ADVANCES IN POLARIZATION ENGINEERING

by

Brian Daugherty

A Dissertation Submitted to the Faculty of

JAMES C. WYANT COLLEGE OF OPTICAL SCIENCES

In Partial Fulfillment of the Requirements

For the Degree of

DOCTOR OF PHILOSOPHY

In the Graduate College

THE UNIVERSITY OF ARIZONA

2019

THE UNIVERSITY OF ARIZONA
GRADUATE COLLEGE

As members of the Dissertation Committee, we certify that we have read the dissertation prepared by *Brian Daugherty*, titled *Advances in Polarization Engineering* and recommend that it be accepted as fulfilling the dissertation requirement for the Degree of Doctor of Philosophy.

Russell Chipman Date: 11/6/2019

Daewook Kim Date: 11/6/2019

Stanley Pau Date: 11/6/2019

James Breckinridge Date: 12/09/2019

Final approval and acceptance of this dissertation is contingent upon the candidate's submission of the final copies of the dissertation to the Graduate College.

I hereby certify that I have read this dissertation prepared under my direction and recommend that it be accepted as fulfilling the dissertation requirement.

Russell Chipman Date: 12/09/2019
Dissertation Committee Chair
Optical Sciences

Acknowledgements

I would like to thank my parents for always being supportive and almost never asking “Are you done yet?” I would also like to thanks my younger brother, Robin, who provided some serious motivation by threatening to complete his PhD before me.

I would like the thanks my partner, Erin, for the patience, support, and joy she has given me throughout this process.

I would like to thank Chris for his encouragement and for being part of so many memorable moments over the years.

I would like to thank my advisor Professor Russell Chipman for the invaluable advice he has given me throughout our time together. He provided the space necessary for me to learn about how to manage research projects while always providing any support or advice I needed along the way.

I would like to thanks Tiffany whose friendship I will always cherish. I loved all of our conversations over sushi.

I would all of the students and scientists who have worked in the Polarization Laboratory during my tenure. Everyone contributed in some way to making the lab a fun place to work.

Dedication

To Danny.

Table of Contents

LIST OF FIGURES

LIST OF TABLES

ABSTRACT

Polarization plays an important role in many optical systems and device. This includes devices designed to advantageously use polarization, like liquid crystal displays, and optical systems that measure polarization to obtain information not otherwise available, like instruments found in many modern telescopes. Polarization also needs to be considered in some systems where it is not a primary aspect of the design, like image formation in very high numerical aperture objective lenses. This manuscript discusses three optical engineering projects where accurate polarization analysis or testing was required.

Chapter one discusses a case where the need for polarization engineering arises from extreme optical requirements. Exoplanet direct imaging requires extremely high contrast, so any possible phase errors need to be considered. This includes the effects of form birefringence, which had previously not been measured over a large diameter mirror. Chapter one presents the first measurements of form birefringence over a large diameter telescope mirror. Measurements of the 3.75-meter, spherical mirror, coated by vacuum deposition of aluminum, indicate low levels of retardance and diattenuation that vary over the face of the mirror. The retardance and diattenuation had maximum values of about $2x10^{-3}$ radians and 0.025% respectively. Initial modeling by Davis J., et al. shows that this level of form birefringence could be impactful in direct imaging systems. The chapter discusses the design of the metrology system used to perform the measurements.

The polarization engineering in chapter 2 relates to a remote sensing instrument that detects polarization to provide information in addition to its spectral reflectance measuring capabilities. Chapter two covers the design and testing of the second-generation

polarization state generator used for the calibration and testing of Jet Propulsion Laboratory's (JPL) air-based, multispectral polarimetric imager (AirMSPI). The chapter focuses on the requirements of a polarization standard. The first-generation instrument is analyzed carefully and the lessons learned are applied to improving the second. The updated version has been successfully used for AirMSPI calibration prior to multiple airborne science campaigns.

The third chapter discusses the analysis and modification of a nominally non-polarizing optical sub-system that has polarization design requirements. This highlights important polarization issues that occur is systems containing a large number of surfaces. The issues with the systems polarization performance are identified. A method to improve the polarization performance that can be implemented without any additional calculations is demonstrated. The system is then modified to improve the polarization performance while maintaining other important optical properties. Finally, the manufacturability of the modified design is considered.

CHAPTER 1

FORM BIREFRINGENCE OF 3.75 METER ALUMINUM MIRROR

1.1 Introduction

1.1.1 Form Birefringence

Form birefringence refers to the refractive index anisotropy that occurs in organized structures with feature sizes smaller than the wavelength of light but much larger that the constituent atoms or molecules. Form birefringent structures can have strong polarization properties, and are used for a number of polarization specific applications. They also occur incidentally during thin film deposition, which commonly results in subwavelength columnar structure [1]. Figure 1.1 shows a scanning electron microscope (SEM) micrograph of 4 types of metal films deposited with different substrate rotations [2].

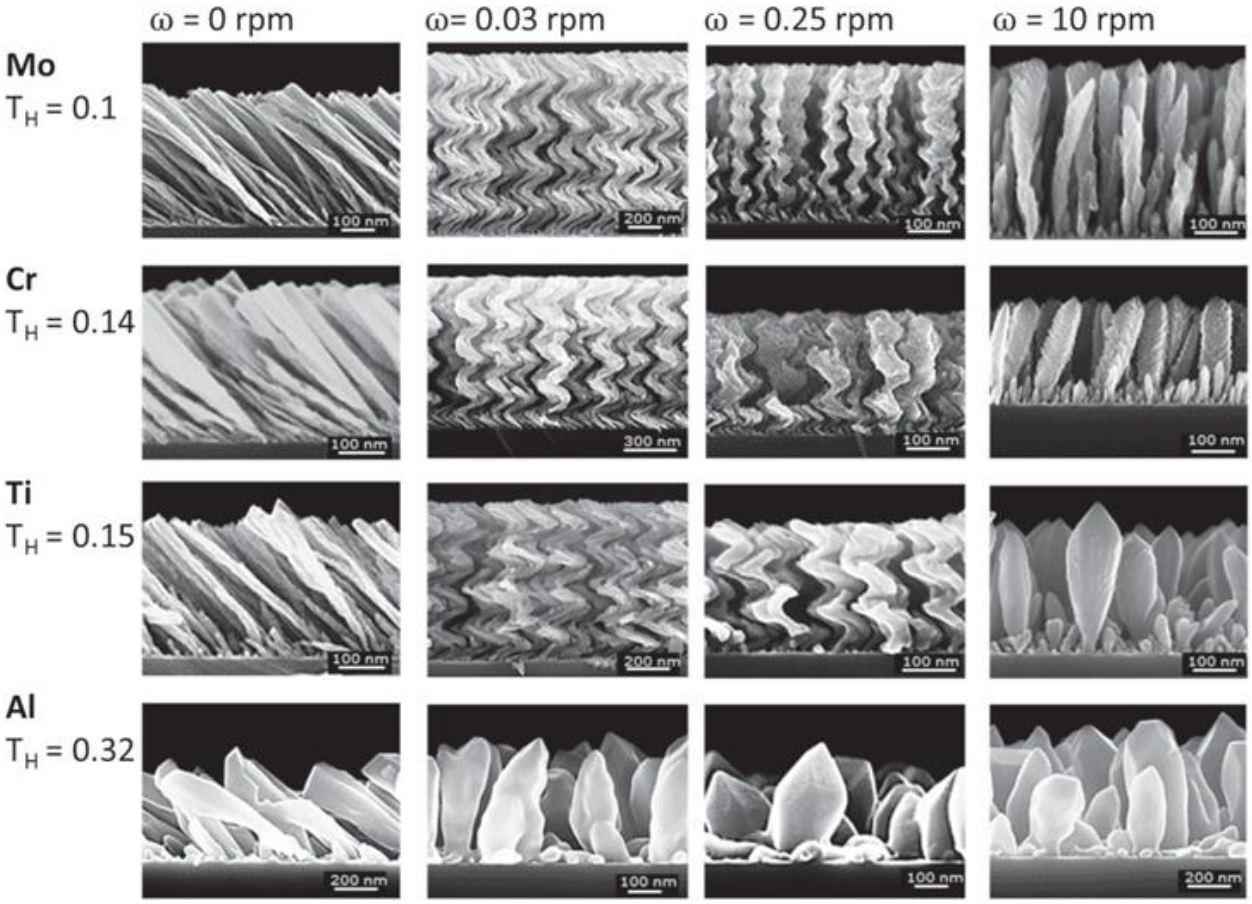

Figure 1.1. SEM micrograph of four metal coatings applied at room temperature with a deposition angle of 84° and the substrate rotating with a frequency ω [2].

The wide applicability of form birefringent devices has led to considerable research into new fabrication techniques and better control processes for existing techniques [3, 4, 5, 6, 7, 8, 9, 10, 11]. Early research demonstrated a relationship between the angle of the columnar nanostructure and the coating deposition angle. Measurements of coatings with tilted columnar nanostructure displayed retardance and diattenuation at normal incidence. Much of the research into fabrication processes focused on oblique angle deposition (OAD)

and has led to considerable control over the growth of nanostructure films and the resulting polarization properties.

An area that has not received significant attention is the form birefringence in large astronomical mirrors [12, 13, 14]. Research into OAD films has demonstrated what coating deposition techniques and conditions promote or reduce columnar growth. Normal incidence deposition in high vacuum reduces contaminants and shadowing effects and produces the most amorphous films. Coating processes for small optical components closely approximate the optimal configuration by arranging the components such that individual components subtend a small angle when viewed from the source. This arrangement requires at least one dimensions of the chamber be much larger than the part diameter and only makes sense from a cost standpoint if coating runs contain many units. It is more challenging to approximate optimal conditions for large diameter substrates. The sources must be placed much closer to the substrate. Coating chambers equipped with multiple sources and the ability to rotate the substrate produce coatings with good thickness uniformity. However, the process clearly includes oblique deposition geometry, known to produce form birefringence.

A new class of telescopes designed for direct imaging of exoplanets have extremely tight contrast requirements [15, 16, 17, 18]. Any birefringence in the primary mirror will impact the point spread function (PSF). Adaptive optics cannot correct for birefringence since they module average optical path length (OPL). It is important to understand risk associated with form birefringence in large diameter mirrors. Previously, the form birefringence of large mirrors had not been measured. In view of this, a polarimeter was

developed and employed to measure the form birefringence of a 3.75 m diameter aluminum mirror.

1.1.2 Coating Induced Form Birefringence of Large Mirror

In order to understand the impact coating microstructure could have on astronomical telescopes, the form birefringence of a 3.75 m, aluminum coated mirror has been measured. The mirror was found to be weakly polarizing, with low levels of retardance and diattenuation detected. Measurements were performed at 450 nm. The maximum retardance measured $2x10^{-3}$ radians or $3x10^{-4}$ waves. The maximum diattenuation measured 0.025%.

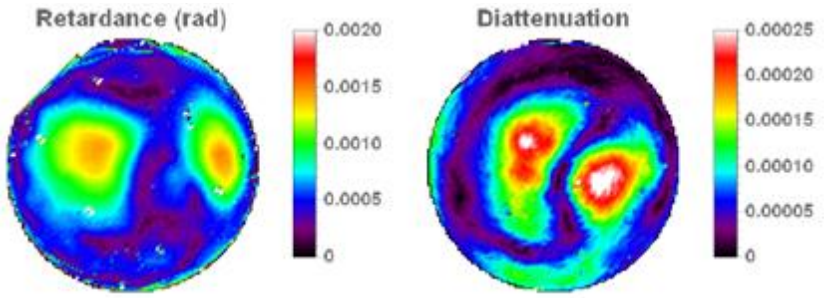

Figure 1.2. Retardance and diattenuation map of a 3.75 m Al coating spherical mirror. Additional measurements can be found in Figure 1.24 and Figure 1.25.

This is the first published measurement of form birefringence over a large diameter mirror. The magnitude of retardance and diattenuation in normal incidence reflection from such mirrors was previously unknown and the results presented here may or may not be typical of astronomical mirrors and other large reflective optics. The mirror discussed in this work is part of the testing apparatus for the Giant Magellan Telescope. It was coated at Kitt Peak National Observatory using methods typical of astronomical mirrors in the

same chamber as the Mayall 4 m primary. This suggests similar levels of form birefringence could be possible in a wide range of astronomical telescope mirrors.

While 0.002 radians of retardance and 0.025% diattenuation sound very small they may have a meaningful effect for applications requiring extreme contrast, like the direct imaging of exoplanets. Models of JPL's HabEx have shown more than an order of magnitude contrast reduction over much of the working area when the retardance map measured here is applied to the primary mirror [19]. The effects of form birefringence cannot be completely corrected with standard adaptive optics wavefront control methods because the retardance introduces a polarization dependent phase and adaptive optics modulate the optical path length. Further measurement of astronomical mirrors would help assess the risk associated with form birefringence for high contrast imaging systems.

1.2 Experiment Design Considerations

This section discusses how experimental requirements affected the design of the form birefringence polarimeter. The primary design requirement of separating small values of form birefringence from other sources of polarization, like polarization aberrations, drives the basic hardware configuration. The configuration imposes constraints on the type of sample the polarimeter can measure. The configuration and sample requirements make calibrating the instrument difficult which affects the choice of polarization optics and polarimetry.

1.2.1 Isolating Form Birefringence from Polarization Aberrations

In addition to form birefringence, polarization aberrations will affect the mirrors polarization properties. Polarization aberrations are the well-understood polarization dependence found in oblique reflection or transmission at interfaces [20, 21, 22, 23]. The form birefringence polarimeter needs to perform its form birefringence measurements using a method that will not mistakenly include polarization aberrations.

Basic ellipsometry does two things relevant to the design of the form birefringence polarimeter, (1) ellipsometry has developed multiple methods for obtaining the relevant polarization properties, this is discussed further in the polarimetry section, and (2) ellipsometers are specifically designed to measure polarization properties caused by oblique incidence, the same polarization properties that the form birefringence polarimeter needs to suppress. Ellipsometer's approach to measuring polarization properties offers multiple methods that should be considered but their measurement geometry provides a clear example to avoid.

Ellipsometers measure the change in the polarization ellipse imparted by a surface and fit the results to previously known models to determine surface properties like film thickness and refractive index [24, 25, 26, 27]. The samples are usually isotropic so the polarization change occurs due to s- and p- reflection or transmission differences. The ellipsometer's sensitivity is increase by performing measurements in a configuration that maximizes this difference. To accomplish this ellipsometers commonly perform measurements with large incident angles such as near Brewster's angle.

Figure 1.3 shows the reflectance and polarization properties for an Al coated surface. The bottom row of plots shows the retardance (left) and diattenuation (right) for selected wavelengths. Both polarization properties increase approximately quadratically with incident angle out to about 1 radian. Retardance continues to increase approaching glancing incidence and diattenuation peaks at pseudo-Brewster's angle then falls back to 0. This behavior is typical to a wave variety of isotropic interfaces and is the reason most ellipsometers operate at large incident angles.

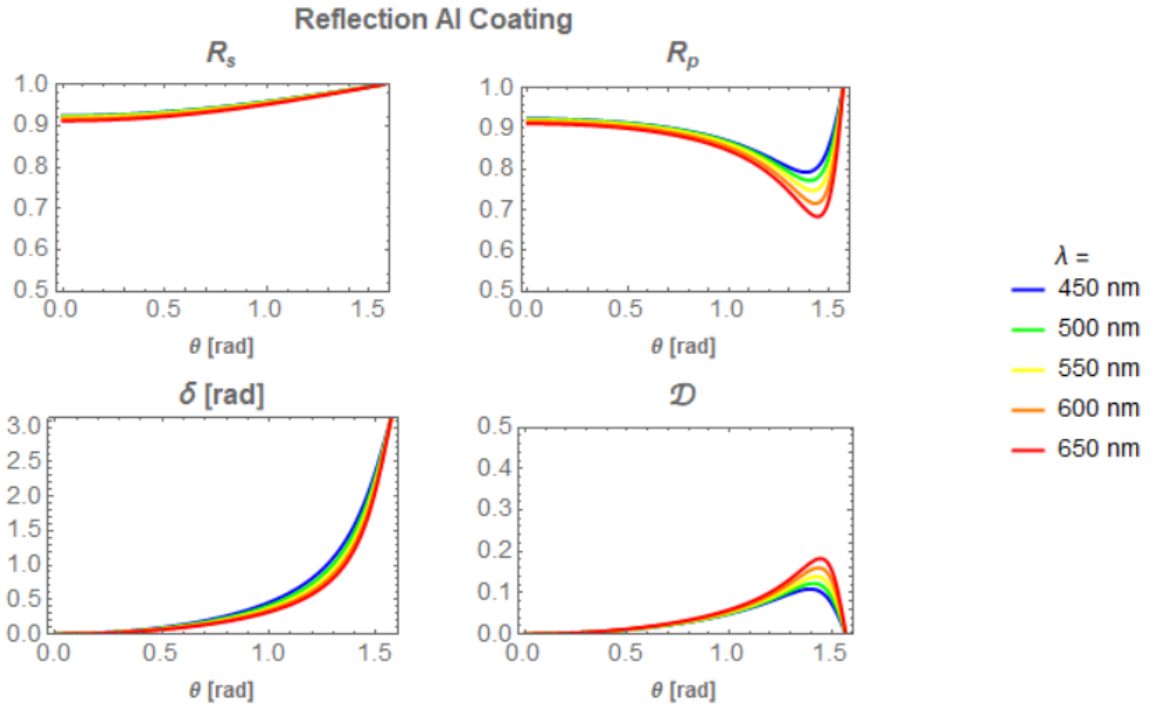

Figure 1.3. Reflection and polarization properties of Al coated surface with increasing incident angle. Top left, s-polarized reflection, top right, p-polarized reflection, bottom left, retardance in units of radians, bottom right, diattenuation.

While ellipsometer's perform measurements near Brewster's angle to maximize polarization aberrations it makes sense for the form birefringence polarimeter to perform measurements at normal incidence where polarization aberrations go to zero. Any

polarization found at normal incidence will be attributed to form birefringence from anisotropic nanostructure. Due to the quadratic nature of polarization aberrations, performing near-normal incidence measurements is very effective at reducing polarization aberrations. Figure 1.4 shows the polarization properties of reflection from an Al coating as a function of incidence angle with 6° highlighted. Both retardance and diattenuation from polarization aberrations are reduced to the approximate order of the form birefringence found in the mirror, 3.97×10^{-3} radians and 4.5×10^{-4} respectively. The form birefringence polarimeter is designed to operate a much smaller angles, with a maximum incident angle if about 0.11°, but this demonstrates that even much larger "small angles" significantly reduce polarization aberrations.

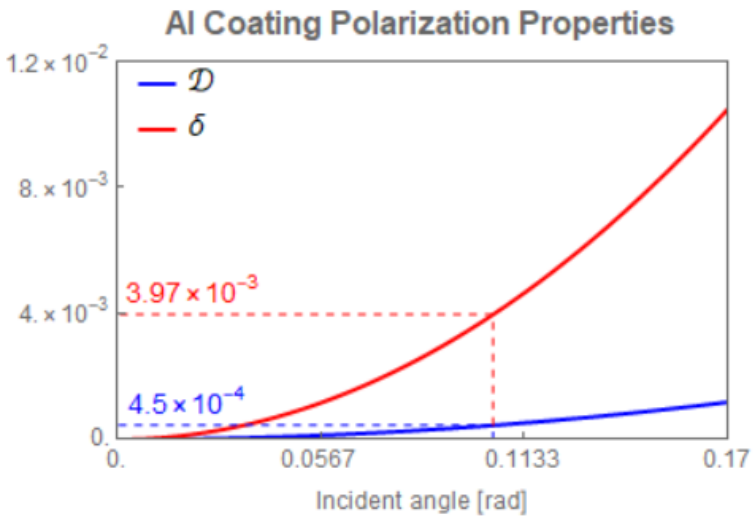

Figure 1.4. Diattenuation and retardance in reflection from Al coating vs incident angle with 6° AOI highlighted.

The near-normal incidence operation requirement is the primary driver of the overall form birefringence polarimeter layout. The concept, originally proposed by Breckenridge [12], of placing all the polarimeter components very close to the center of

curvature of a spherical mirror, accomplishes both near-normal illumination and view angles over the entire mirror surface. If the light source beam angle fills the mirror's aperture with limited overfill, the system will be extremely light efficient with almost all of the illumination reaching the detector. Figure 1.5 shows the basic layout. This configuration limits the samples that the form birefringence polarimeter can measure to approximately spherical mirrors with an accessible center of curvature. The dimensions shown in Figure 1.5 limit the maximum incident angle to about 0.11°, corresponding to retardance and diattenuation of 1.4×10^{-6} radians and 1.6×10^{-7} respectively.

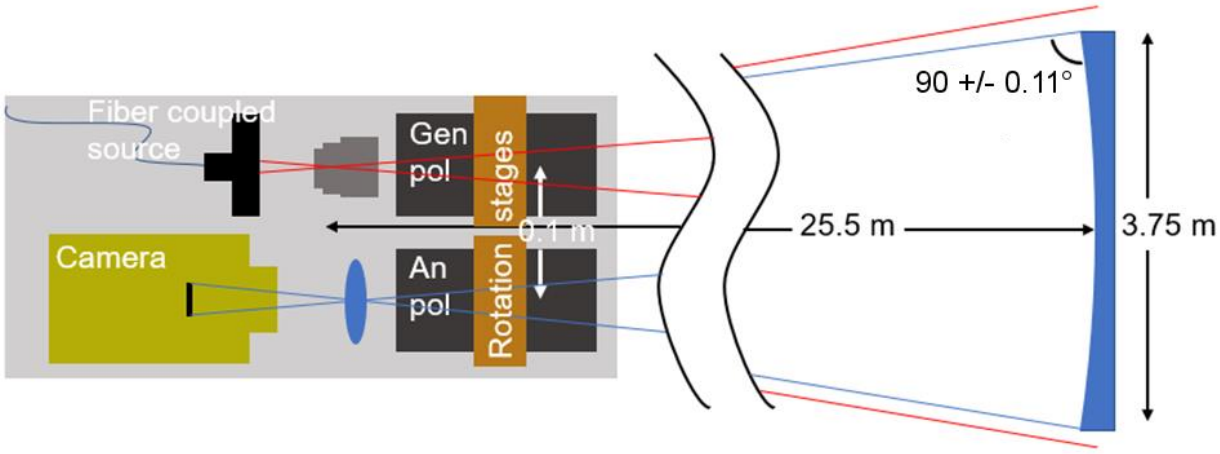

Figure 1.5. Form birefringence polarimeter basic layout and dimensions.

1.2.2 Measurement Environment Related Calibration Limitations

Polarimeters reduce a set of intensity modulations into polarization information. Calibration is the process of determining the relationship of the intensities to Stokes or Mueller parameters. In Mueller matrix polarimetry the mathematical description of a measurement is,

$$\mathbf{D} = \mathbf{A}\,\mathbf{M}\,\mathbf{G} \tag{1.1}$$

Where **D** is a vector of detected intensities, **A** contains all of the analyzer vectors describing how the polarimeter responds to any Stokes vector leaving the sample, **M** is the Mueller matrix of the sample, and **G** contains generator vectors defining the illumination side of the polarimeter. This equation assumes a linear detector response. The calibration process determines **A** and **G** so that once **D** is measured **M** can be calculated. One methods for determining **A** and **G**, a priori knowledge of the polarization elements is used to model the instrument, the model parameters are determined by performing one or more calibration measurements on known samples, and **A** and **G** are calculated based on the model [28, 29, 30, 31, 32]. The other category of calibration techniques determines **A** and **G** without using a priori knowledge of the polarimeter by performing calibration measurements on known samples until **A** and **G** are overdetermined [33].

Both techniques assume that the system configuration during calibration is the same as the configuration during measurements, except for the sample. The system must remain stable and repeatable between calibration and measurement. both methods require measurements be performed with reference samples. This form birefringence experiment will not meet any of these requirements.

In preparation for this measurement, the form birefringence polarimeter was constructed and tested in Professor Chipman's Polarization Laboratory at the University of Arizona and then transported to the Richard F. Caris Mirror Lab for the measurement. Measurements were performed after hours or on weekends with the form birefringence polarimeter stored out of the way during business hours to avoid interfering with work on the Giant Magellan Telescope. This necessitates moving and aligning the experiment prior

to each measurement so maintaining a high degree of repeatability will be difficult. Additionally, since the experiment illuminates and views the sample from the center of curvature, there is no straight forward way to replace the sample with a known calibration standard. These calibration issues result in a requirement that the measurement procedure and data reduction determine the form birefringence using only data collected during the measurement process.

1.2.3 Polarimetry Overview

Given the limited calibration options available, the form birefringence polarimeter benefits from using a small number of components to limit the sources of uncertainty. It is preferable that the components themselves do not require calibration. Given these concerns, the only polarization elements in the form birefringence polarimeter are its generator and analyzer polarizers. This section demonstrates how linear diattenuation and retardance can selectively measured using two rotating linear polarizers.

A simple experiment using two polarizers and a sample is to cross the polarizers so they are uniformly dark, then place the sample between them to see if it causes transmission. Any transmission could be a sign of diattenuation, or retardance, or polarization rotation due to the sample's geometry. If there is no transmission the sample might still have non-zero retardance or diattenuation. So, this simple experiment alone does not separate the retardance from the diattenuation, or really provide much information of either. The form birefringence polarimeter needs to do all of those things and also distinguish linear polarization properties from circular polarization properties. The Poincare sphere is a useful tool to understand how weak linear retarders and diattenuators

change the polarization of linearly polarized incident light and how that change can be measured with a linear polarizer.

Figure 1.6 shows the evolution of horizontally polarized light incident on various linear retarders. Each circle represents a different retarder orientation with the circle's rotation axis intersecting the retarder's fast and slow axis coordinates on the Poincare sphere. The circle represents the output polarization as the retardance varies from 0 radians to 2π radians. All of the circles are tangential when the retardance equals zero and have instantaneous trajectories moving from horizonal towards right circular polarization with no lateral movement, which would represent rotation of linear polarization. Weak linear retarders, regardless of orientation, acting on linearly polarized light approximate this type of trajectory, with the change in polarization move directly towards circular with no rotation of linear polarization. The orientation will affect how far the polarization state moves along the sphere for a given retardance magnitude. This means that the transmission caused by a weak retarder placed between crossed polarizers occurs because the retarder has introduced a circular component to the incident linear state. The circular component will have 50% transmission though a linear polarizer independent of orientation.

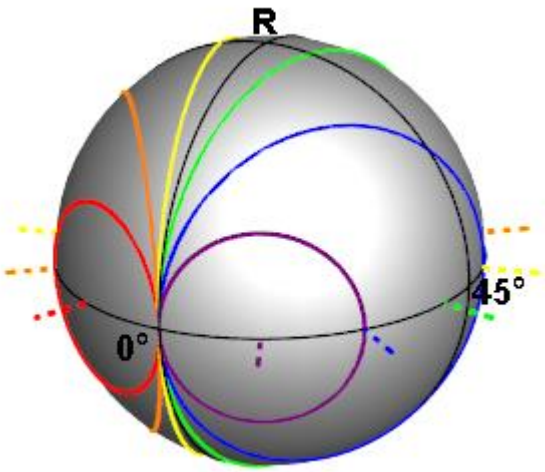

Figure 1.6. The circles depict how various linear retarders will modify horizontal polarized light. As the retardance changes from 0 to 2π the polarization state travels around a circle centered on an axis through the fast and slow axis directions or the retarder.

A linear diattenuator acting on a linear polarization state causes the preferential transmission of one linear state. On the Poincare sphere this causes the initial polarization state to move along the equator towards the transmission axis and away from the absorption axis. This is a rotation of the incident linear polarization state which clearly causes light transmit through the crossed analyzer polarizer. Since the modified polarization state remains entirely linear the leakage caused by diattenuation can be removed if the analyzer polarizer is allowed to rotate. The amount the analyzer must rotate is related to the magnitude and orientation of the diattenuation.

Weak linear retarders and diattenuators cause orthogonal trajectories of linearly polarized light on the Poincare sphere, with retardance the change in confined to ellipticity and for diattenuation the change is confined to angle of polarization. The form birefringence polarimeter performs measurements by setting the polarizers to minimize

transmission and measuring the transmission and the relative angle between the polarizer axes. This is sufficient to separate linear retardance from diattenuation but still doesn't provide enough information to separate linear properties from circular properties or determine the magnitude of the linear properties.

Circular retardance, like linear diattenuation, will cause a polarization rotation and circular diattenuation, like linear retardance, will increase ellipticity. These effects are not distinguishable from linear diattenuation and retardance, respectively, in a single measurement, but by rotating the polarizers and repeating the measurements the leakage and orientation associated with linear polarization properties will modulate while leakage and orientation caused by circular polarization properties will remain constant. Repeated measurements at different angles will also provide the information necessary to determine the magnitude of the linear effects.

Mueller calculus is used to investigate the transmission, as a function of orientation and retardance, caused by a weak linear retarder placed between crossed polarizers. This is analogous to a stationary sample, with weak linear retardance, placed in the form birefringence polarimeter, and rotating the polarizer. Equation (1.2) gives the Mueller matrix for a retarder with retardance δ and orientation θ. Equations (1.3 and 1.4) are the Mueller matrices for linear polarizers at 0° and 90° [34],

$$\mathrm{LR}[\delta,\theta] = \begin{pmatrix} 1 & 0 & 0 & 0 \\ 0 & \cos(\delta)\sin^2(2\theta)+\cos^2(2\theta) & \sin^2\left(\frac{\delta}{2}\right)\sin(4\theta) & -\sin(\delta)\sin(2\theta) \\ 0 & \sin^2\left(\frac{\delta}{2}\right)\sin(4\theta) & \cos(\delta)\cos^2(2\theta)+\sin^2(2\theta) & \sin(\delta)\cos(2\theta) \\ 0 & \sin(\delta)\sin(2\theta) & \sin(\delta)(-\cos(2\theta)) & \cos(\delta) \end{pmatrix} \quad (1.2)$$

$$\mathrm{LP}[0^\circ] = \begin{pmatrix} \frac{1}{2} & \frac{1}{2} & 0 & 0 \\ \frac{1}{2} & \frac{1}{2} & 0 & 0 \\ 0 & 0 & 0 & 0 \\ 0 & 0 & 0 & 0 \end{pmatrix} \tag{1.3}$$

$$\mathrm{LP}[90^\circ] = \begin{pmatrix} \frac{1}{2} & -\frac{1}{2} & 0 & 0 \\ -\frac{1}{2} & \frac{1}{2} & 0 & 0 \\ 0 & 0 & 0 & 0 \\ 0 & 0 & 0 & 0 \end{pmatrix}. \tag{1.4}$$

The Mueller matrices are multiplied together to model the cumulative effect of light transmitting through the form birefringence polarimeter generator, off of a weakly deattenuating sample and through the polarimeters analyzer,

$$\mathrm{LP}[90^\circ].\mathrm{LR}[\delta,\theta].\mathrm{LP}[0^\circ] = \begin{pmatrix} 2\sin^2\left(\frac{\delta}{2}\right)\sin^2(\theta)\cos^2(\theta) & 2\sin^2\left(\frac{\delta}{2}\right)\sin^2(\theta)\cos^2(\theta) & 0 \\ -2\sin^2\left(\frac{\delta}{2}\right)\sin^2(\theta)\cos^2(\theta) & -2\sin^2\left(\frac{\delta}{2}\right)\sin^2(\theta)\cos^2(\theta) & 0 \\ 0 & 0 & 0 \\ 0 & 0 & 0 \end{pmatrix} \tag{1.5}$$

.

Multiplying the cumulative Mueller matrix by the Stokes parameters for horizontal polarization gives the output Stokes parameters. Horizontal polarization is used as the input instead of unpolarized light so that the transmission between parallel polarizers is 1 instead of 0.5. The output Stokes parameter represents the light incident on the detector, and since the detector is non-polarizing, it measures the Stokes parameter s_0,

$$S_{out} = \begin{pmatrix} 2\sin^2\left(\frac{\delta}{2}\right)\sin^2(\theta)\cos^2(\theta) & 2\sin^2\left(\frac{\delta}{2}\right)\sin^2(\theta)\cos^2(\theta) & 0 & 0 \\ -2\sin^2\left(\frac{\delta}{2}\right)\sin^2(\theta)\cos^2(\theta) & -2\sin^2\left(\frac{\delta}{2}\right)\sin^2(\theta)\cos^2(\theta) & 0 & 0 \\ 0 & 0 & 0 & 0 \\ 0 & 0 & 0 & 0 \end{pmatrix} \cdot \begin{pmatrix} 1 \\ 1 \\ 0 \\ 0 \end{pmatrix}$$

$$= \begin{pmatrix} \sin^2\left(\frac{\delta}{2}\right)\sin^2(2\theta) \\ -\sin^2\left(\frac{\delta}{2}\right)\sin^2(2\theta) \\ 0 \\ 0 \end{pmatrix} \tag{1.6}$$

$$I_{out} = S_{out,0} = \left(\sin^2\left(\frac{\delta}{2}\right)\sin^2(2\theta)\right) . \tag{1.7}$$

Since the form birefringence polarimeter will be measuring very small levels of retardance, $\delta << 1$, the intensity is expanded to two orders around $\delta=0$ resulting in, $\left(\frac{\delta}{2}\right)^2 \sin^2(2\theta)$. The transmission between crossed polarizers caused by a weak retarder has a maximum value of $\delta^2/4$ that occurs at retarder orientation of 45° and repeats every 90° of retarder rotation.

The effect of diattenuation is modeled using the Mueller calculus to determine change in polarization orientation imparted on a horizontal incident state by a linear diattenuator. The Mueller matrix of a diattenuator with diattenuation D and orientation θ defined as,

$$\mathrm{LD}[\mathcal{D},\theta] = \begin{pmatrix} \frac{1}{\mathcal{D}+1} & \frac{\mathcal{D}\cos(2\theta)}{\mathcal{D}+1} & \frac{\mathcal{D}\sin(2\theta)}{\mathcal{D}+1} & 0 \\ \frac{\mathcal{D}\cos(2\theta)}{\mathcal{D}+1} & \sqrt{\frac{2}{\mathcal{D}+1}-1}\,\sin^2(2\theta)+\frac{\cos^2(2\theta)}{\mathcal{D}+1} & \frac{1}{2}\left(\frac{1}{\mathcal{D}+1}-\sqrt{\frac{2}{\mathcal{D}+1}-1}\right)\sin(4\theta) & 0 \\ \frac{\mathcal{D}\sin(2\theta)}{\mathcal{D}+1} & \frac{1}{2}\left(\frac{1}{\mathcal{D}+1}-\sqrt{\frac{2}{\mathcal{D}+1}-1}\right)\sin(4\theta) & \frac{\sin^2(2\theta)}{\mathcal{D}+1}+\sqrt{\frac{2}{\mathcal{D}+1}-1}\,\cos^2(2\theta) & 0 \\ 0 & 0 & 0 & \sqrt{\frac{2}{\mathcal{D}+1}-1} \end{pmatrix}. \tag{1.8}$$

For horizontal input polarization, the output polarization state is calculated by multiplying the diattenuator Mueller matrix by {1,1,0,0}. Since the form birefringence polarimeter will deal with very small diattenuation, D << 0, the output state is expanded to first order around D = 0,

$$\mathrm{LD}[\mathcal{D},\theta].\begin{pmatrix}1\\1\\0\\0\end{pmatrix} = \begin{pmatrix} \frac{\mathcal{D}\cos(2\theta)+1}{\mathcal{D}+1} \\ \frac{(\mathcal{D}+1)\sqrt{\frac{2}{\mathcal{D}+1}-1}\,\sin^2(2\theta)+\mathcal{D}\cos(2\theta)+\cos^2(2\theta)}{\mathcal{D}+1} \\ \frac{2\mathcal{D}\sin(2\theta)-(\mathcal{D}+1)\sqrt{\frac{2}{\mathcal{D}+1}-1}\,\sin(4\theta)+\sin(4\theta)}{2(\mathcal{D}+1)} \\ 0 \end{pmatrix} \approx \begin{pmatrix} 1-2\,\mathcal{D}\sin^2(\theta) \\ \mathcal{D}\cos(2\theta)-\mathcal{D}+1 \\ \mathcal{D}\sin(2\theta) \\ 0 \end{pmatrix} \tag{1.9}$$

By definition the output angle of linear polarization (AoLP) is related to the Stokes parameters by,

$$AOLP = \frac{1}{2}\tan^{-1}\left(\frac{s_2}{s_1}\right) \approx \frac{1}{2}\tan^{-1}\left(\frac{\mathcal{D}\sin(2\theta)}{\mathcal{D}\cos(2\theta)-\mathcal{D}+1}\right) \tag{1.10}$$

Since D << 1,

$$AOLP \approx \frac{1}{2}\mathcal{D}\sin(2\theta) \tag{1.11}$$

A weakly diattenuating sample will cause a maximum rotation in radians equal to one half its diattenuation. The magnitude of the rotation will depend on the diattenuator's orientation relative to the incident polarization state and will repeat every 180°

The form birefringence polarimeter measures retardance by measuring the intensity transmission through two linear polarizers that have been aligned to minimize transmission. It measures diattenuation by measuring the angle between the polarizers at minimum transmission. Repeating these measurements at different polarizer orientations provides information on the frequencies present in the minimum transmission and orientation data. This allows effects of linear polarization properties to be distinguished from circular polarization properties.

The form birefringence polarimeter uses aspects from both nulling ellipsometry and photometric ellipsometry. A null ellipsometry approach would have added a quarter waveplate to the system so that full extinction could always be achieved. The relative angles of all three components are then used to determine both the retardance and diattenuation. The form birefringence polarimeter uses this concept to measure diattenuation but uses a photometric approach for retardance. The primary reason being, that motorized components in the system were not accurate enough to provide accurate absolute positions, and the near normal incidence configuration would make it difficult to calibrate the relative component orientations. More detailed discussion of the issues using orientation information can be found in the diattenuation data reduction section. The retardance measurement used a photometric ellipsometry concept by detecting the amplitude of a modulated signal. Using this approach allowed the form birefringence polarimeter use only polarizers which was preferable based on the limited calibration capabilities.

1.3 The Form Birefringence Polarimeter

Figure 1.7 shows the form birefringence polarimeter with the important components labeled. This section will give additional details on the instrument including a description of the data acquisition software routine.

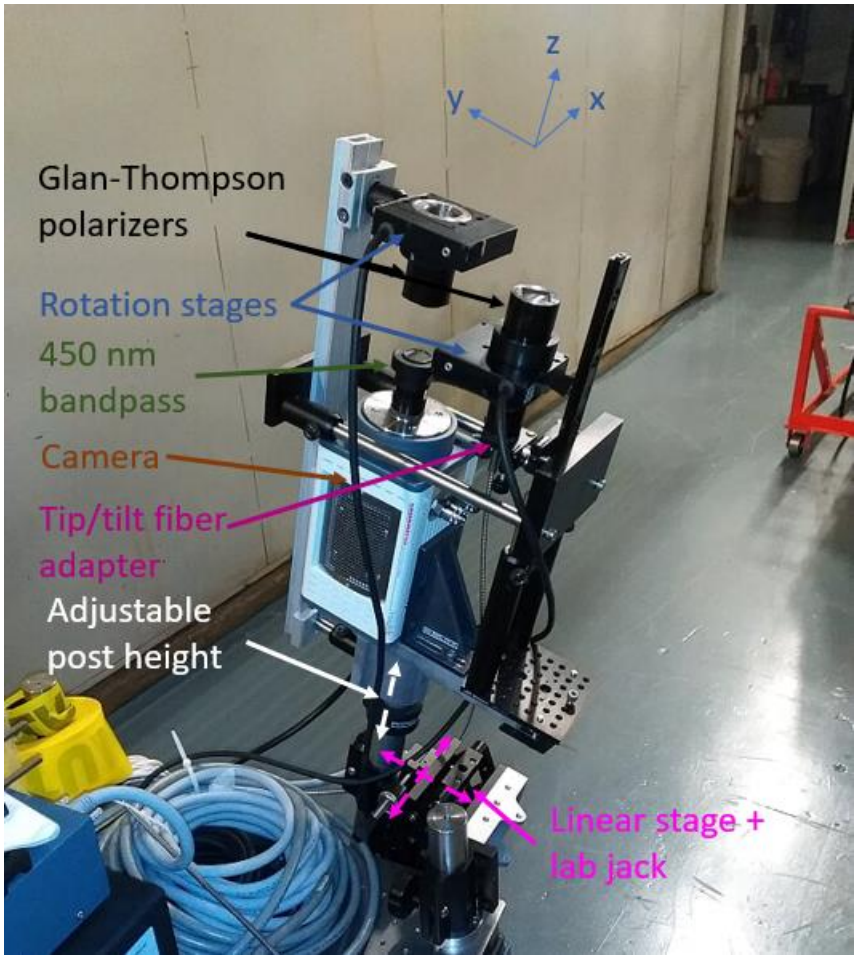

Figure 1.7. Photograph of the form birefringence polarimeter. Light travels in the z-direction toward a spherical mirror six meters above.

1.3.1 Polarization Components

The form birefringence polarimeter has two identical α-BBO Glan-Thompson polarizers. One polarizer placed after the source is used to generate the linear polarized

illumination state. A polarizer before the camera analyzes the incoming polarization. The polarizers are Red Optronics GMP-6020, they have 20 mm clear apertures with extinction ratio specifications < $5x10^{-6}$ and a large field of view >15°. The usable field of view and the extinction ratio depend on how the polarizers are used. In the form birefringence polarimeter the useful field of view is smaller than 15° and the extinction ratio is better than advertised. This will be discussed in the data analysis section.

1.3.2 Light Source

Illumination is provided by a Spectral Products xenon arc lamp fiber coupled to an 1/8 m monochromator. A 1 mm core diameter fiber couples to an adapter in the form birefringence polarimeter illumination system. The monochromator was originally selected to provide flexibility. In practice, the strong spectral dependence of the Glan-Thompson polarizer field of view resulted in all measurements being performed at 450 nm.

1.3.3 Mechanical Components

The form birefringence polarimeter has a computer-controlled rotation stages for precisely rotating the generator and analyzer polarizers and a variety of manual stages to provide the degrees of freedom necessary for alignment. The polarizers are mounted to Newport sr50cc motorized rotation stages and controlled by a Newport 301 motion controller. The stages provide precise positioning when stepped at low speed in a single direction. The accuracy decreases due to backlash when the direction of travel is reversed. The motors absolute accuracy limitations force some assumptions during the diattenuation data reduction. This is discussed in the diattenuation part of the data reduction section.

The alignment of the form birefringence polarimeter requires movement in all 6 degrees of freedom, 3 translations and 3 rotations. The tip/tilt of the entire system requires coarse adjustment to aim the camera at the mirror. This is provided by moving the entire table holding the form birefringence polarimeter and adjusting the angle between the base post and the instrument axis. There is also coarse rotation of the entire instrument head about its axis. This is performed by rotating the axis post in its clamp. The source is fiber coupled to a 2-axis translation stage connected to the projection objective. This allows the source to be centered on the sample once the camera is aligned. With both camera and source aligned, the instrument head needs to be translated so that the light returned from the mirror is centered on along the analyzer axis of the form birefringence polarimeter. This requires sub-millimeter two axis positioning. A manual linear translation stage provides the entirely horizontal movement in the x-direction and a lab jack provides movement in the y-direction. An adjustable collar on the instrument axis post allows translation along z.

Component	Degree of Freedom	Purpose	Notes
Generator motor	z-axis rotation	Polarimetry	
Analyzer motor	z-axis rotation	Polarimetry	
Monochromator	wavelength	Polarimetry	Hardly used due to FOV issues
Source tip/tilt	Tip/tilt	Aim illumination	
Vertical post mount	Rough rotation	Aim camera at mirror	
Full arm tilt	Rough rotation	Aim camera at mirror	
Lab-jack	Precise alignment	Center return light on camera aperture	
Translation stage	Precise alignment	Center return light on camera aperture	
Near vertical post	Rotate source/camera head	Data redundancy and checking for systematic errors	

Table 1.1. List of dynamic hardware in the form birefringence polarimeter.

1.3.4 Camera

The form birefringence polarimeter uses a Hamamatsu c9100-13 ImagEM Enhanced camera. The detector is 512 x 512 pixels with an area of 8.19 mm x 8.19 mm, and 16 μm square pixels. It is an electron multiplying, back-thinned frame transfer CCD detector that has usable quantum efficiency down to 300 nm. It is a 16-bit camera with a 370,000 electron full well capacity, 8 electron readout noise, and 0.01 electron/s/pixel dark current. It responds linearly over nearly its full range, which was verified with calibrated neutral density filters. The low dark current is important because of the long integration times necessary given the low light levels. Integration times on the order of seconds cause a negligible decrease in dynamic range.

1.3.5 Control Software

A Labview based program controls the polarizer rotation stages and the camera, acquiring and storing raw images, and performing the first data reduction step and storing the reduced images. The automation is important because each measurement involves acquiring 221 raw image files. The software provides a setup screen that shows a live image from the camera and allows manual control of the polarizer rotation stages, the monochromator output wavelength, and the controls used to specify parameters for an automated measurement. Once parameters are specified and the start button is activated, the program populates an empty directory with folders with names based on the scan parameters. The program then checks for empty folders and performs the measurement specified by the first one it sees. This process continues until there are no empty folders left in the directory.

When a folder is selected the program parses the folder name to determine the generator angle to use. The generator polarizer rotates to the specified angle and the analyzer rotates the generator angle plus 89 degrees. The analyzer then takes two 1° steps with an image acquired before each step and after the last step. The images are used to determine the approximate null angle to center a +/- 0.4° scan. The analyzer polarizer rotates to 85° then rotates to its starting position for a +/- 0.4° scan. The camera exposure is determined based on the signal strength and then 13 images are acquired as the analyzer steps through 0.8°. Quadratic curve fitting is used to obtain a minimum transmission map and an orientation map for each wavelength. All of the raw data and both maps are exported and the program checks for the next empty folder.

1.4 Description of Measurement Procedure and Data Collected

The polarimetry section developed the basic concepts of what data the form birefringence polarimeter needs to obtain to determine the linear retardance and diattenuation of the sample. The previous section on control software discussed some of the details related to how the automated software actually acquires the raw data. This section aims to provide a clear explanation of the measurement procedure and how it relates to the concepts from the polarimetry section. As well as a clear description of all the components that make up each data set.

Section 1.2.3 established what data needs to be collected to determine the diattenuation and retardance of the 3.75 m mirror. The calculation requires a series of measurements obtained as the sample rotates relative to the generator polarizer. Each measurement contains two pieces of information, (1) the minimum transmission possible for the given generator/sample configuration, found by rotating the analyzer, and (2) the analyzer orientation at which the minimum transmission occurs. The periodicity of these quantities as a function of generator angle separates the linear from circular polarization properties.

In practice, the detector is a camera with many pixels making it infeasible to attempt to manually rotate the analyzer to the position that minimizes each pixel. Instead of trying to acquire a single measurement at the best analyzer orientation a series of images are acquired at discrete steps through the minimum transmission configuration. Quadratic curve fitting provides the minimum transmission and orientation images. To acquire the first minimum transmission and orientation pair for example, images are acquired for the

following {generator, analyzer} polarizer angles: {{0, -90.4}, {0, -90.33}, {0, -90.267}, … ,{0, -89.67}, {0, -89.6}} making 13 total images. From these images one minimum transmission image and one orientation are calculated. This is repeated 16 additional times so the second set of images would have the following {generator, analyzer} angles: {{22.5, -67.9}, {22.5, -67.83}, {22.5, -67.77}, … ,{22.5, -67.17}, {22.5, -67.1}}. This results in 17 sets of minimum transmission and orientation pairs, the former used to calculate linear retardance and the latter used to calculate linear diattenuation.

1.5 Data Reduction

The following section explains the process used to reduce 221 images, 13 at each generator angle and 17 generator angles acquired for each form birefringence polarimeter data set into a retardance map and a diattenuation map showing the mirror's form birefringence. As discussed in section 1.2.3, the retardance is calculated using the minimum transmission through linear polarizers and the diattenuation is calculated from the relative orientation at which the minimum transmission occurs. This results in two distinct data reduction methods that share the first step. This section begins with the common first step, then explains he retardance calculation followed in the diattenuation calculation.

1.5.1 Leakage and Orientation Maps

The first data reduction step involves analyzing the thirteen images acquired while the analyzer polarizer rotates 0.8°, from one side of the crossed-polarizer null to the other, to create the minimum transmission and orientation images.

The transmission between two linear polarizers as a function of the angle between their polarization axes is given by Malus's law,

$$T = \mathrm{Cos}^2[\theta] \quad (1.12)$$

With $\theta = \pi/2 + \varepsilon$, and $\varepsilon << 1$, series expansion shows that T varies with ε^2. The raw images are the transmission through two linear polarizers as ε varies from -0.007 to 0.007 radians in 13 steps. The minimum transmission values are used to determine the quadratic coefficients of the small angle approximation of Malus's law,

$$T = a\theta^2 + b\theta + c. \quad (1.13)$$

Setting dT/dθ to 0, and solving for θ gives the analyzer orientation for minimum transmission,

$$\theta_{pol} = -b/(2a). \quad (1.14)$$

$$T_{min} = c - \frac{b^2}{4a} \quad (1.15)$$

The quadratic fitting completes the process of reducing the raw images to the relative orientation maps. However, the minimum transmission maps must be referenced to the maximum transmission to provide meaningful information for calculating retardance. To maintain fully automated scan software the maximum transmission map is calculated based on the same 13 images used to calculate minimum transmission map. The maximum transmission is given by Malus's law or the peak amplitude of a $\sin^2$ function. Looking at the series expansion of $\sin^2$,

$$a_0 \mathrm{Sin}^2[a_1 x] \approx a_0 a_1{}^2 x^2. \quad (1.16)$$

The amplitude and frequency of a $\sin^2$ both appear in the amplitude term of the series expansion. If the frequency is unknown it is not possible to retrieve the $\sin^2$ amplitude from measurements around x=0. If a_1 is known, like in Malus's law $a_1 = 1$, a_0 can be determined. For $a_1 = 1$, $a_0 = a$, and the ratio of minimum transmission to maximum transmission is just T_{min}/a or,

$$T_{\min}/T_{\max} = -\frac{b^2 - 4\,a\,c}{4\,a^2}. \tag{1.17}$$

Alternatively, the maximum transmission can be obtained by rotating the analyzer polarizer 90° from the minimum orientation. This approach would result in an off-axis ray transmitting along a different region of one of the polarizers for the maximum transmission image compared to the maximum extinction image. This could lead to polarizer apodization affecting the calculated transmission ratio. Obtaining the maximum transmission image also creates issues in the data acquisition process. The form birefringence polarimeter uses long exposure times to increase the signal to noise near the null. The detector starts to saturate within 1° of the null configuration. The form birefringence polarimeter does not include a filter wheel or any other method to modulate the light source intensity and the camera exposure cannot be set to a low enough value to prevent saturation with parallel polarizers. Obtaining maximum transmission images would require human intervention regularly over the hours-long measurement.

This completes the first step of the analysis and reduces the first 13 raw images to a referenced minimum transmission map and a relative polarizer orientation map. This step is repeated for each of the generator polarizer orientations (0°, 22.5°,…, 360°) resulting in

17 of each map. One complete data set is shown in Figure 1.8 and Figure 1.9, showing the minimum transmission and relative orientation maps respectively.

In Figure 1.8, the bright region on the left side of the 22.5° image, vanishes in the 67.5° image, reappears at 112.5°, and continues that pattern through the remaining images. The bright region on the right side of the 67.5° image modulates with the same frequency but different phase. The relative orientation images in Figure 1.9 also exhibit periodic behavior. The visually apparent periodicity is caused by the rotation of the hyperbolic paraboloid shaped field dependence found in each map. This is the expected behavior due to the field dependence of the Glan-Thompson polarizers. Any relative orientation chances caused by mirror diattenuation must be separated from this much larger orientation signal. The following sections discuss the retardance calculation from 17 minimum transmission images and the diattenuation calculation using 17 relative orientation images.

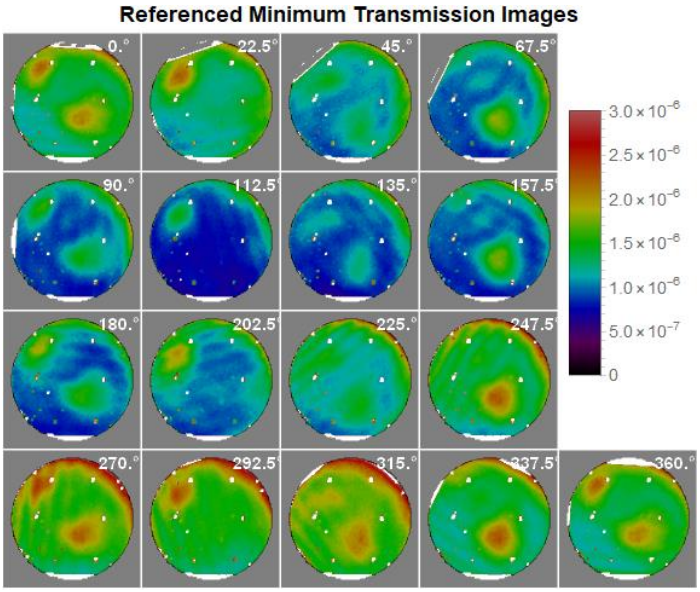

Figure 1.8. 17 minimum transmission maps, each one generated from 13 images. The angle in the upper right of each image gives the generator polarizer orientation. The value being plotted is the minimum transmission relative to the maximum transmission. The leakage due to retardance is expected to be 90 degree periodic so similarities along columns of the figure are important.

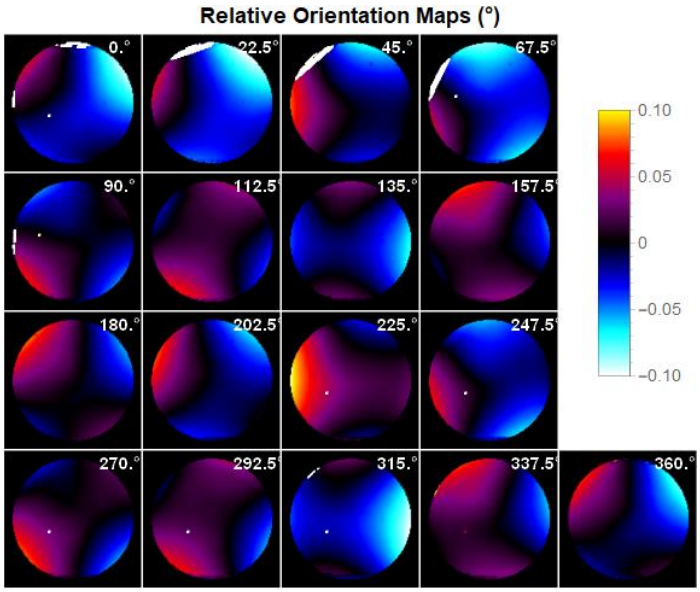

Figure 1.9. Relative orientation maps for 17 generator polarizer orientations. Each one composed from 13 images. The value plotted is the angle in degrees at which the minimum transmission occurred with the generator angle subtracted and 90 degrees added to center the data around 0.

1.5.2 Retardance

This section explains the process to reduce the 17 images in Figure 1.8 to a single map of the mirror's linear retardance. The polarimetry section showed that for a low polarization sample, the minimum leakage between polarizers is related to the samples linear retardance, circular diattenuation, and retardance orientation. The dependence on retardance orientation causes the minimum transmission due to linear retardance to modulate with a period of 90° as a pair of crossed polarizers rotate. Any transmission caused by the unlikely presence of circular diattenuation is independent of polarizer orientation and does not modulate, and can still be separated in the data reduction process.

The discrete Fourier transform (DFT) provides a straight forward method to calculate the retardance from the minimum transmission images. Before performing the

DFT the 0° and 360° images are averaged so that the data set runs from 0° to 337.5°. The images are then arranged into an array of dimensions 512 x 512 x 16. The DFT is performed on the 16-element list obtained by indexing the first two dimensions of the array. For a purely linearly retarding sample the Fourier transform will have 3 non-zero elements. The +/- 4^{th} harmonic component contains the 90° period signal and the 0^{th} harmonic contains the DC signal that occurs because minimum leakage is always greater than 0.

Figure 1.10 shows the first 5 DFT coefficients of the minimum transmission maps. The black circle drawn over the maps illustrates where the mirror's edge should be. A section of the map along the upper left edge retuned retardance values much larger than the rest of the map, significantly off the color scale used in the plot. The issue occurs because those pixels saturate in some of the minimum transmission images, as can be seen in Figure 1.8 in a number of images, 67.5° being one of the most pronounced. The saturation occurs when the angle of incidence at the Glan-Thompson's hypotenuse is too low for the ordinary mode to experience total internal reflection (TIR). For these fields, the Glan-Thompson's diattenuation drops to close to 0 and the corresponding pixels saturate. Since the field of view depends on the angle on incidence at the hypotenuse surface, it is asymmetric about the Glan-Thompson's center axis in the plane of incidence of the hypotenuse. It is symmetric about the center axis in the plane containing the center axis and normal to the plane of incidence. The asymmetry varies with wavelength due to dispersion of the crystal and cement materials used in the Glan-Thompson. These effects can significantly reduce the useful symmetric field of view to a fraction of the full asymmetric field.

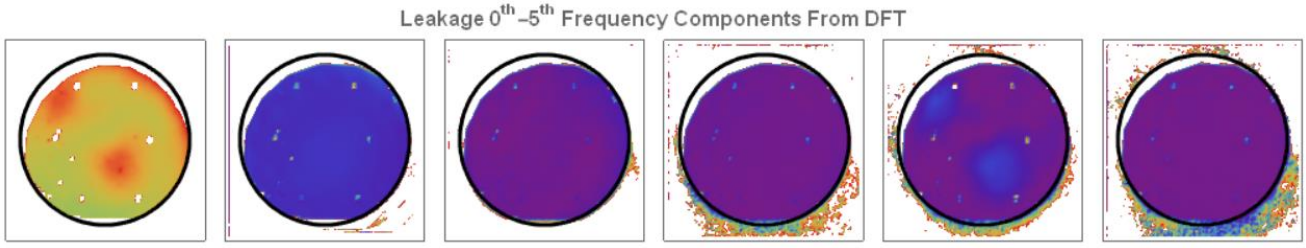

Figure 1.10. First 5 terms of the DFT calculated using 16 images per pixel. There is a clear spatial variation in the 4th harmonic which is repeated in the 0th harmonic due to the positive nature leakage. The other 4 harmonics look approximately uniform. The black circle shows where the mirrors edge should be. There is a fairly large region with no data in the upper left part of the mirror.

The wavelength of 450 nm was chosen to reduce field of view asymmetry while maintaining enough source power and detector quantum efficiency. This increases the symmetric field of view of each Glan-Thompson to slightly smaller than the angle subtended by the mirror. The polarizers are aligned so that for most generator orientations the entire mirror falls in the usable field, but limited flexibility in the polarizer fixturing made occasional saturation unavoidable. The nominal sample rate used while rotating the generator polarizer was twice the Nyquist frequency for the highest frequency of interest. As long as there are not too many saturated pixels, they can be rejected while maintaining a sufficient sample rate to reconstruct the signal. Figure 1.11 shows the number of samples per pixel after rejecting saturated pixels. Over most of the mirror all 17 samples were unsaturated, but at the top left edge there are a small number of pixels where only 12 samples were used. Due to the non-uniform sampling caused by rejecting bad pixels, the Fourier coefficients are calculated by directly fitting the data to the sine-cosine Fourier series.

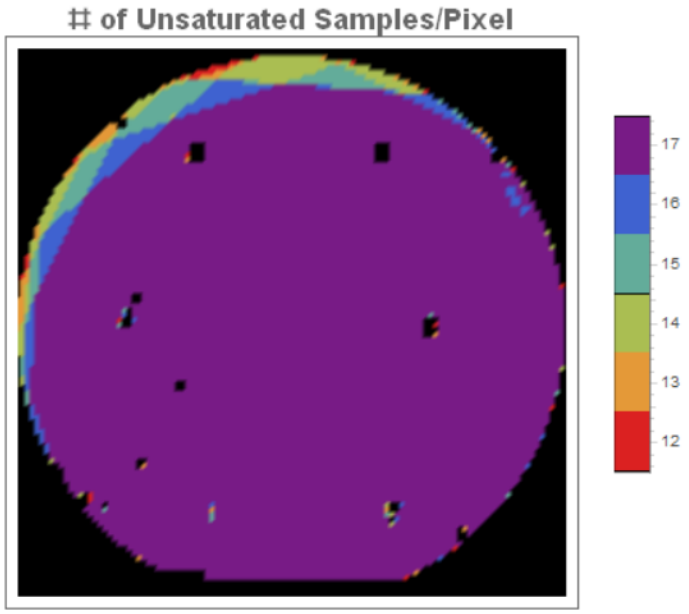

Figure 1.11. A graphical representation of the number of pixels used in the non-linear curve fitting for each pixel index. Most of the pixels are in the red level meaning all 17 data points are available for extracting the retardance. Near the edge of the mirror there are regions where reduce usable data points.

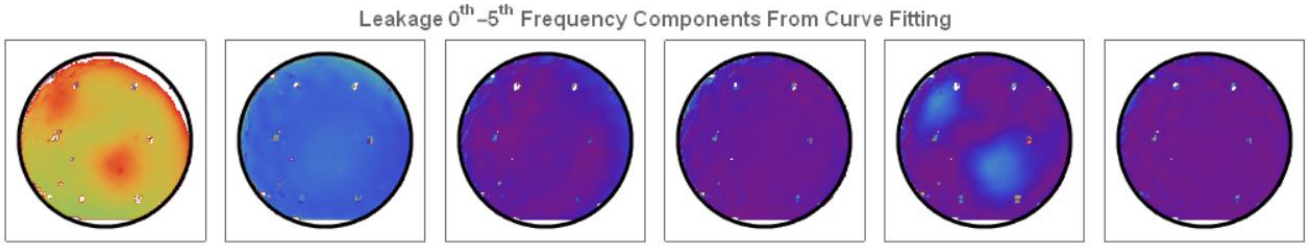

Figure 1.12. The 0th through 5th harmonics of the leakage signal. There is background leakage seen in the 0th harmonic and 90° periodic leakage in the 4th.

Figure 1.12 shows the same dataset at Figure 1.10. The field of view has been improved extending to the edges of the mirror. Faint artifacts are visible in the previously saturated regions. This will be discussed further in the results section.

The retardance magnitude is calculated from the peak value of the transmission attributed to retardance. The source of transmission is determined by the frequency of the

signal as the polarizers are rotated through 360°; retardance caused transmission has a 90° periodic signature. Since transmission is always greater than 0, half of the retardance leakage amplitude appears in the zero-frequency component. Given the 4th harmonic,

$$a_4 \cos(4\theta) + b_4 \sin(4\theta) \tag{1.18}$$

the retardance will be,

$$\delta = 2\sqrt{2A_4}\ radians\ with\ A_4\ = \sqrt{a_4^2 + b_4^2} \tag{1.19}$$

This is the same result calculated in the polarimetry section with an additional $\sqrt{2}$ to account for the amplitude appearing in the DC term.

1.5.3 Diattenuation

Calculating the diattenuation from the orientation images is considerably more involved than the retardance procedure. The orientation maps do not provide an absolute reference like the leakage maps. The polarizer rotation stages do not have the absolute accuracy to relate the orientations from one generator polarizer angle to the next. For each individual generator configuration, the polarizer motor steps through the scan and the relative orientation between the pixels can be determined more precisely. This means the data reduction process needs estimate the average angle from one generator orientation to the next. This requires an assumption about the diattenuation at some point on the mirror. Due to these limitations the form birefringence polarimeter is insensitive to spatially uniform diattenuation at the mirror.

The data reduction software also needs to separate the orientation due to diattenuation from other sources of orientation variation present in the measurements. This

is challenging because the field dependence of the Glan-Thompson polarizers causes significantly more orientation variation in the maps than the diattenuation. A Glan-Thompson polarizer model was developed and fit to the data using free parameters related to the possible tilts of the polarizer.

1.5.3.1 Uniaxial Crystals and Glan-Thompson Polarizers

Glan-Thompson polarizers take advantage of the birefringent nature of uniaxial crystals to separate incident light by polarization. [35, 36, 37, 38]. Figure 1.13 shows the basic layout of a Glan-Thompson polarizer. The polarizer is comprised of two identical wedges of α-BBO, a negative uniaxial material, cemented together such that both crystal axes are parallel to the entrance and exit faces and parallel to the diagonal face. Light entering the polarizer splits into ordinary and extraordinary modes which propagate to the cement interface. The cement and wedge angles are selected so that the ordinary ray experiences total internal reflection and the extraordinary ray transmits with minimal reflection loss. The reflected ordinary ray is usually absorbed at the top side of the prism. The extraordinary ray refracts into one ray in the isotropic cement layer, and then refracts into two modes in the second crystal. The eie mode is the intended exiting polarization state [39].

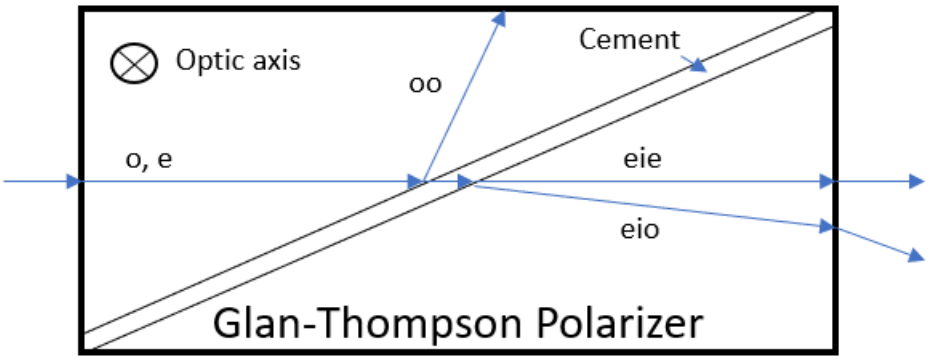

Figure 1.13. Glan-Thompson polarizer. The optic axis points into the page. The large angle of incidence at the diagonal allows the o- mode to experience TIR while the E mode transmits into the cement layer and then out through a second uniaxial material.

Lam analyzed a Glan-Taylor polarizer in considerable detail, especially in the description of its field of view, mode coupling, and field dependent contrast [40]. Glan-Taylor polarizers replace the cement with an air gap making them suitable for higher power applications but reducing the field of view. While the field of view properties of the Glan-Taylor will not be quantitatively relevant to Glan-Thompson polarizers, Lam's qualitative observations are useful. Lam modeled the intensity in each of the four modes exiting a single Glan-Taylor Prism, eie, oio, eio, and oie, and identified the eio mode as the largest undesirable mode contribution. Fortunately, the large distance between the form birefringence polarimeter's polarizers and the sample mirror ensure that any mode-coupling occurring at the polarizer hypotenuse will not reach the mirror. Of the modes identified only oio has to potential to reduce the form birefringence polarimeter performance and can be reduced to very near zero with proper alignment. More relevant than individual mode analysis is the discussion and modeling of the Glan-Taylor's contrast [40].

Lam defines the extinction ratio as the transmittance through two perfectly aligned parallel Glan-Taylor polarizers divided by the transmittance through perfectly aligned orthogonal Glan-Taylors. Lam found a Maltese cross shaped region of high contrast which falls off quickly with tilts about any axis other than x or y. The eieieie mode contributed the most intense leakage. The other leakage modes identified were coupled modes that would miss the detector of the form birefringence polarimeter. The leakage calculated for the eieieie mode, of 0.00035, is about 350 times larger than the maximum retardance leakage signal observed with the polarimeter. This seems to suggest the form birefringence polarimeter's polarizers perform better than the theoretical Glan-Taylor polarizers modeled by Lam. The eieieie mode only occurs in Lam's simulations for off-axis propagation. It occurs when the e mode leaving the first polarizer does not couple completely into the o mode of the second polarizer. Rotating the second polarizer to the correct angle would allow full coupling of the e mode to the o mode, with each off-axis field requiring a slightly different rotation. The form birefringence polarimeter accomplishes this by its procedure of taking images while stepping through the crossed polarizer null to determine the minimum transmission for each pixel. This also means that while this leakage mode did not impact the retardance measurement or data reduction it causes a polarizer orientation effect that must be separated from diattenuation [40].

1.5.3.2 Glan-Thompson Polarizers and Orientation Images

Figure 1.14 shows the same data as Figure 1.9 but using a 3D plot to emphasize the shape of the surface. The predominate feature for all generator polarizer angles is a hyperbolic paraboloid shape that rotates with the polarizer. Additionally, different maps

have different linear variations as can be seen by the shifting center of the pattern. These visible spatial variations are all due to the polarizer field dependence and must be removed before calculating diattenuation. This is complicated by the fact that rotation stage backlash reduced the accuracy too much to compare angles from different generator polarizer orientations. The stages were precise over each individual generator angle. This leaves a piston-like part of the map that must be removed from each map which requires assumptions about the diattenuation and can have a large effect on the calculated result. This will be discussed later in the section. The remaining Glan-Thompson field effects are backed out of the data by fitting the results to a model using the fewest possible parameters.

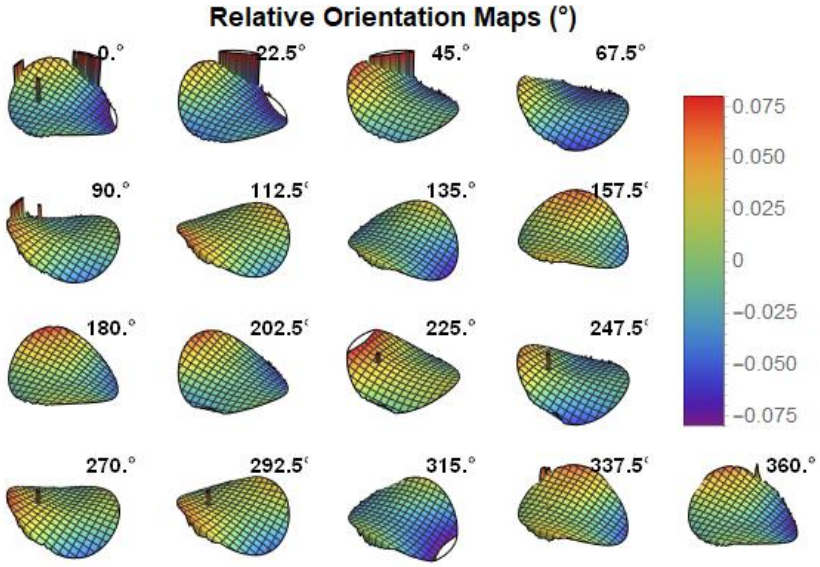

Figure 1.14. The is the same information as Figure 1.9 but plotted using a 3-D plot to highlight the predominant shape occurring in each map.

Before discussing the Glan-Thompson model it will be helpful to visualize how the orientation maps relate to the raw measured data. Figure 1.15a. shows raw intensity images acquired for 0° generator angle as the analyzer stepped from 89.6° to 90.4°. The image at

the bottom of the stack was the first image acquired and the image at the top of the stack was the last image acquired as the analyzer rotated through extinction. The leakage image can be approximated by taking the darkest regions from each image in the stack and stitching them together. The orientation is determined by how far up the stack of images the smallest values occurs for each pixel. The quadratic curve fitting makes this discrete process continuous.

A form birefringence polarimeter model was created in Polaris-M to simulate the experiments data acquisition process. Figure 1.15b. shows simulated raw images of the data acquisition for well aligned polarizers. Each column represents data from one generator polarizer orientation. The stack is reduced to a minimum leakage map and a orientation map. Each pixel has a minimum value at some height in the stack, this height is the value that appears for that pixel in the orientation map. For the 0° stack of images in Figure 1.15b., the bottom image has black regions near the left and right edges that move towards the center until there is a black “X” centered on the image, the black regions then separate and move towards the front and rear edge of the image. The other columns are similar with the pattern rotating with the polarizer angle. This is the rotating hyperbolic paraboloid seen in the orientation maps.

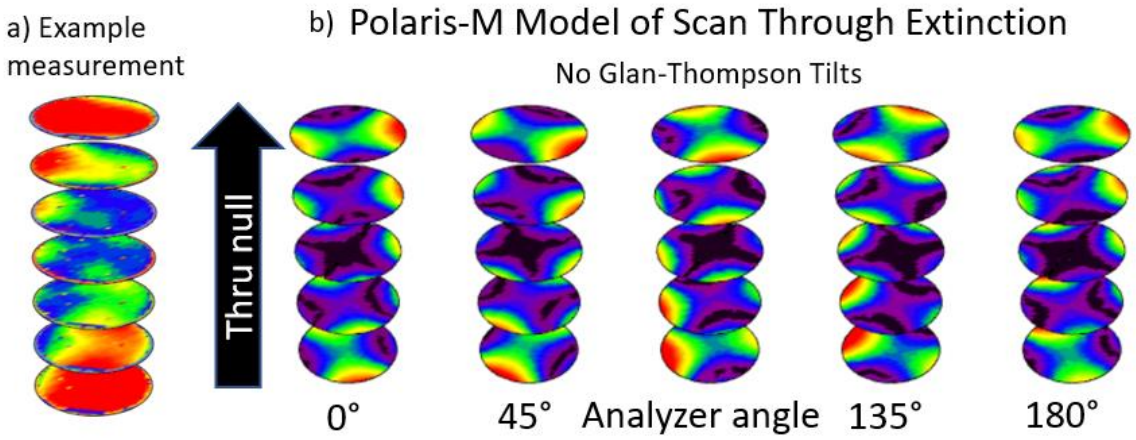

Figure 1.15. a. Shows intensity measurements acquired as the analyzer polarizer stepped through the cross-polarizer orientation. b. Polaris-M model simulation of the measurement performed at different analyzer angles. The set shows a well aligned system i.e. no retarder tilt.

Generator and analyzer tilt errors can be visualized with this approach which will help clarify the various tilt components used in the polarizer model. Figure 1.16 shows additional simulations performed for various types of Glan-Thompson alignment errors. Beginning with the bottom simulation, showing the effects of rotating the generator and analyzer about parallel tilted rotation axis that are aligned with the polarizers' center axes; moving up these stacks a dark line moves across the images from the front left of the bottom image, to the back right of the top image. The surface that connects the black pixels through the stack approximates a tilted plane. The image stacks for different polarizer orientations all have approximately the same behavior. This type of polarizer alignment error will appear in the orientation maps as a tilt term that is constant through all polarizer orientations.

Moving up to the middle row of Figure 1.16, showing the effect of rotating the generator and analyzer about the systems optical axis with the polarizers central axis misaligned causing wobble; these images also result in an orientation map dominated by a linear term. Looking at the stacks from left to right; the structure in the images rotates with analyzer angle. The Glan-Thompson polarizer field dependent orientations modeled here will appear as a 360° periodic tilt term in the orientation images.

The top row of Figure 1.16 is not as clear as the first two because the effect is smaller relative to the paraboloid component. These images show the effects of rotating the generator and analyzer about mirrored tilted rotation axes aligned with the polarizers' center axes. In the first stack of images the extinction starts at the back, right edge and moves towards the front, left edge. The orientation image has a small tilt term combined with the hyperbolic paraboloid seen in the well aligned case. Moving left to right through the images, the small tilt component rotates twice as fast as the analyzer. This can most easily be seen by looking at the extinction in the bottom image of each stack. This type of polarizer error will manifest as a 180° periodic tilt in the orientation images.

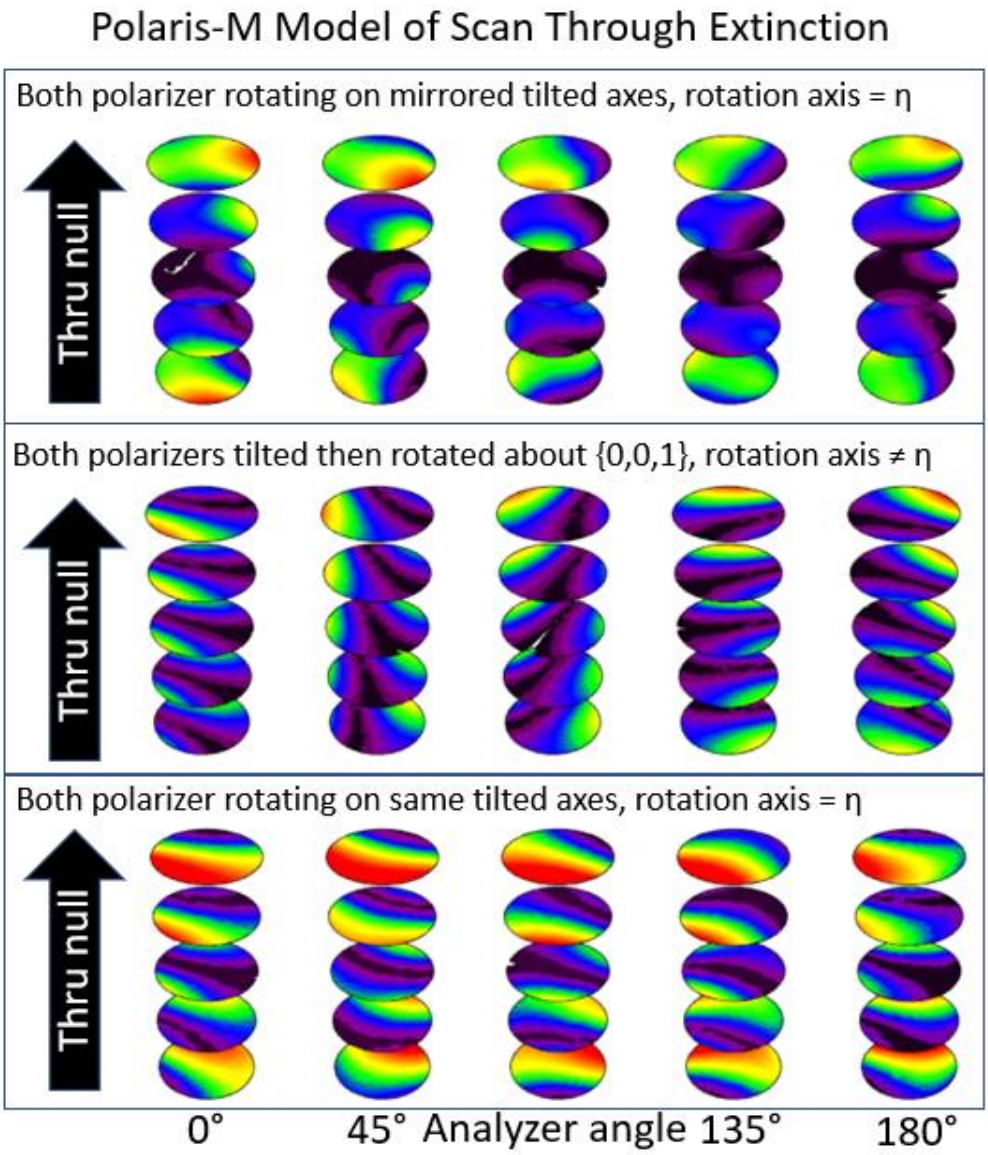

Figure 1.16. Additional simulations with different types of polarizer tilts.

1.5.3.3 Remove Orientations Due to Glan-Thompson

To summarize the observations from the previous section, (1) the Glan-Thompson polarizers introduce a hyperbolic paraboloid shape to the orientation image, (2) this shape rotates with the polarizers, (3) tilts to the polarizer move the hyperbolic paraboloid off axis,

(4) a polarizer that's tilted relative to the rotation axis of the stage such that it wobbles, will produce a shift in the orientation image that rotates with the polarizer, (5) polarizers rotating about tilted axes will either cause a shift in the orientation that rotates with twice the polarizer orientation or a stationary shift depending on the relationship between the generator and analyzer rotation axes. All of these effects can be modeled using the Zernike's polynomial terms for tilt and astigmatism. Piston is also included since the form birefringence polarimeter cannot measure constant diattenuation. The fitting will be performed directly on the orientation images.

There are 17 orientation images for each dataset and fitting them all individually increase the likelihood of losing diattenuation orientation information to one of the Zernike terms. Figure 1.17 shows the results of fitting Zernike's to 17 orientation maps using the simulation from before. The x-axes of these plots correspond to generator orientation. At each generator orientation the orientation image is parameterized by piston, tiltx, tilty, oblique astigmatism, and vertical astigmatism. Clearly these parameters are not independent from one analyzer angle to the next. For example, the astigmatism for the entire dataset does not require (2 astigmatism parameters) x (17 images) = (34 parameters). The astigmatism term depends only on the polarizer properties and the orientation of the pair of polarizers. The amplitude of the astigmatism is constant but it switches between oblique and horizontal with twice the frequency of polarizer rotation. Over the 17 images the astigmatism can be described with just an amplitude and a phase offset if the correct modulation is built into the model. The linear components are treated similarly. Since there are three linear components from the different possible tilts, (DC, 1θ, and 2θ), this leads to

6 parameters to describe them resulting in 8 total parameters. When this process is performed on simulated datasets with only Glan-Thompson induced field dependence the leaves a residual variation on the order of 10^{-6} radians.

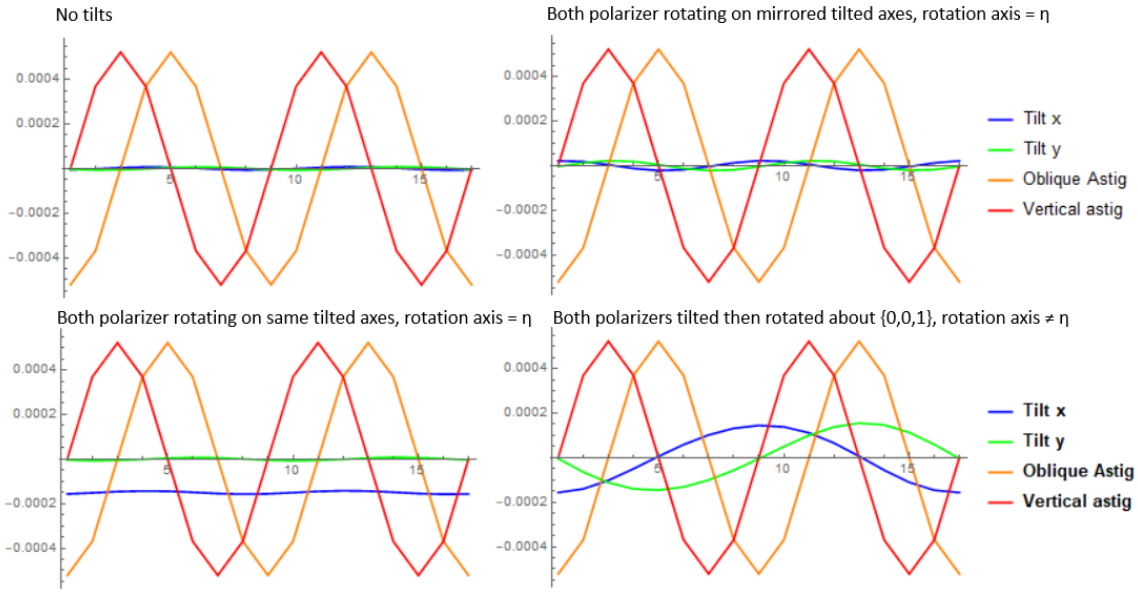

Figure 1.17. Zernike fits to the simulations for different polarizer tilts.

$$GT\ Model = a_0 + a_1 z_1^{-1} + a_2 z_1^1 + a_4 z_2^{-2} + a_5 z_2^2 \tag{1.20}$$

$$a_4 = a_{astig} \cos\left(2\theta - \phi_{astig}\right) \tag{1.21}$$

$$a_5 = -a_{astig} \sin\left(2\theta - \phi_{astig}\right) \tag{1.22}$$

$$a_1 = \sum_{k=0}^{2} a_{tilt,k} \cos\left(k\theta - \phi_{tilt,k}\right) \tag{1.23}$$

$$a_2 = \sum_{k=0}^{2} a_{tilt,k} \sin\left(k\theta - \phi_{tilt,k}\right) \tag{1.24}$$

$$\theta = \frac{\pi}{8} n \quad n = 0,1,2,\ldots,16 \tag{1.25}$$

Figure 1.18 shows the results of applying the model to 5 complete datasets. The datasets correspond to measurements at various system orientations. The astigmatism parameter is constant across the measurement as expected. The tilts change by small amounts between measurements which is expected. The polarizers had to be adjusted for each configuration to try to optimize the field of view. The parameters are plugged into the Glan-Thompson model to create masks for each dataset. The masks are subtracted from their orientation images isolate possible diattenuation effects on orientation.

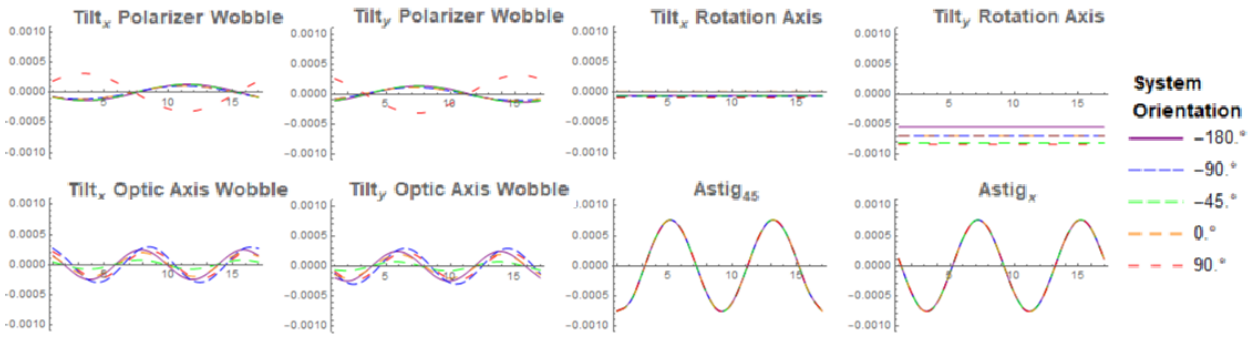

Figure 1.18. Best fit parameters for 5 complete datasets at different instrument orientations.

This method to remove the polarizer effects relies on a couple big assumptions. Diattenuation orientation will not take a tilt like form. If it does it would be removed by 2x frequency tilt term. And there is not diattenuation offset or piston-like term. All piston was removed from orientation maps prior to fitting because the rotation stage motors did not maintain enough accuracy over large motion angles to use their values finely compare orientations between different generator angles.

1.5.3.4 Calculate Diattenuation

Figure 1.19 shows the orientation images after attempting to remove the polarizer effects. The final step is to perform the harmonic analysis on the orientation images and convert the correct frequency component to diattenuation. Figure 1.20 shows the harmonic analysis of the orientation image. The second harmonic, where we expect to find orientation due to diattenuation, shows a clear signal while all other frequency components are near zero.

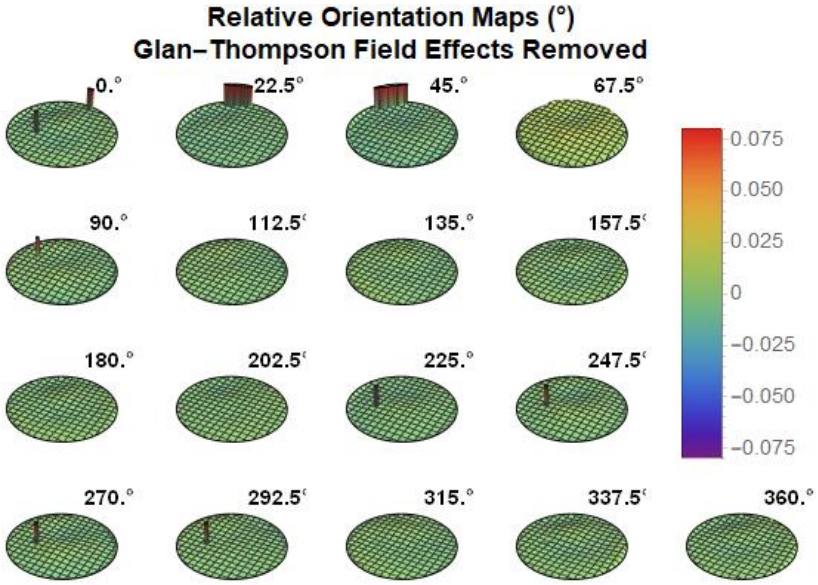

Figure 1.19. Orientation images after removing contribution from Glan-Thompson polarizers.

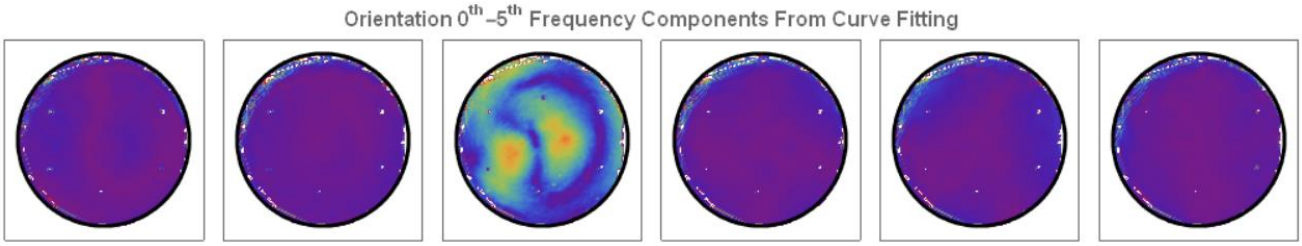

Figure 1.20. Harmonic analysis of one complete set of orientation images. The second harmonic shows a distinct pattern while all other frequency components show no signal.

1.5.3.5 Test Method with Simulated Data

Simulated orientation data was created to test this data reduction method. The simulated orientation maps were created by modeling the experiment in Polaris-M. A 2-D distribution was chosen for the diattenuation and entered into the model as pure diattenuator Jones matrices. The full sequence of measurements was simulated by running a new ray trace for each raw image that would be collected in an actual measurement. Curve fitting the raw simulated images produced the leakage and orientation maps.

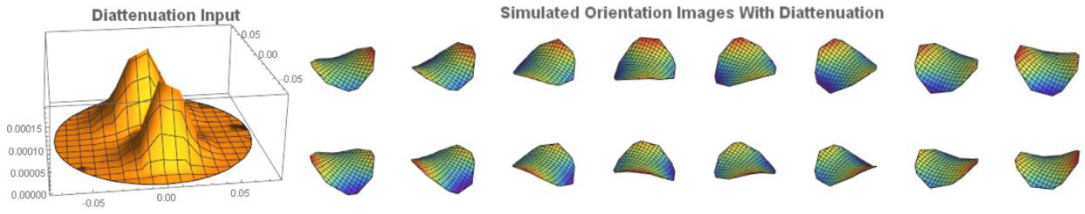

Figure 1.21. Left. The mirror diattenuation used in the simulation. Right. The orientation maps after the diattenuation is added. The rotation caused by diattenuation is small enough that it cannot be easily seen in the orientation maps.

Prior to fitting the orientation maps to the model, the piston was removed from each map separately. This was carried out by simply fitting a piston term to each individual map and removing it. Curve fitting is performed to find the 8 parameters from the previous

section. The model is used to generate a Glan-Thompson orientation map that is removed from the simulated orientation map, leaving the orientation due to diattenuation. Harmonic analysis is performed on the result and the 180° periodic component is taken as the orientation due to diattenuation. Figure 1.21 shows that the diattenuation recovered by this method generally reproduces the main features of the input map but has substantial error. The accuracy can be improved with a priori knowledge of the input diattenuation map. For example, Figure 1.22 shows the results obtained by making the assumption that the perimeter of the mirror should have approximately 0 diattenuation. This is implemented by adjusting the piston terms of for each map to minimize the diattenuation near the map perimeter. This reduces the offset between the calculated and input diattenuation. Ultimately this step was not implemented in the diattenuation data reduction because there was not compelling a priori knowledge of the mirror's diattenuation assumptions made in this manner have significant impact on the result. The diattenuation results presented here should be understood as a giving an approximate size and shape of spatial diattenuation variation with any constant diattenuation present in the mirror lost.

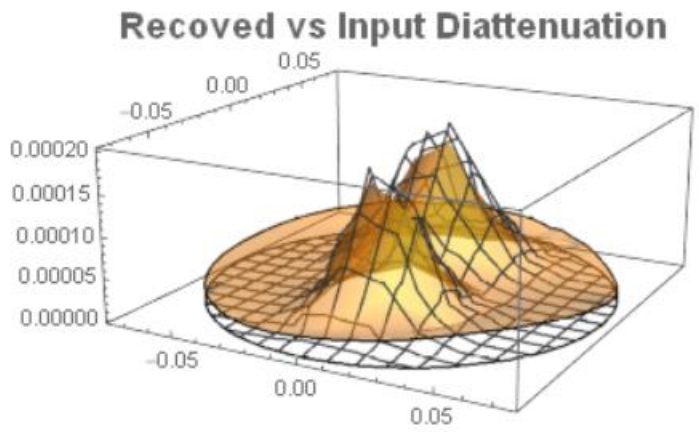

Figure 1.22. The recovered diattenuation (orange) vs the input diattenuation (mesh). There is an offset in the recovered diattenuation that is not present in the input. The recovered diattenuation also has lower peak values than the input.

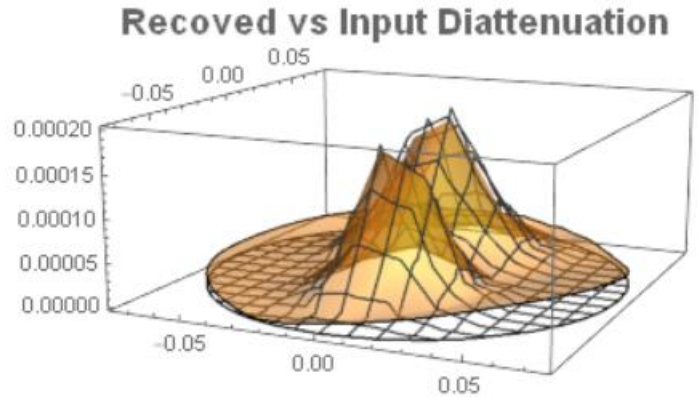

Figure 1.23. Modified data reduction approach where assumptions are made about the perimeter values of the sin and cos frequency components.

1.5.4 Separating Mirror Signal from Systematic Effects

All measurements in this section were performed at 450 nm. To distinguish between properties of the mirror and potential systematic effects, multiple measurements of the same mirror were performed with the form birefringence polarimeter rotated about its axis. Artifacts caused by the form birefringence polarimeter itself will appear stationary as it rotates. Mirror properties will rotate relative to the form birefringence polarimeter detector

by remaining stationary on the mirror. Figure 1.24 and Figure 1.25 show that the features measured are indeed stationary with physical position on the mirror even as the polarimeter rotates. The magnitude of retardance and diattenuation measured was quite small, 0.002 radians of retardance and diattenuation of 0.00025.

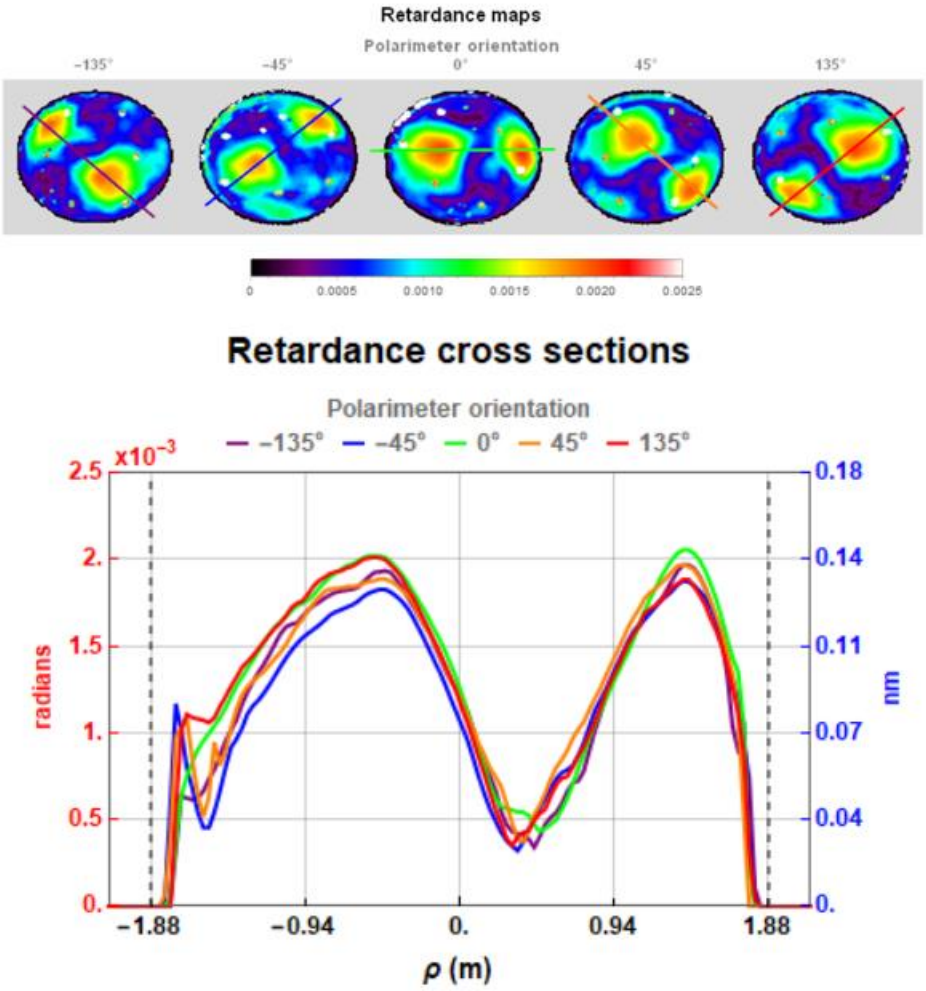

Figure 1.24. Retardance maps acquired with different polarimeter orientations.

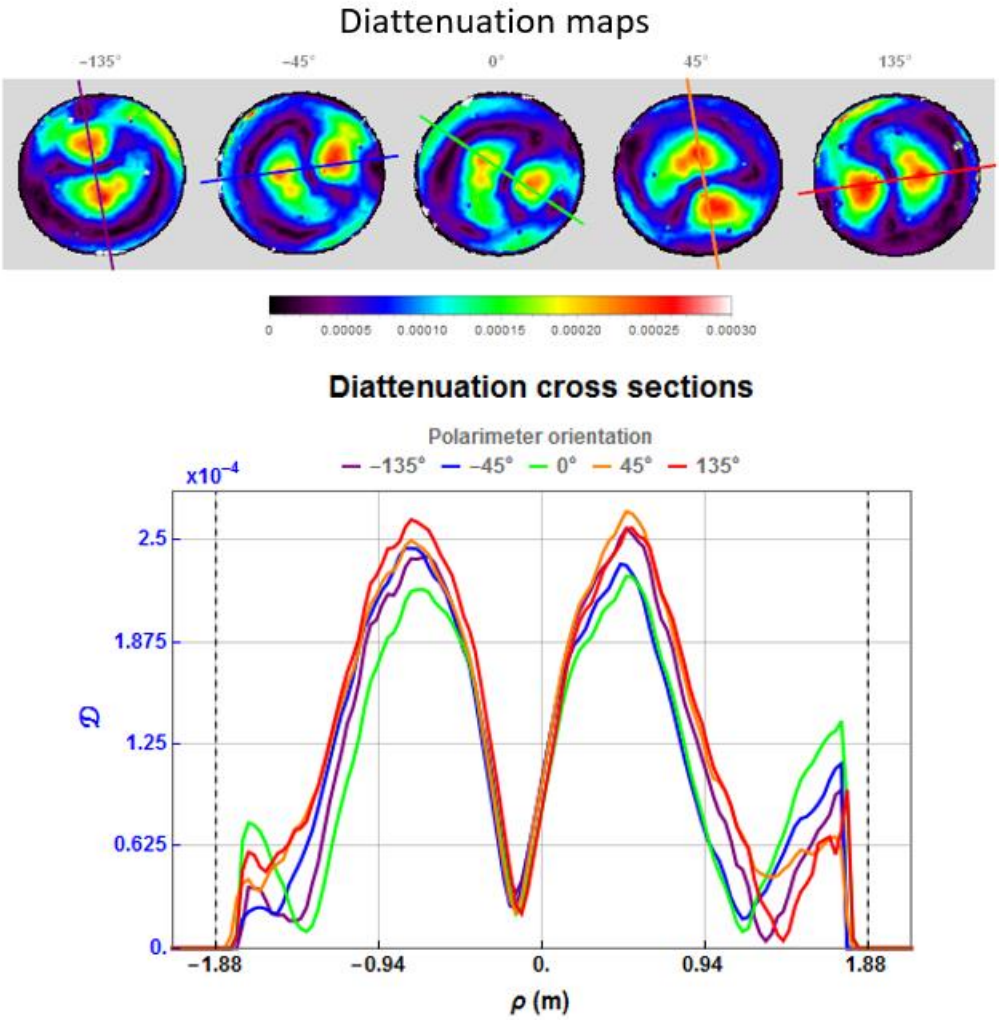

Figure 1.25. Diattenuation maps acquired with the polarimeter at different orientations.

The figures each include the same five complete measurements. The five spatial maps show the mirror properties from the rotating reference frame of the polarimeter. Similarly placed cross sections from each measurement are plotted together also. The retardance is an order of magnitude larger than the diattenuation using the leakage between crossed polarizers metric.

1.6 Conclusion and Future Work

The form birefringence of a large diameter mirror was measured for the first time. The mirror had a peak retardance of 0.002 radians about 3/1000 waves, and a peak diattenuation of 0.00025. These measurements were repeated at several system orientations to verify they were a property of the mirror and not the form birefringence polarimeter. The polarization components of interest were encoded onto different frequency components of the signal produced by measuring the minimum transmission and its orientation for different analyzer angles, further distinguishing the polarization from other sources of radiation reaching the CCD.

More work should be done to understand how this type of form birefringence would impact the design requirements for exoplanet missions. Davis has begun this effort by applying the results discussed here to his HabEx model. He modeled the polychromatic point spread function for perfect reflection from the primary mirror, isotropic reflection with polarization aberrations included, and polarization aberrations plus form birefringence. He found that the form birefringence causes about 2 orders of magnitude reduction in contrast from the isotropic case as shown in Figure 1.26 [19].

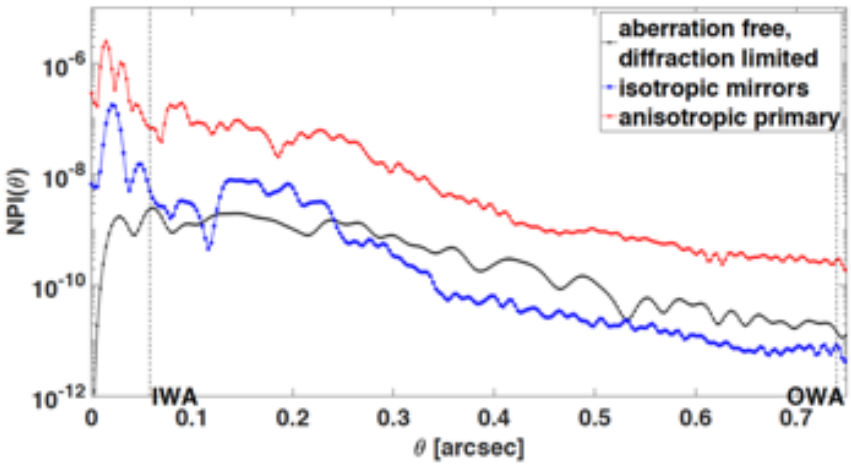

Figure 1.26. Comparison of normalized point spread function of HabEx with perfect primary mirror coating (black), polarization aberrations from reflection at mirrors included (blue), and with form birefringence included (red). [19].

Additional measurements to either reproduce the results here or to test other large mirrors would provide useful information, especially if one instrument could measure multiple large mirrors coated by different methods.

CHAPTER 2

POLARIZATION STATE GENERATOR 2 (PSG-2): POLARIZATION CALIBRATION AND TESTING INSTRUMENT

2.1 Introduction

The University of Arizona Polarization Lab designed and delivered a polarization state generator (PSG-1) to JPL to provide a calibration and testing standard for MultiSpectral Polarimetric Imager (MSPI) [41, 42]. More recent versions of MSPI have a new focal plane with more spectral bands over a larger range of wavelengths than the PSG-1 accommodates. PSG-1 uses modular LED illumination so there is potential to expand its spectral range by creating, testing, and calibrating additional LED modules at the new wavebands. While the modular illumination allows PSG-1 modification to meet new spectral requirements, the intrinsic drawback of illuminating one waveband at a time becomes more inconvenient as the number of wavebands increases. The field of illumination of PSG-1, +/- 2.25˚, must be stepped across the MSPI field of view, +/- 31˚, by rotating MSPI about its entrance pupil. The alignment of PSG-1 to MSPI is critical to PSG-1's effectiveness as a calibration standard. The combination of switching out multiple LED modules while precisely stepping across the field would result in a time-consuming calibration process requiring constant human involvement. For these reasons the UA Polarization Lab was tasked with providing a second-generation polarization state generator (PSG-2) that improve usability and reduce calibration time by using white light illumination and increasing the instantaneous field of view [41, 42].

2.1.1 MSPI Optical System Overview

JPL's MSPI camera currently exists in lab-, ground-, and airplane-based platforms and is scheduled for a space-based platform. While the optics and electronics vary over the iterations of the camera, the polarization modulation scheme and imaging method remain consistent. MSPI operates as a push broom camera, having a large field of view in one direction that is swept across the other direction to form an image. Each channel of the detector consists of a single row of pixels covered by a spectral filter and, in some cases, a linear polarizer at either 0˚ or 45˚ [43, 44, 45].

The push broom architecture causes MSPI's footprint to move along the Earth's surface during data acquisition. The full set of polarization measurements must be acquired over a smaller interval than the line repeat time. MSPI accomplishes rapid retardance modulation with dual photoelastic modulators (PEMs) driven at their resonance frequencies. The resonant frequency of a single PEM is too high to be useful for this application, but the combination of two PEMs with slightly different resonant frequency creates signal with a much lower beat frequency. A dual PEM system with a beat frequency of 23 Hz provides linear retardance modulation. Modulating the linear retardance modulates the circularly polarized component and one linearly polarized component of the incident light. The light reflected from the Earth's surface has very little circular polarization and MSPI needs to measure both linear components. Quarter wave linear retarders, placed before and after the dual PEMs, change the modulating linear retardance to modulating circular retardance, which will modulate both linear components of the incident light. Over one beat period, the two linear Stokes parameters are encoded onto

Bessel functions. The integration time of approximately 1 ms is long enough to average out the high frequency modulation but short enough to sample the Bessel function adequately [43, 44, 45].

Figure 2.1 shows the layout of Ground MSPI which will be used throughout this chapter as the default MSPI optical system. The ray trace shows the ray bundles associated with 5 pixels spaced along the same detector row that span the +/- 31˚ field of view. In object space ray bundles are collimated and have a "smile" due to the off-axis nature of the telescope. The details of the polarization modulation scheme and optical design will not have a large impact on the design of the PSG-2 but telescope smile and the entrance pupil location and size will end up impacting the design.

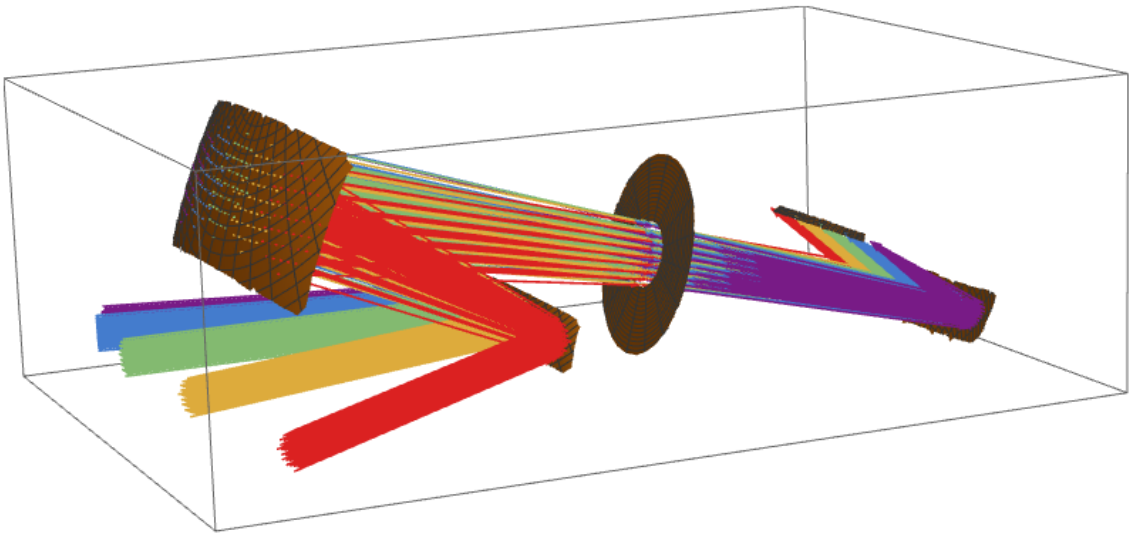

Figure 2.1. Ground MSPI optical system with ray trace demonstrating 5 field angles.

Figure 2.2 shows the approximate focal plane layout for MSPI cameras. Each spectral and polarimetric band reads out on a single row of pixels that provides the

instantaneous +/- 31˚ field of view. Images are formed for each spectral and polarimetric band by scanning the detector up or down.

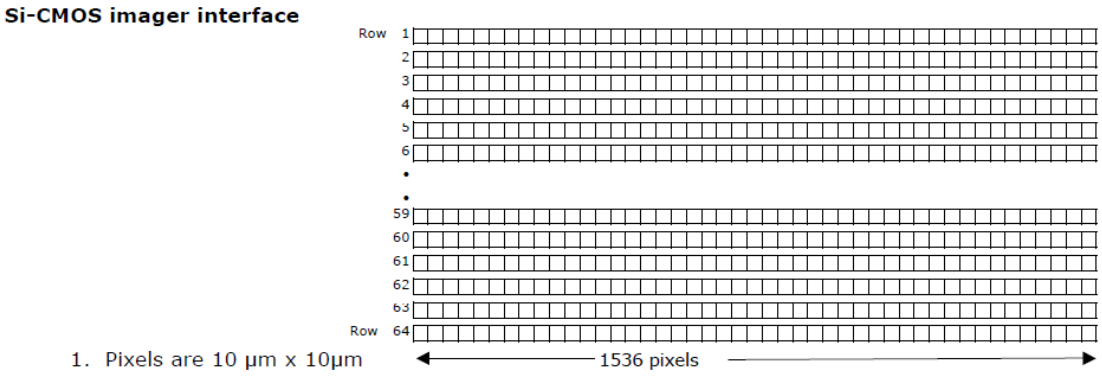

Figure 2.2. Approximate MSPI focal plane layout.

2.1.2 Polarization Calibration and Testing Standard

The PSG-2 needs to provide illumination to both calibrate and test MSPI cameras. The MSPI cameras have a defined calibration scheme of imaging fully linearly polarized illumination at orientations 0˚ to 350˚ in 10˚ steps. The calibration is performed pixel by pixel. In typical operation, MSPI cameras will be imaging natural scenes that have a low degree of linear polarization (DoLP) and approximately 0 circular polarization [46, 47, 48]. To provide the required illumination for calibration the PSG-2 needs to output linearly polarizer light with variable orientation. It also needs to produce partially polarized light at various DoLP to verify the instruments accuracy at polarization levels more typical of operating conditions. The PSG-2 must also provide a mechanism to allow easy and repeatable alignment with MSPI's focal plane.

It is important to determine the properties that affect the quality of a calibration or test standard with respect to calibrating MSPI cameras. For calibration the illumination

should be as close to 100% polarized as possible with the orientation controlled to a high degree [49, 50]. MSPI's entrance pupil should be fully illuminated for all fields being calibrated. The test system needs to provide illumination with DoLP and orientation known to a high degree. The DoLP will vary with field; the degree to which this can be managed depends on the accuracy and repeatability of the alignment between PSG-2 and MSPI. With perfect alignment, a known field dependence can be accounted for so that it does not adversely affect testing. Pupil dependent polarization would create a poorly defined illumination polarization state and degrade the PSG-2's ability to act as a calibration source or a testing standard. The expected DoLP measured by a polarimeter in these conditions would depend on the Jones pupil of the polarimeter itself.

2.1.3 Design Requirements

PSG-2 design requirements focus on improving aspects of the PSG-1 based on experience gain during its implementation for calibrating ground-MSPI. Table 2.1 gives the complete design requirements for the PSG-2.

PSG-2 Requirements	Value
Illumination DoLP	0%, 1%, 5%, 10%, 20%, 40%, 100%
Illumination AoLP	Variable over 360°
DoLP uncertainty	<0.02%
Illumination radiance	>10% of Earths reflected + upwelling radiance
Illuminating field	+/- 3°
Spacing from MSPI EP	>9 inches from final PSG-2 hardware to MSPI EP

Bandwidth	Cover all MSPI wavebands instantaneously

Table 2.1. PSG-2 design requirements.

The requirements define a set of polarization states that must be generated, over a specified spectral band, field of view, and radiance, with a DoLP uncertainty less than 0.0002. Functionally this means that, during MSPI testing, the generated DoLP of any pixel in the field of view is known to within 0.0002. The generated DoLP does not need to be within 0.0002 of the DoLP values listed in the requirements, which represent approximate targets. The field of view and wavelength specifications aim at improving usability and measurement time. The +/-3˚ PSG-2 field of view reduces the number of steps needed to span the MSPI field. The field also covers all of the MSPI spectral and polarimetric bands. Coupled with the broadband spectral requirement, the larger field allows for simultaneous calibration or testing of all MSPI bands. This reduces the number of measurements required for calibration from about 45 to 10. There specification on distance between MSPI EP and any PSG-2 component ensures that MSPI can rotate to any required field position without obstruction.

2.2 PSG-1 Review

The PSG-1 design provided light-efficient, partial polarized illumination for verifying MSPI calibration. This section reviews the PSG-1 design to determine what concepts are potentially useful for the PSG-2. It will focus specifically on the requirements of a polarization standard and how well the PSG-1 accomplished them. This includes reviewing the physical optical system and the defined calibration and testing procedures.

2.2.1 System and Calibration Process Overview

Figure 2.3 shows a layout of PSG-1 interfaced with a MSPI camera. The PSG-1 achieves its most fundamental task, of filling the MSPI entrance pupil over a +/- 2.25˚ instantaneous field of view, using an efficient Koehler illumination system. A lens images the PSG-1 light source, the output of an LED coupled into a light pipe, onto and overfilling the MSPI entrance pupil. The lens also brings MSPI's object plane from infinity to one focal length in front of the lens. An aperture placed at the front focal plane of the lens defines the PSG-1 illumination field. The LED light pipe pair produces nearly unpolarized light. A tilted, plane-parallel plate, placed in collimated space after the lens, will induce some degree of polarization due to the polarization dependence of refraction at oblique incident angles as defined by Fresnel laws. A motorized rotation stage controls the plate tilt angle to provide accurate and repeatable control of polarization. A half-wave retarder rotates the polarization state to the desired orientation [41, 42].

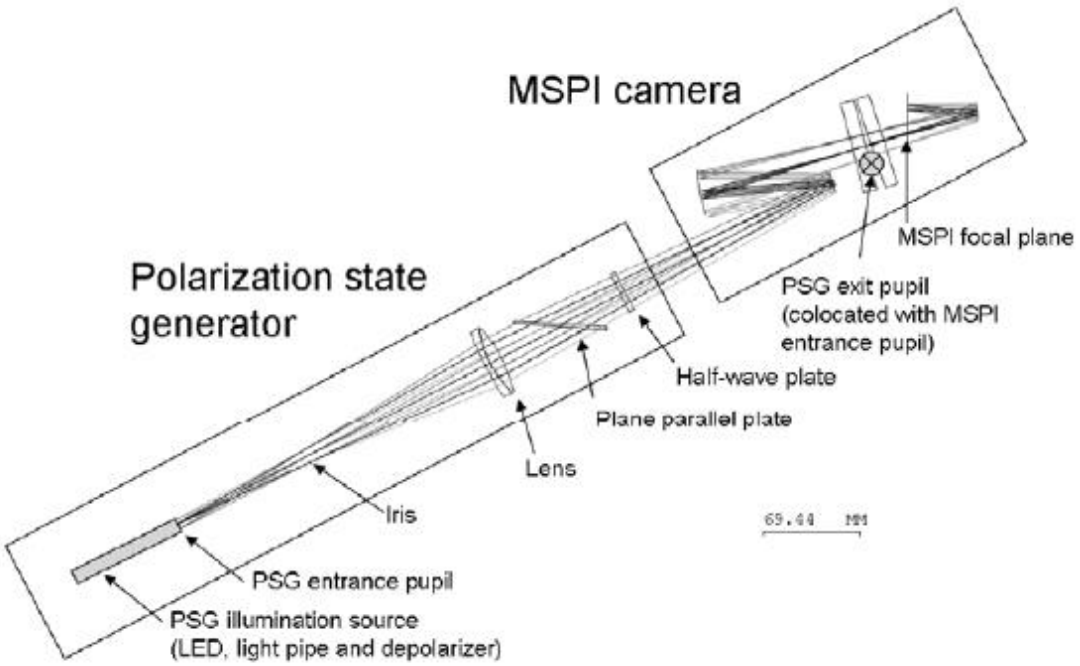

Figure 2.3. Layout showing PSG-1 interfaced with MSPI [41].

Calibration and testing consisted of measuring the PSG-1 DoLP field and pupil dependence along with a number of other tests that are not discussed here. To measure the DoLP field dependence, a small aperture was raster scanned in the field plane while the DoLP was monitored by rotating a polarizer in front of a single channel detector at the PSG-1 exit pupil. This provided high SNR DoLP measurements with resolution defined by the aperture size. To determine the DoLP pupil dependence, a camera acquired images of the PSG-1 exit pupil through a rotation polarizer. Both calibration procedures will be revisited during PSG-1 analysis.

2.2.2 Field Dependence

As stated previously, the actual DoLP value is not strictly defined. Field dependence only becomes an issue when it increases the DoLP uncertainty. A set of rays

covering the PSG-1 field are traced through the four different plate tilt settings to determine the DoLP field dependence. Each field is defined by aiming a ray from the center of the light pipe at a point in the object plane Figure 2.4 shows the PSG-1 Polaris-M model and four ray traces used in determining the DoLP field dependence.

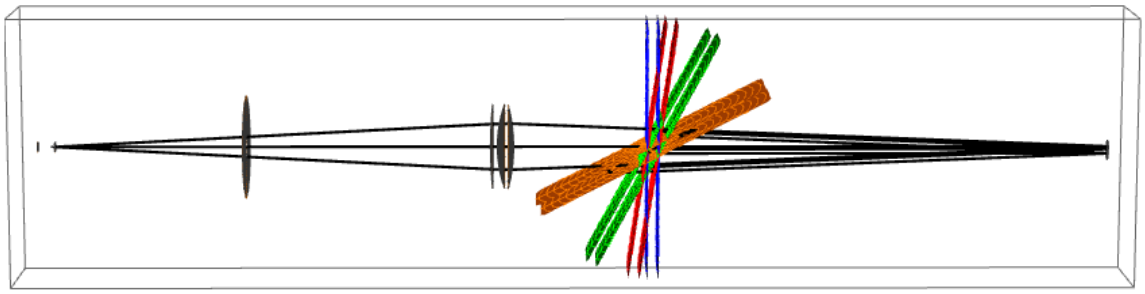

Figure 2.4. Ray trace of PSG-1 performed at 4 plate tilt angles. Only the max, min, and center field rays are plotted.

The DoLP field maps, shown Figure 2.5, give the expected field dependence over a +/- 2.5° field of view. For non-tilted plate, the DoLP increases quadratically from 0 at the center field. As the plate angle increases the linear component of the DoLP field dependence dominates. This is the result of looking at the approximately quadratic DoLP field dependence through a small window centered at increasing angles.

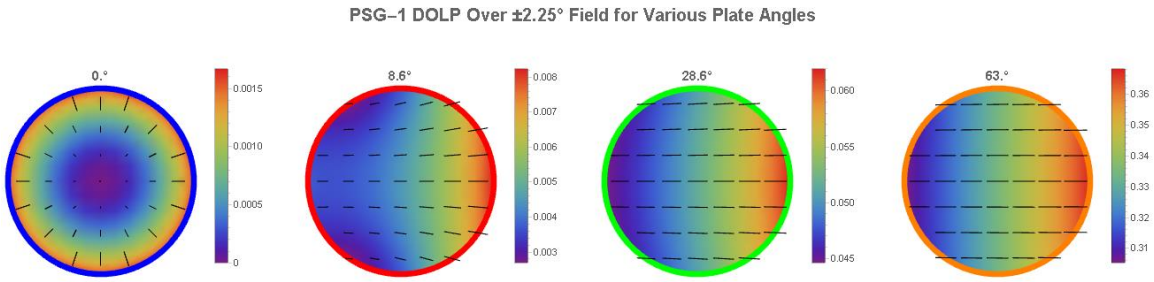

Figure 2.5. PSG-1 field dependence.

Figure 2.6 shows the slope of DoLP in units of DoLP per pixel for cross sections of the DoLP field maps. For the most tilted plate, the DoLP slope varies from 0.0005 to 0.00065 DoLP per pixel. Alignment uncertainty between PSG and MSPI must be less than a pixel to hit the DoLP uncertainty spec for the PSG-1 and better than half a pixel to reach the updated spec. Subpixel alignment positioning of circular apertures is certainly possible for 2D detector arrays [51, 52, 53]. The PSG-1's LED source illuminates at most three rows of MSPI pixels, one intensity band and two polarization bands. The other rows will have spectral filters for different wavelengths. This will reduce the effectiveness of relying on the image of the aperture for alignment.

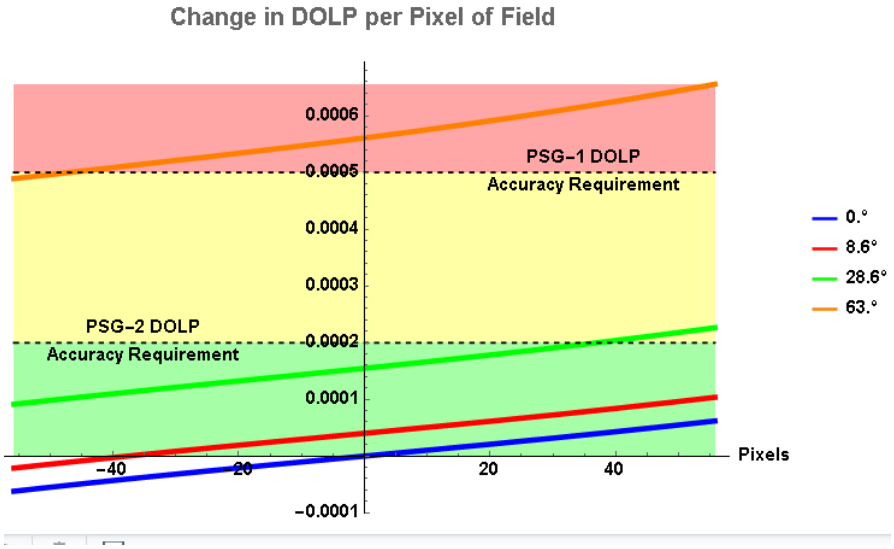

Figure 2.6. DoLP slope in units of DoLP per pixel for cross sections of the DoLP maps.

The PSG-2 will be illuminating more rows of pixels than the PSG-1 but it would still have very few pixels available to estimate the aperture position. With the tighter DoLP uncertainty specification, relying on subpixel alignment based on a small number of pixels

is not a desirable approach. A partial polarization generation scheme with weaker field dependence is preferable.

2.2.3 Pupil Dependence

During the original analysis and tolerancing of PSG-1, Mahler noted that pupil DoLP and intensity non-uniformities could reduce the quality of calibration or play a role in pupil alignment sensitivity. The calibration method relied on measuring the DoLP of the entire PSG-1 exit pupil while scanning a small aperture through the field plane. The PSG-1 exit pupil overfills the MSPI entrance pupil so MSPI will only collect a portion of the light used during calibration. For exit pupils with uniform DoLP, the output polarization state averaged over the MSPI entrance pupil will be insensitive to intensity non-uniformities or pupil misalignment. In the presence of DoLP non-uniformities, the intensity non-uniformities become relevant as a weighting factor. In this case, the DoLP averaged over the MSPI entrance pupil depends on the sub region of the PSG-1 exit pupil being sampled. With known pupil non-uniformities, the alignment sensitivity can be characterized and toleranced accordingly.

The PSG-1 exit pupil uniformities were measured by scanning a CCD across the exit pupil plane and stitching multiple images together to show the full pupil. The measurement was performed without a field mask so it represented the pupil dependence averaged over field. Figure 2.7 shows the irradiance, DoLP, and irradiance weighted DoLP pupil uniformities. The black circle in the rightmost image represents the size of the MSPI entrance pupil. A simulation showed that two measurements, one integrating over the full PSG-1 illumination and one integrating over just a MSPI pupil sized area at the center,

would result in a 0.00005 difference in DoLP. This indicated that measuring the full PSG-1 exit pupil was a sufficiently accurate method to determine the DoLP as seen by MSPI. The lateral pupil alignment tolerances were determined by convolving the intensity weighted DoLP map with a mask representing MSPI's entrance pupil [41, 42].

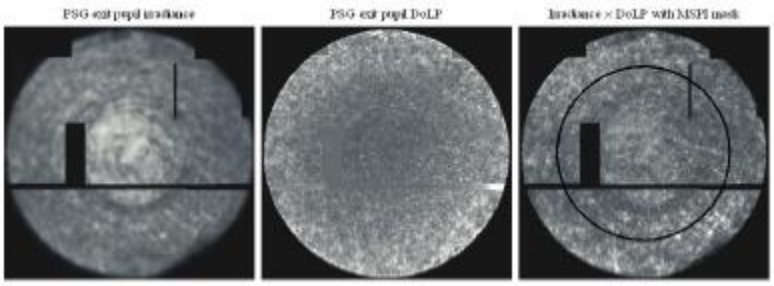

Figure 2.7. PSG-1 exit pupil irradiance, DoLP, and irradiance weighted DoLP images [41].

The analysis and calibration focused on determining the average DoLP integrated over MSPI's entrance pupil and whether the calibration approach of measuring the full PSG-1 exit pupil was sound. The intensity and DoLP uniformity at the PSG-1 exit pupil was characterized and used to determine alignment tolerances. The field dependent DoLP pupil uniformity was not measured even though MSPI's separates the field across its pixels. This testing approach was blind to even large pupil dependence as long as it was symmetric in field.

By not measuring the field dependent pupil non-uniformity the alignment tolerances could not be sufficient for all illuminated pixels. Additionally, pupil non-uniformity in the PSG-1's pupil is problematic because it creates a degree of complexity that is impossible to characterize with an imaging polarimeter. If the polarimeter optics are free of apodization and polarization aberrations then the polarization averaged over the

pupil will be well defined. In real polarimeters the measured DoLP will depend on polarization aberrations and not be an accurate tool for comparing measurements performed on different instruments. More generally, it is a poor representation of the typical illumination MSPI will see in operation. MSPI's pupil subtends a tiny angle from the ground so illumination polarization and intensity will be very nearly constant.

The PSG-1 exit pupil uniformity and the measurement method used to test it are reviewed using polarization ray tracing. Figure 2.8 shows a ray trace of five different PSG-1 fields, each filling the exit pupil. The AR coating on PSG-1's lens is unknown so a typical broadband AR coating is used. The traced fields are on-axis and maximum and minimum x and y. The ray bundles for these five fields interact with different portions of the lens. This results in different incident angles for each field which leads to different polarization aberrations.

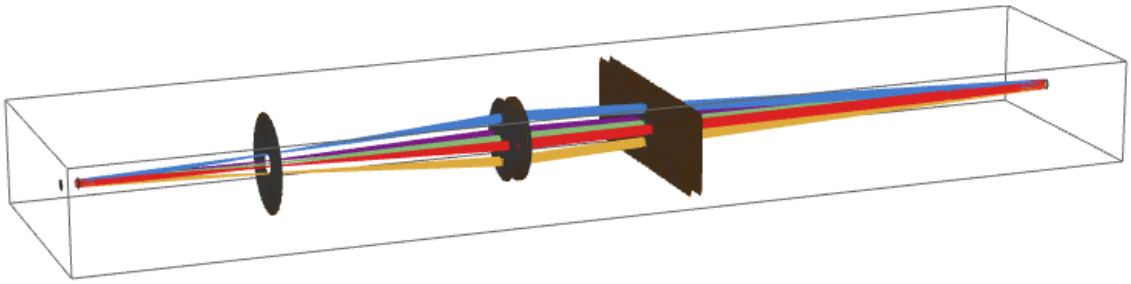

Figure 2.8. PSG-1 ray trace showing rays filling the MSPI entrance pupil for 5 different field angles.

The DoLP pupil variation for the five fields in Figure 2.8 are calculated from the ray trace results assuming unpolarized illumination. The DoLP for each of the H = 1 fields

varies by about 0.001 across the pupil, twice the DoLP accuracy requirement. The off-axis fields do not present well-defined polarization illumination with respect to the PSG-1's application. Even if the MSPI pupil is uniform enough that a non-uniform illumination with well-known average DoLP is sufficient, the alignment tolerances were based on the pupil variation averaged over field instead of the field-dependent pupil variation. The DoLP at the larger fields will be more sensitive to alignment than expected.

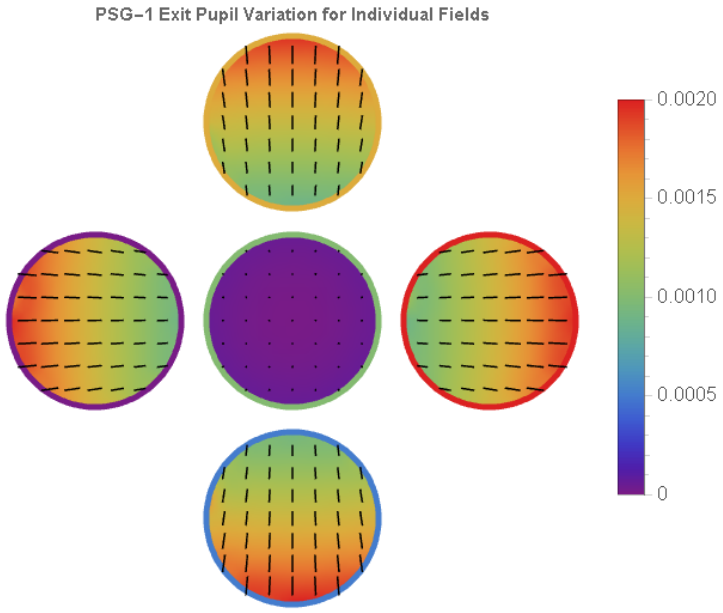

Figure 2.9. DoLP non-uniformity for different PSG-1 illumination fields.

Figure 2.10 shows the simulated pupil non-uniformity averaged over the five traced fields and the measured DoLP. In both cases the pupil dependence is close to uniform with the DoLP increase towards the edge of the pupil. The DoLP of the simulation is an order of magnitude smaller than the measured DoLP which averaged to 0.00056. This suggests the lens in the PSG-1 had no coating or a less effective coating than the one used in the

model. The model still effectively demonstrates how much larger field dependent pupil non-uniformities are masked when averaged over field.

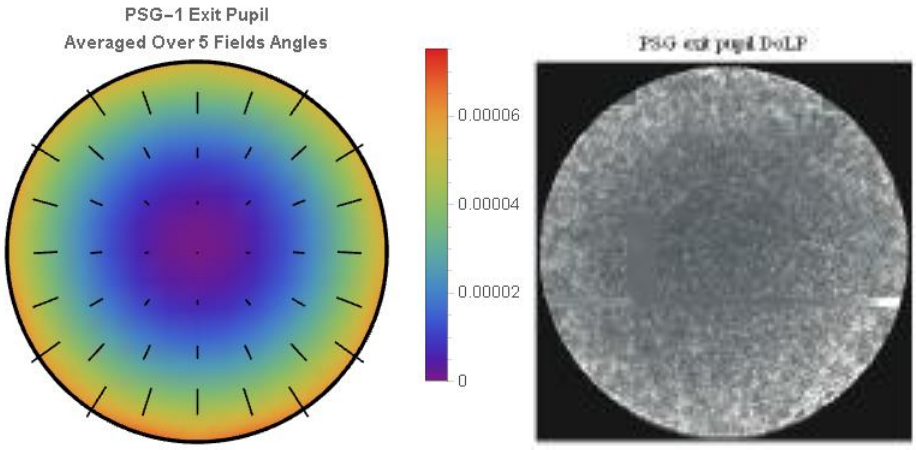

Figure 2.10. Left, Pupil variation at PSG-1 exit pupil when averaged over 5 fields. Right, Measured DoLP pupil dependence for PSG-1, average over all fields [41].

Review of pupil uniformity calibration and test procedures from PSG-1 determines that the field-averaged DoLP pupil dependence did not accurately represent the pupil dependence found off-axis. This results in illumination DoLP that becomes more poorly-defined with increasing field. This issue results from different illumination fields transmitting through different sub-apertures of the PSG-1 lens. The spacing between the MSPI entrance pupil and the lens combined with the required field of view determines the separation of fields at the lens. The MSPI/lens spacing must be large enough to contain the tilted plate and required physical clearance. With the PSG-2 spectral requirements, the AR coating performance would likely to be worse than PSG-1 increasing the DoLP pupil dependence. The efficiency and stray light control of the PSG-1 illumination scheme are advantageous but require an active path lens causing pupil dependent DoLP that varies by five times the PSG-2 accuracy requirement. While PSG field dependence can be readily

addressed through calibration, pupil dependence cannot. The problem is compounded if the PSG pupil needs to be able to rotate relative to MSPI, as is the case with PSG-2.

2.2.4 Multiple Internal Reflections in Plate

The DoLP induced by unpolarized light passing through a tilted plane-parallel plate depends on the number of overlapping ghost beams caused by multiple reflections within the plate. This effect was noted in previous analysis as one of the reasons the PSG-1 calibration scheme was modified from primarily theory based to primarily empirical. This section advances the PSG-1 model to account for multiple reflections to determine if the empirical approach take effectively accounted for any related issues.

Figure 2.11 shows rays traced towards the top, middle, and bottom of the MSPI entrance pupil for the on-axis field. One of the rays only consists of the light directly transmitted through the plate, one consists of directly transmitted light plus the first ghost reflection, and the third consists of directly transmitted light plus the first two ghost reflections. This happens because the plate tilt angle determines the source position required to have a co-propagating ghost reflection for any given ray. When the required source position occurs outside of the physical source a co-propagating ghost cannot occur. The result of varying ghosting properties across the pupil leads to plate angle dependent pupil non-uniformity.

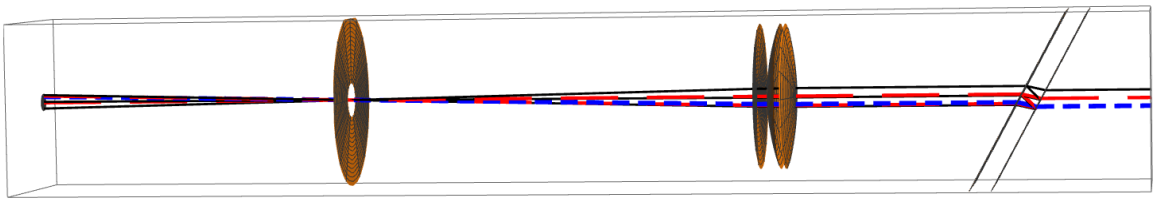

Figure 2.11. The number of possible multiple internal plate reflections depends on where in the pupil the ray originates.

The number of ghost reflections contributing to PSG-1 illumination varies across the pupil. This variation causes the DoLP to vary across the pupil as well. As discussed in the previous section, DoLP pupil variation cannot be adequately corrected by calibration, making any DoLP pupil variation larger than the accuracy specification problematic. To determine the impact this has on the PSG-1s ability to function as a polarization standard, a revised model of the PSG-1 implements non-sequential ray tracing. The non-sequential ray trace "kill ray" conditions stop tracing on any ray that encounters the same surface 4 times to limit the size of the ray trace. The output of the ray trace contains all rays associated with direct illumination and the first two ghost reflections. To simplify data reduction, the ray trace implemented deliberate input ray sampling that resulted in ghost and direct illumination rays overlapping in space at the PSG-1 exit pupil. This allowed for simple sorting of the exit pupil rays into subgroups based on exit pupil location. The model treats rays in a subgroup as co-propagating and determines the total polarization properties by summing the rays' Mueller matrices.

Figure 2.12 shows exit pupil DoLP maps determined from the non-sequential ray trace. The first row shows the DoLP calculated if the model ignores ghosting, the second row includes one ghost reflection, and the third row includes two ghost reflections;

columns correspond to different fields with the center column being on-axis. The model including only direct illumination shows a field DoLP variation of about 0.015 but near uniform pupils. The second and third rows, which look identical because only a small unsampled portion of the pupil can contain two ghost rays, show similar field dependence but very different pupil dependence relative to the first row. When the model includes ghosting effects the exit pupil DoLP exhibits a discontinuity where the DoLP changes by about 0.005, about an order of magnitude larger than the required accuracy. The size of this discontinuity will increase with plate angle until the shearing effect becomes large enough that the first ghost reflection no longer overlaps with the direct illumination. This effect went unnoticed during PSG-1 calibration and testing because the pupil variation testing was performed without the plane-parallel plate in the system.

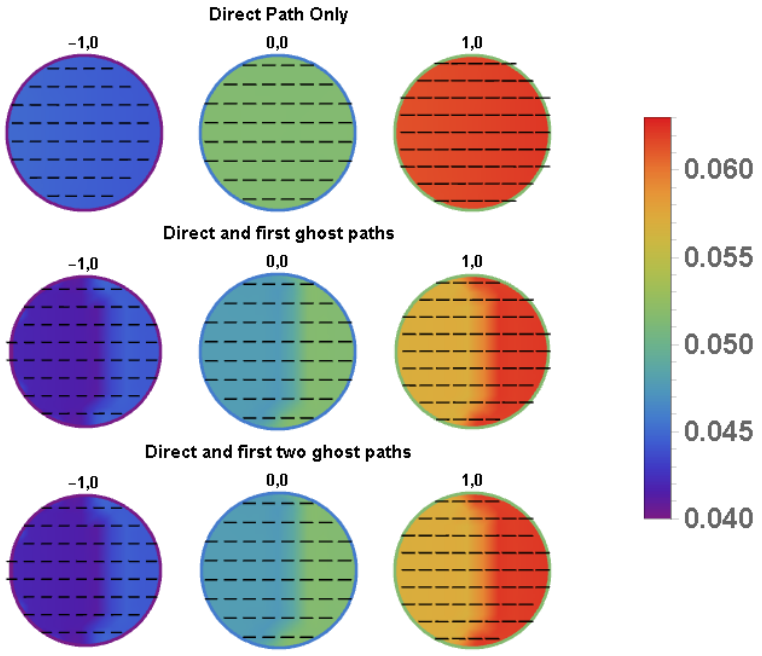

Figure 2.12. Pupil DoLP variation for three different field angles and determined first by ignoring ghosting, second by allowing single ghost reflection, and third by allow two ghost reflections.

This type of DoLP pupil dependence is problematic as a polarization standard for a couple reasons. First, assume an ideal situation where MSPI's entrance pupil is perfectly uniform. In this situation the requirements on a polarization standard are simplified to accurately knowing the field dependence of the pupil averaged polarization presented to the camera. The discontinuity in DoLP across the pupil makes even this potentially problematic because of increased sensitivity to alignment. More realistically, MSPI has pupil dependent polarization properties that vary with field angle. During testing, multiple images of PSG-1 illuminated different sections of MSPI field of view. Each section will have some field dependence due to the expected PSG-1 field dependence, plus an additional field dependence caused by the field dependent MSPI pupil viewing a

polarization dependent PSG pupil. In general, two different but well calibrated polarimeters would not measure the same DoLP when illuminated by PSG-1.

It is possible to work around this issue without major changes to the PSG design. The system needs to be configured so it only provides the direct illumination at the exit pupil. An instrument could achieve this by increasing shearing by either increasing the plate angle or thickness. Small plate tilts become untenable since they would require unrealistic plate thicknesses. Low values of DoLP could be generated by using plates with AR coatings at the larger tilt angles required. Alternatively, design modifications ensuring that the entire PSG-1 exit pupil has enough ghost reflections to make it indistinguishable from the infinite ghost reflection case also solve the problem. This requires reducing shearing effects by reducing plate angles or using thinner plates.

2.2.5 Requested Operational Improvements

JPL and the Polarization Lab identified additional PSG properties for improvement in generation two. These include the following: (1) increase field of view to +/- 3˚, (2) provide broadband illumination that meets radiance requirements, and (3) stationary exit pupil.

2.3 Use Insight From PSG-1 to Develop PSG-2

The PSG-2 conceptual design aims to avoid the issues found analyzing PSG-1 while also meeting the new design requirements. This section explains how addressing these issues drove the design of the PSG-2. The tilted-plate system was an effective method

for producing partially polarized light. The development of the PSG-2 begins with the assumption that tilted-plate partial polarizers are used.

2.3.1 Field Dependence

Assuming the infinitely large plates and extended source, the DoLP from tilted-plate partial polarizers depends only on propagation direction. Since DoLP field dependence can be calibrated and pupil dependence cannot, the plate-polarizer should be placed so that propagation direction through the plates maps entirely to position at MSPI's focal plane. MSPI focuses at distant objects so its object space is suitable. The partial polarizer is assumed to be the final PSG-2 element to place it in MSPI's object space.

The PSG-1 field dependence required subpixel alignment to meet the accuracy specification. The tighter DoLP accuracy requirement makes the required alignment tighter still. The PSG-2 aims to reduce field dependence to a point where alignment requirements are no tighter than one pixel. The large field dependence in PSG-1 occurs as the incident angles at the plate increase when the plate angle increases. The variation in incident angle across the PSG-1 field does not increase as plate tilt increases but the mean value of angle increases. The polarization aberrations vary quadratically with angle, so as the mean incident angle changes the variation in polarization aberrations over the field increases.

Figure 2.13 shows the field dependence of the PSG-1 for two equal and opposite plate tilt angles. Each field map appears to have close to linear variation along on axis, close to no variation along the other axis, and nearly constant orientation so the average of the maps will be nearly uniform. This can be physically realized by two plates in series with opposite tilt angles. Additionally, this configuration removes the exit pupil shift

caused by a single tilted plate and satisfies one of the new requirements. This approach was highlighted by Mahler in the future work section specifically to remove the beam shift so the system would not require re-alignment whenever the DoLP changed [41].

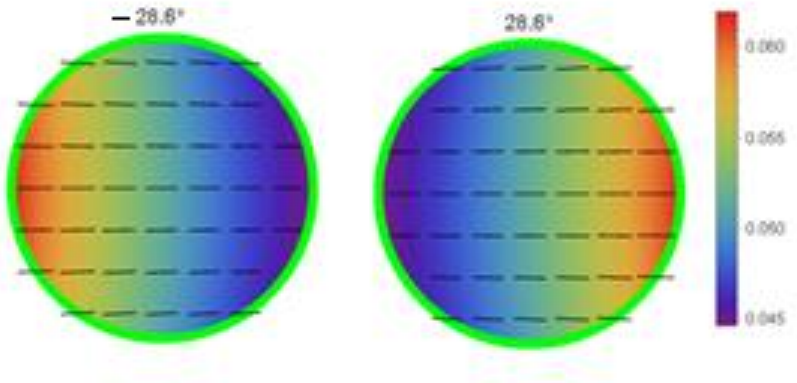

Figure 2.13: PSG-1 field dependence for to opposite plate angles.

Four sets of plates using this configuration and producing average DoLPs up to 0.4 provide models for investigating the DoLP field effects. A +/- 3˚ ray cone traced to the partial polarizer models gives the variation in DoLP expected over required PSG-2 field.

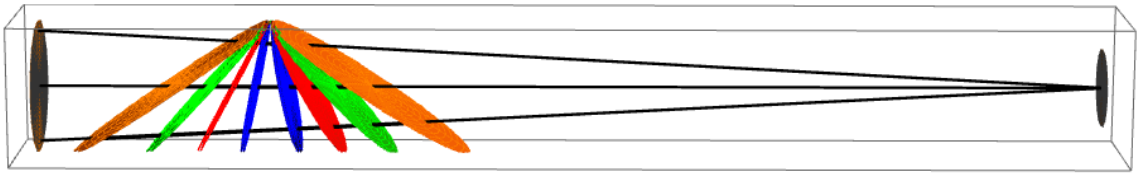

Figure 2.14. Ray trace through the PSG-2 partial polarizer for different field angles.

Figure 2.15 shows the field maps that result from this plate configuration. The lines representing DoLP magnitude and orientation look nearly constant for each map. The color scale shows the small variation in DoLP magnitude across field for each plate set. This

configuration has removed the larger linear field effect seen previously and only a higher order quadratic variation remains.

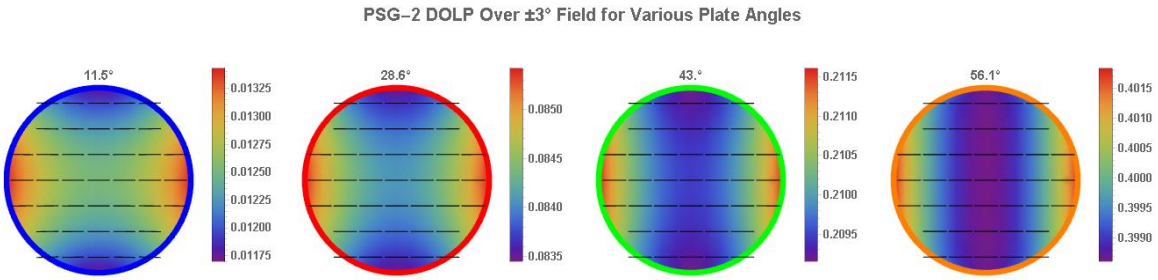

Figure 2.15. PSG-2 field maps.

Figure 2.16 shows the change in DoLP with field, expressed in pixels. For the larges DoLP plate configuration the maximum slope will be about 0.0001 1/pixel. The DoLP accuracy specification requires alignment better than two pixels. This sets the requirements for the PSG-2 alignment system once development progresses to that point.

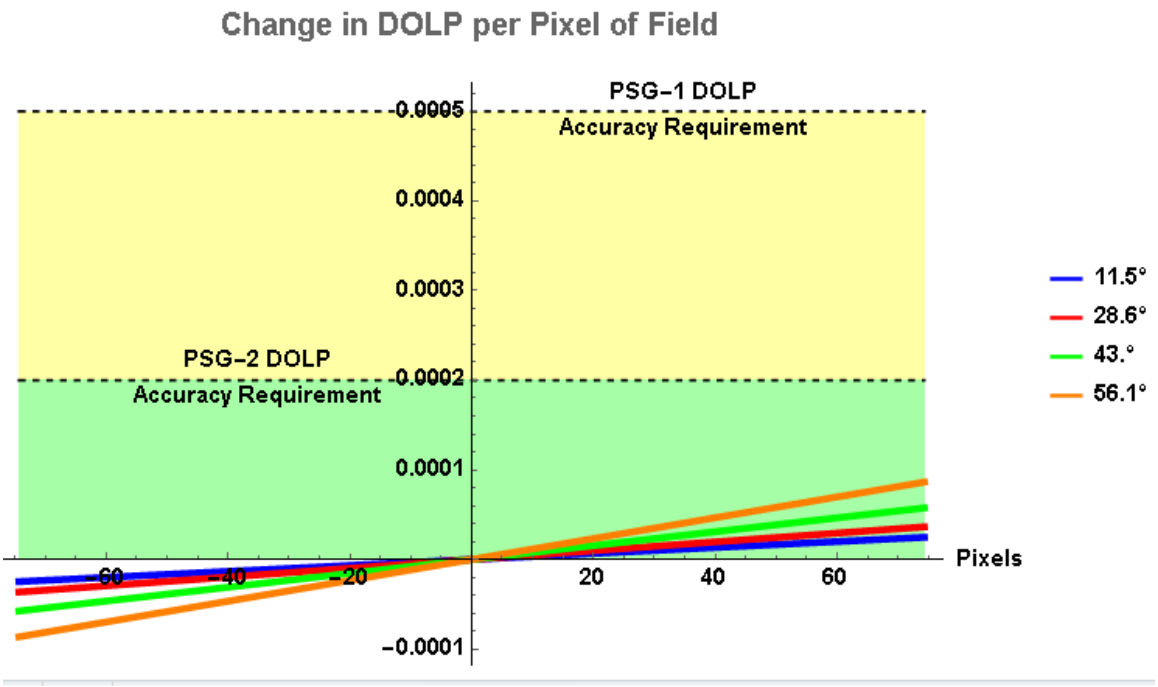

Figure 2.16. PSG-2 DoLP slope.

This completes the concept for PSG-2 partial polarizers by reducing the field dependence enough that DoLP accuracy of 0.0002 can be achieved over a +/- 3˚ field of view with a field alignment tolerance of two pixels. The next portion of the design focuses on providing illumination to the partial polarizer section.

2.3.2 Pupil Dependence

The illumination at the front of the partial polarizer section of PSG-2 must contain 5 mm collimated beams of light with propagation angles ranging from 0˚ to +/- 3˚ each propagating towards the MSPI entrance pupil. PSG-1 achieves desired illumination by placing a lens with an aperture in its front focal plane directly before the partial polarizer section. The aperture acts as a field stop for the illumination; fields in partial polarizer space correspond to points within the field stop. The source must be large enough that all

fields through the field stop will fill the MPSI entrance pupil. The source to lens distance results in an image of the source at the MSPI entrance pupil ensuring that MSPI images are not affected by source non-uniformities. This scheme provides efficient illumination over required field angles and does not require a large area source. However, since each field refracts from a different sub-aperture of the lens, the illumination will have pupil dependent DoLP that changes with field.

The PSG-2 could approach this issue by spreading the lens power over more surfaces to reduce incident angles. The expanded wavelength range will likely reduce AR coating performance and the multiple reflection issue would still need to be addressed. Instead, the PSG-2 opts for a simple but inefficient approach to illumination. The output port of an integrating sphere replaces the lens and completes the PSG-2 illumination system. As long as the integrating sphere outputs unpolarized light, this scheme does not introduce a pupil dependent polarization. Figure 2.17 shows a ray trace and pupil maps confirming the expected result.

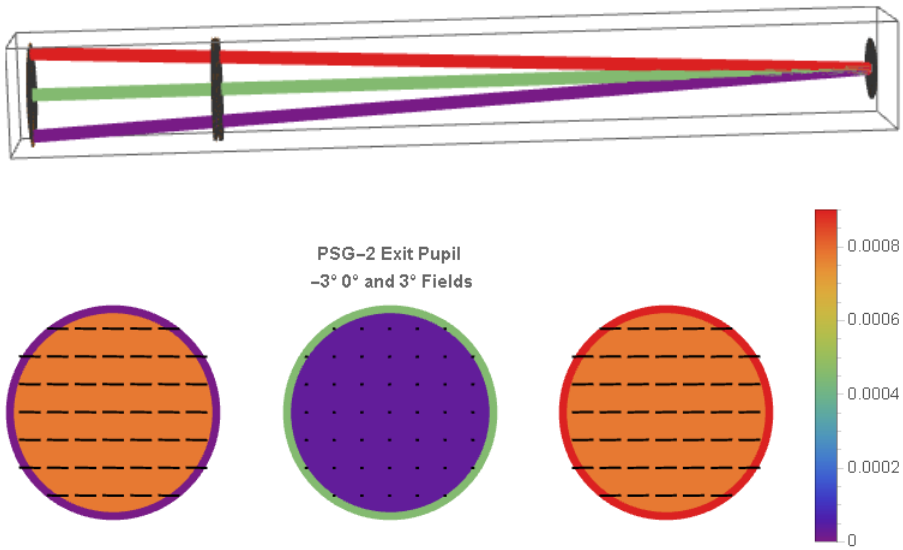

Figure 2.17. PSG-2 ray trace demonstrating uniform pupil DoLP.

PSG-2 uses a simple and inefficient illumination scheme to avoid pupil dependent DoLP. By removing the lens and field stop, the PSG-2 has also lost the natural alignment system build into PSG-1. To reach to the two-pixel alignment requirement some sort of alignment system must be included. This will be addressed during the process of turning the conceptual design into a physical instrument. Additionally, the multiple reflection issue still needs consideration.

2.3.3 Multiple Internal Reflections

The PSG-1 review demonstrated the DoLP pupil non-uniformity occured when a ghost reflection fills only a portion of the pupil. Each subsequent order ghost acts like an additional dimmer source, shifted in space, and with different polarization properties than the direct illumination. To achieve truly uniform polarization, MSPI's entrance pupil must fit into a contour of uniform number of reflections in the PSG-2's exit pupil. Figure 2.18

highlights such contours for a round source viewed through a tilted glass plate. In this configuration, the contours are oddly shaped and each one makes up a narrow portion of the direct illumination. Increasing the shearing between subsequent ghosts can expand the direct illumination contour to fill the entire pupil. This requires larger plate angles or thicker plates so generating lower DoLP states becomes untenable without adding AR coatings to reduce plate diattenuation. The PSG-2 avoids these complications by not attempting to fill MSPI's pupil with truly DoLP uniform illumination. Instead, the PSG-2 provides suifficient DoLP uniformity by ensuring that the pupil region with the fewest overlapping ghosts and a region with infinite ghosting have a DoLP difference below the required accuracy. The green highlighted region in Figure 2.18 shows the acceptable region for a situation when two ghosts sufficiently approximate infinite. The shape of this region fits MSPI's round entrance much more efficiently than the slivers of uniform DoLP. Using thinner plates or small plate angles increases the usable green portion of the pupil.

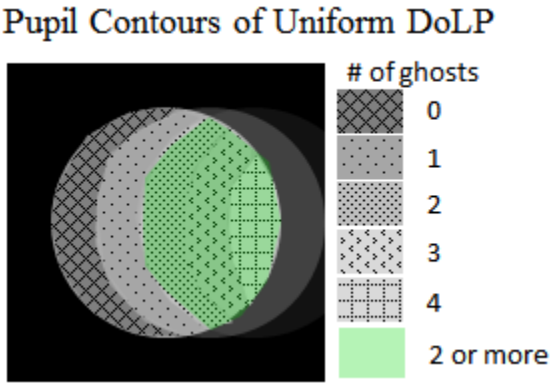

Figure 2.18. Show an example pupil where each subsequent ghost shifts further right. The uniform DoLP contours of the direct beam are highlighted.

The PSG-2 design includes margins around the required beam size at the integrating sphere exit pupil and the first tilted glass plate. Correctly selecting margin size, plate

geometry, and plate thickness, allows the direct beam and the required ghost beams to remain unvignetted at the PSG-2 exit pupil. Specific design of these components continues in the design realization section. Non-sequential ray tracing, Figure 2.19, performed similarly to the PSG-1 ghosting section, shows uniform DoLP pupils when including up to two ghost orders. If the ray trace included high enough order ghosting, the results would show DoLP non-uniformity well within the DoLP accuracy budget.

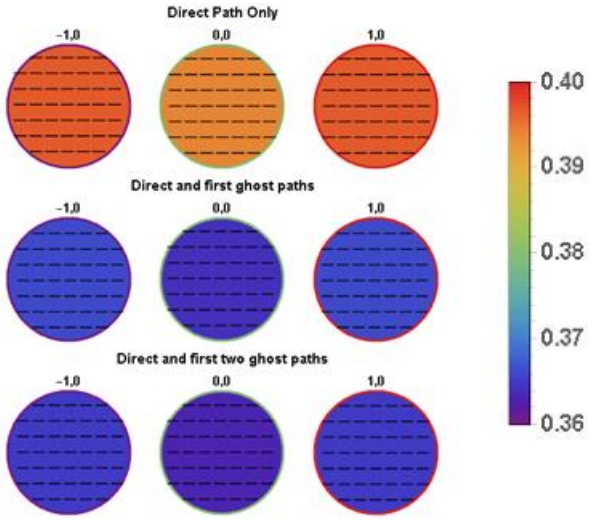

Figure 2.19. Ray trace showing the DoLP-2 design does not suffer from the multiple reflection issues found in PSG-1.

2.4 PSG-2 Design

Careful analysis of PSG-1 found a number of issues that reduced its capacity as a polarization standard. A skeletal concept of PSG-2 formed through addressing each issue individually. An additional plate added to the partial polarization scheme improves field dependence, an extended source replaces the illumination system to avoid active path optics and remove DoLP pupil dependence, and large enough padding around the required

illumination beam avoids DoLP pupil non-uniformity from ghosting. The initial concept does nothing to address the PSG-2 requirements but provides a foundation for a more viable polarization standard.

2.4.1 System Layout and Dimensions

Three system requirements affect the layout and dimensions of the PSG-2: (1) the required 9 inches of free space between the final PSG component and MSPI entrance pupil, (2) the +/- 3˚ field of view, and (3) the maximum partial polarizer DoLP of 0.4. While not specifically a design requirement, ensuring pupil DoLP uniformity impacts system layout as well. N-LAK7 glass is selected for the partial polarization plates due to its broad spectral transmission and relatively high index. To produce a DoLP of 0.4, two N-LAK7 glass plates must be tilted at +/- 58˚. Figure 2.20, shows the layout as defined by the requirements. The blank dimensions depend on ghosting requirements and each other.

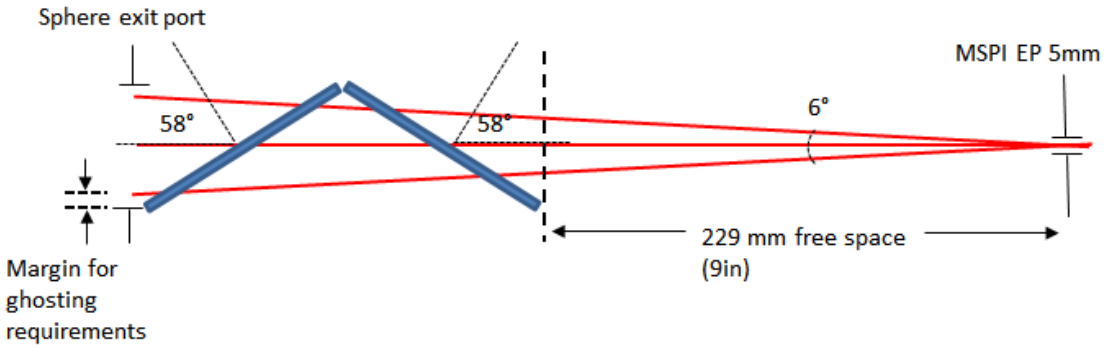

Figure 2.20. Layout based of MSPI EP spacing, DoLP, field of view, and uniform pupil.

Figure 2.21 a. shows the relative error for different orders of ghosting when compared to the infinite ghosting case. To achieve pupil uniformity within the DoLP accuracy requirement at least two orders of ghosting must combine with the direct

illumination everywhere in the pupil. Figure 2.21 b. uses the result from a. to express the ghosting accommodation margin in terms of plate thickness.

a)

Multiple Reflections	DOLP	Error
0	0.43827	0.036987
1	0.402902	0.001619
2	0.401354	0.000071
Inf	0.401283	

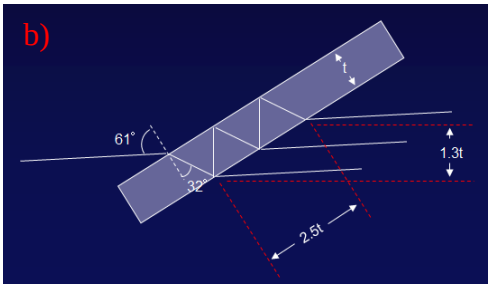

Figure 2.21. a. DoLP from combining the direct illumination with different numbers of ghost orders compared to the infinite ghosting case. b. Shearing expressed in terms of plate thickness for 2 order ghosting case.

At 412 mm from MSPI's entrance pupil the chief ray height will be 21.65 mm. An aperture size of 24.15 mm prevents vignetting over the full +/- 3˚ field of view. A plate thickness of 1 mm gives a ghosting allotment margin of 1.3 mm, extending the aperture to 25.45 mm. This convenient aperture size allows the PSG-2 to choose an off-the-shelf integrating sphere with a 2" exit port. Working through the geometric constraints established by the requirements produced a reasonable system layout to work from.

2.4.2 Partial Polarizers

The PSG-1 used a single plate mounted in motorized rotation stage to provide adjustable DoLP. A half wave retarder in a manual rotation mount followed the plate to allow AoLP adjustment. The PSG-2 must also provide adjustable DoLP and AoLP. The PSG-2 provides illumination for calibrating and testing all MSPI wavebands simultaneously. With a wavelength range extending from 355 nm to over 2 µm for

AirMSPI-2, the PSG-2 cannot use half wave retarder method to adjust AoLP. The addition of the second plate complicates the DoLP control method as well.

The PSG-2 approaches the AoLP requirement differently from PSG-1. Instead of rotating the polarization state generated by the partial polarizer, the PSG-2 rotates the entire partial polarizer, eliminating the need for additional polarization optics in the active path. This decision steers the design away from using motorized stages to adjust plate tilt angles; attempting to package stages and plates on a platform that must rotate and fit into the allotted space results in significant mechanical complications. Instead, the PSG-2 uses interchangeable partial polarizers to discretely generate the required DoLPs.

An error budget for the DoLP = 0.4 partial polarizer helps inform initial design decisions. The budget includes refractive index uniformity, ghosting, and angular errors in the same plane as the plate tilt, as shown in Figure 2.22. The analysis ignores out of plane angular errors because they have much less effect on DoLP. The initial tolerances for n and α come from a vendor's specification sheet and optical shop's fabrication quote respectively. The ghosting tolerance comes from the previous section. The remaining tolerances are determined such that the remaining DoLP error budget distributes approximately evenly. The resulting partial polarizer tilt tolerance of 0.1˚ looks reasonable, but the 25 arc second requirement on the angle between the plates corresponds to 0.01 mm, less than half mil, over the length of the plate. Even after balancing the tolerances based on sensitivity, the angle between plates specification requires machining tolerances of less than 1 mil. Instead of relying on very tight machine tolerances to achieve precise plate angles, the calibration process will be responsible for determining the plate angles.

Source	Tolerance	DOLP Error
α_1	+/- 1 arcmin	0.000062
α_2	+/- 1 arcmin	0.000062
ϕ	+/- 25 arcsec	0.00011
θ	+/- 0.1 degree	0.00013
n	+/- 10^-4	0.000051
Ghosting	>2 ghosts	0.000071
	RSS Error	0.00021

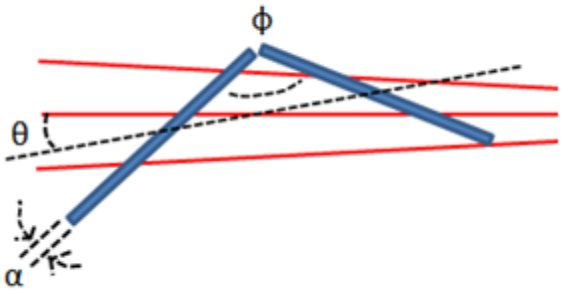

Figure 2.22. Error budget to meet DoLP requirements.

The design must allow for interchange of partial polarizers and provide 360˚ of continuous rotation while maintaining calibration. The PSG-2 design accomplishes this using a hollow motorized rotation stage to rotate a custom partial polarizer sleeve that kinematically mates with the individual partial polarizers. This allows partial polarizers to quickly and repeatably swap in and out of the PSG-2. The coupling between the rotation stage and the partial polarizer sleeve is not uniquely defined as it occurs between two planar surfaces bolted together. This connection is intended to be permanent after initial calibration.

Figure 2.23, shows a model of how the partial polarizer sleeve mounts to one of the partial polarizers. Each partial polarizer follows the same design concept but has unique face angles. The sleeve has three steel balls epoxied into recesses in the back wall surrounding a countersunk M4 hole. Two of the balls rest in a y- direction slot in the partial polarizer defining orientation and position in the z- direction (on-axis field direction). One ball sits in the partial polarizer slot along the z- direction defining the y- position. An M4

bolt through a countersunk relief in the sleeve and into a threaded hole in the partial polarizer provides tension between the parts.

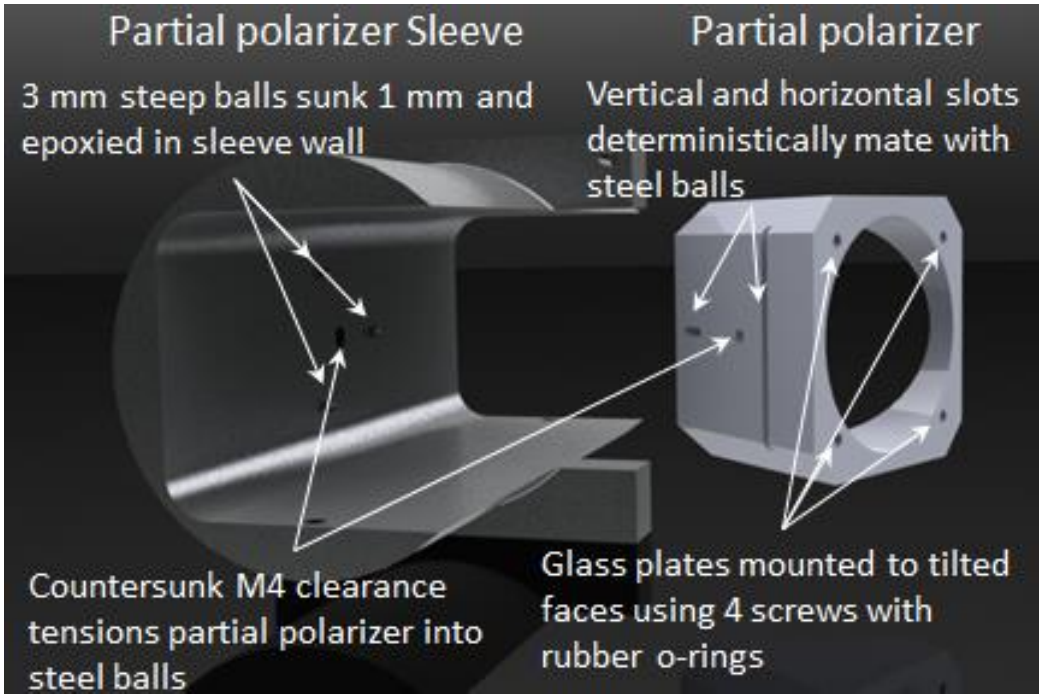

Figure 2.23. Model of partial polarizer and sleeve with mounting features highlighted.

A USR150BCC Newport rotation stage with a 3-inch clear aperture provides the required 360˚ of polarization orientation. The sleeve's outer diameter fits through the clear aperture and a flange near the middle of the sleeve bolts onto the face of the stage. The partial polarizer's glass plates mount to the tilted faces, secured by four screws with rubber o-rings.

2.4.3 Calibration Polarizer

The most basic and primary function of the PSG-2 is to calibrate highly accurate polarimeters. For the MSPI camera, 100% DoLP light at varied polarization angles provides the calibration standard. To accommodate this, the PSG-2 can produce a fully

polarized field at any polarization orientation by replacing the partial polarizer plates with a broadband UBB01A Moxtek wire grid polarizer.

Wire grid polarizers divide polarization by transmitting one state and reflecting the other. MSPI's focal plane contains wire grid polarizers that reflect light back towards the object. If the PSG-2 reflects this light into its output field of view it will reduce the output DoLP. The calibration polarizer mounts into the partial polarizer sleeve tilted at 10.5˚ to prevent this issue, shown in Figure 2.24.

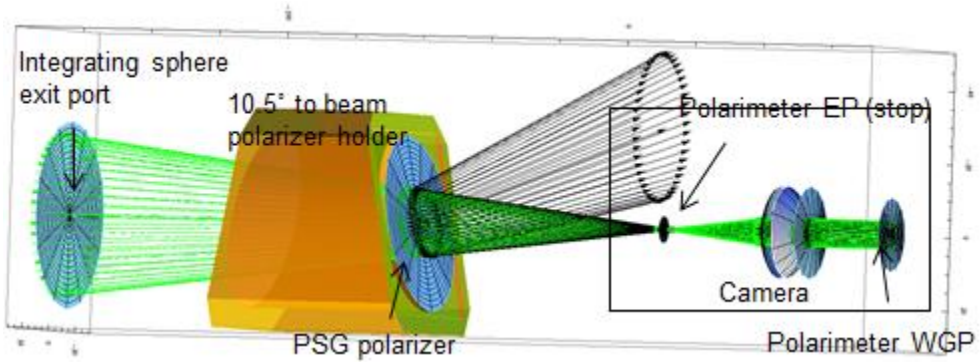

Figure 2.24. Wire grid calibration polarizer mounts at an angle so reflections from MSPI's polarizer do not reflect back into the field of view.

2.4.4 Alignment Concept

2.4.4.1 Field Alignment

Each partial polarizer module pairs with calibration documentation, which consists of 2-D maps of DoLP and AoLP at 36 rotation stage orientations spaced evenly from 0˚ to 350˚. The calibration maps have the same pixels per degree of field as MSPI images to facilitate comparison. Each channel in a MSPI image will correspond to a different line-shaped subregion of the calibration maps, shown in Figure 2.26. To properly implement

the calibration maps with the required accuracy, the MSPI pixel position within the map must be known to within 2 pixels.

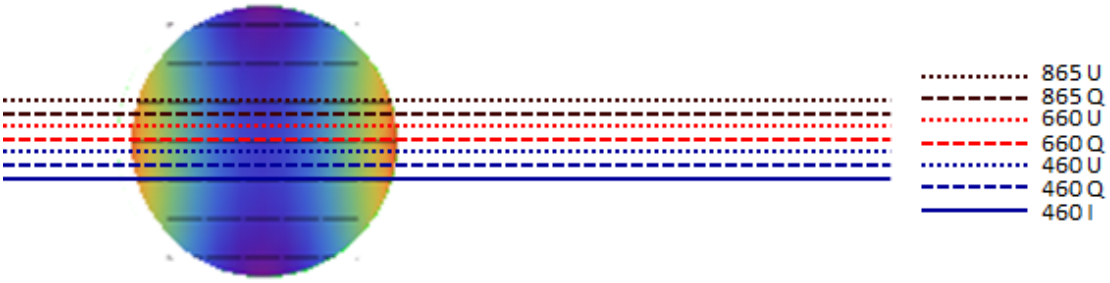

Figure 2.25. MSPI detector samples lines across the calibration maps.

The PSG-1 illumination system created a real, accessible field plane, allowing a field-defining aperture to appear in focus to MSPI. The aperture image can then be used to determine the alignment between PSG-1 and MSPI so the calibration map implementation meets accuracy requirements. Since the PSG-2 does not include any beam shaping optics, no intermediate image plane exists. MSPI images of PSG-2 output contain no in-focus features to establish alignment.

With no way to discern alignment from MSPI images of its output, the PSG-2 includes a simple alignment module to determine the PSG-2/MSPI alignment prior to a measurement. The module consists of a pinhole and a collimating lens that attach to either end of the partial polarizer sleeve. Notches on the pinhole and lens mounts mate with spring plungers at either end of the sleeve to provide repeatable positioning. Cementing the pinhole and lens into their mounts prevents their relative positioning from changing due to frequent handling. Shimming between the rotation stage and the partial polarizer sleeve adjusts the sleeve orientation slightly so that the pinhole and lens define a constant field as the rotations stage moves through 360˚. Figure 2.26 shows the parts of the alignment

module. During MSPI testing, the user mounts the alignment module into PSG-2 illuminating a 2x2 pixel portion of MSPI's field of view and defining the PSG-2's on axis field. The user removes the alignment system and acquires an image. With the center of the calibration map matched to a pixel in one MSPI band, the data from that band compares directly with the center row of the calibration map on a pixel by pixel basis. Each additional MSPI band directly compares to a different row of the calibration map determined by the known focal plane geometry.

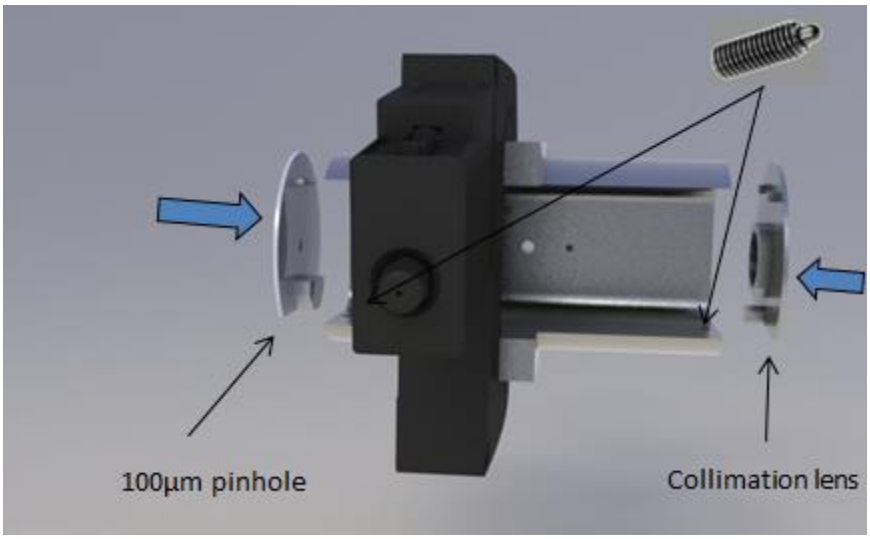

Figure 2.26. PSG-2 field alignment scheme. Spring plunger set screw shown in top right of figure.

2.4.4.2 Spatial Pupil Alignment

With the field alignment system mounted in the PSG-2, the xy- pupil alignment is performed by separately translating the camera in the x and y plane and noting the position where the illuminated pixel becomes fully vignetted. After noting these positions, the

camera moves to the center of translation found from the fully vignetted coordinates. The z- translation is performed by removing the pinhole and collimation lens and placing the integrating sphere into the PSG-2. The separation between the integrating sphere exit port and the camera's entrance pupil is adjusted so that the fully vignette size of the exit port covers 7.71º of pixels.

2.4.5 Illumination

The PSG-2 illumination system specifically targets the requirements for calibrating the AirMSPI camera. The PSG-2 must output radiance greater than 10% of the Earth's upward radiance over the wavelength range of 440 nm to 2200 nm with a field of view of +/-3º. The source DoLP must be less than 0.02%. To meet the AirMSPI calibration requirements, the PSG-2 was designed to include a 150 W solar simulator and an 8" integrating sphere with no addition optical elements.

An SF150-B Sciencetech Inc. solar simulator illuminates a US-800-SF 8" labsphere integrating sphere to provide a light source for the PSG-2. The solar simulator produces 2 SUNs (200 mW/cm^2) over its 25 mm output when equipped with an AM1.5G filter, and the PSG-2 will use the unfiltered output of the solar simulator. The filtered output is referred to in this section because it is a well understood reference standard. The integrating sphere's 50.8 mm output port provides greater than +/-3º field of view for a camera with located 412 mm away.

The output radiance of the integrating sphere is calculated based on the AM1.5G spectrum [54], the spectral reflectance of the Spectraflect used in the integrating sphere,

and published models for integrating sphere exit port radiance. Labsphere gives the exit port radiance of an integrating sphere as [55]:

$$L_s = \frac{\Phi_i}{\pi A_s} * \frac{\rho}{1 - \rho(1 - f)} \tag{2.1}$$

Where A_s is the sphere's surface area, ρ is the surface reflectance, and *f* is the ratio of port area to sphere surface area. Using equation (2.1), a 200 mW/cm^2 AM1.5G spectrum, and the spectral reflectance of Spectraflect, the sphere's output radiance is calculated and compared to typical upwelling radiance, Figure 2.27. The combination of solar simulator and integrating sphere provide the required 10% of typical upwelling radiance over the required spectrum.

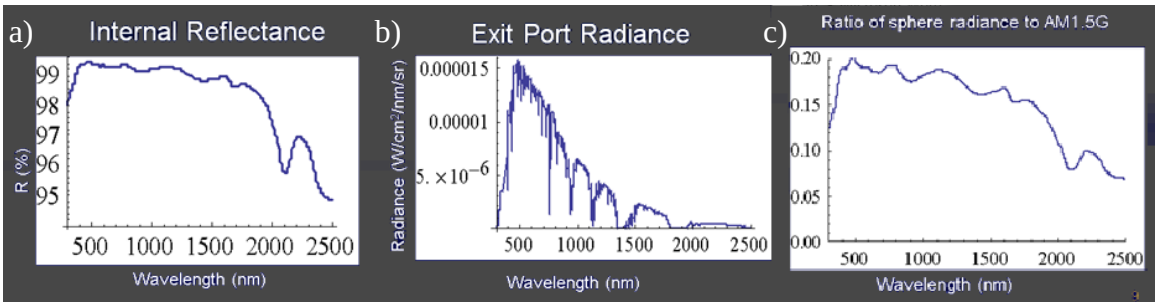

Figure 2.27. a. Spectraflect reflectance. b. Radiance at sphere exit port. c. Ratio of sphere exit port radiance to typical upwelling radiance.

The illumination system must also have an output DoLP of less than 0.02% over its output. Chipman and McClain show Mueller matrix measurements of integrating sphere outputs demonstrating DoP of 0.5% or less [56]. In order to verify that the integrating sphere DoLP output would meet the 0.02% requirement measurements, integrating sphere output measurements were performed using a linear stokes polarimeter. The results showed

that the integrating sphere produced an output with average DoLP of 0.019%, shown in Figure 2.28. This provides a source with substantially better uniformity and polarization properties than the light pipe used in the PSG-1 [57, 58] while also allowing the PSG-2 to forego collection and condensing optics. Using an integrating sphere instead of collection and condensing optical elements was included by Mahler in her discussion of future work [41].

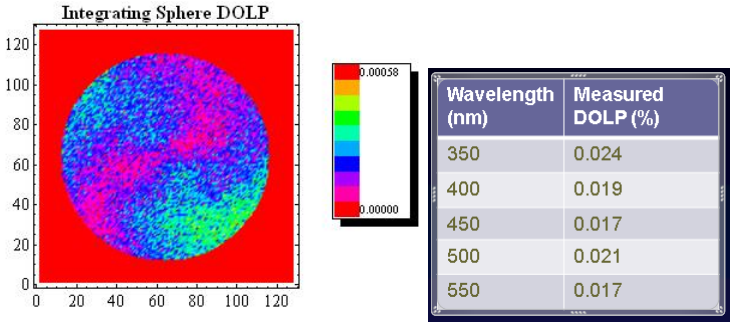

Wavelength (nm)	Measured DOLP (%)
350	0.024
400	0.019
450	0.017
500	0.021
550	0.017

Figure 2.28. UV and visible light DoLP measurements find nearly unpolarized light exiting integrating sphere.

2.4.6 Sub-System Mounting

The previous sections developed the PSG-2 concept into sub-systems designed to meet requirements. Designing fixturing that is compatible with the sub-system and system requirements completes the design. Due to the field of view, the PSG-2/MSPI spacing requirements, and the sizes of the partial polarizer sleeve, integrating sphere, and pinhole mount, the pinhole and integrating sphere cannot be mounting in the system together. This does not prevent the PSG-2 from working as intended; the pinhole should be out of the system during calibration, and testing and removing the integrating sphere during alignment provides better pinhole illumination. It does add another step to calibration and

testing so the mount design facilitates removal and replacement of the sphere. The sphere sits in a cylindrical recess with a bevel tangential to the sphere surface. Additional recesses accommodate the outer features of the sphere. The sphere connects to the bottom of the cylindrical recess with a pair of spring-loaded catches rated for 5 lbs. each. They provide tension to keep the sphere firmly in place, reasonably repeatable repositioning, and a simple mechanism for removing the sphere. The rotation stage, sleeve, and partial polarizers, mount directly after the sphere on the same platform. Figure 2.29 shows the full system.

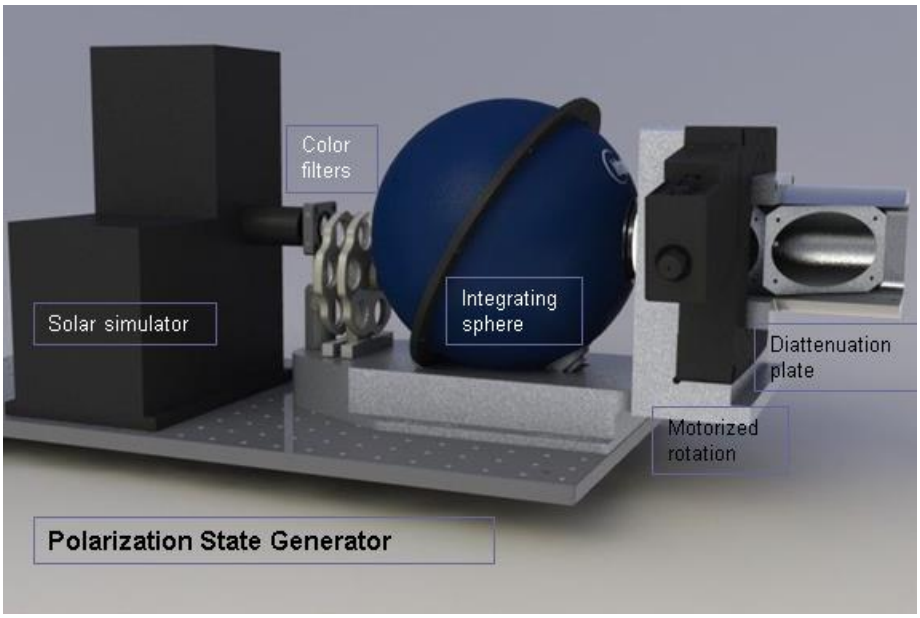

Figure 2.29. Model of entire PSG-2.

2.5 PSG-2 Calibration

The PSG-2 calibration process generates the DoLP and AoLP maps using a combination of theoretical models and measurement results for each partial polarizer. The measurement results establish best fit plate orientations for each partial polarizer by

measuring DoLP from 400 nm to 800 nm. Measurements also confirm that the DoLP pattern rotates around the axis defined by the alignment system as expected. The model, using the best fit plate angles, generates DoLP and AoLP maps for each partial polarizer and partial polarizer orientations from 0˚ to 350˚ in 10˚ steps. This relies heavily on extrapolation to cover AirMSPI's wavelength range. The theoretical DoLP for a single glass plate with infinite ghosting is defined [49, 34].

$$DoLP = \frac{\left| T_s^2\left(1/(1-R_s^2)\right) - T_p^2\left(1/\left(1-R_p^2\right)\right)\right|}{T_s^2\left(1/(1-R_s^2)\right) + T_p^2\left(1/\left(1-R_p^2\right)\right)} \tag{2.2}$$

R and T parameters in the above equation (2.2) are Fresnel coefficients and depend on incident angle and refractive index. The incident angles at the plates remain constant with wavelength and the error in refractive index should remain a small portion of the error budget over the spectrum, so the model for DoLP can safely be extrapolated. Potential extrapolation issues relate to incomplete understanding of scattering from PSG-2's non-optical components.

A Mueller matrix imaging polarimeter was modified to operate as a linear Stokes polarimeter for PSG-2 calibration. A monochromator with 20 nm bandwidth and central wavelength between 400 nm and 800nm illuminates PSG-2's integrating sphere. Following the PSG-2 and prior to any optics, a broadband UBB01A Moxtek polarizer mounted in a motorized rotation stage analyzes the polarization leaving the PSG-2. A 5 mm diameter imaging lens following the polarimeter collects approximately the same ray bundle as MSPI. A 16-bit Hamamatsu camera at the rear focal plane of the lens collects a series of

images at discrete polarizer orientations. The DoLP is calculated by curve fitting to a sinusoid.

2.5.1 Calibration Results

All of the plate sets were measured at 400 nm, 600 nm, 700 nm, and 800 nm. The 700 nm measurements were used to determine the plate angle parameters for the DoLP model that resulted in the best agreement. The same model was used to generate DoLP maps for the other wavelengths. This was intended to demonstrate the validity of the proposed calibration approach. Figure 2.30 shows cross sections of the measured DoLP compared to the modeled DoLP for the 20% DoLP plate pair. Over the +/- 3º field of view plotted, the measured DoLP and modeled DoLP remain within 0.001 for all wavelengths. For 400 nm and 800 nm the DoLP error does not stay within the specification of 0.0002. The best fit plate angles for the 20% DoLP plate pair were found to be 44.07º and 42.87º.

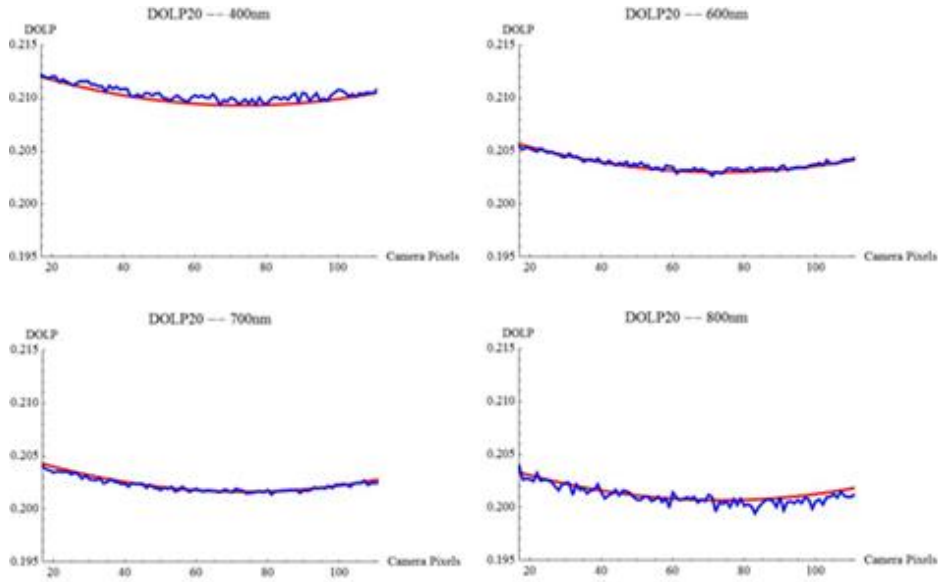

Figure 2.30. 20% DoLP plate pair measurements vs model.

Figure 2.31 through Figure 2.33 show comparisons of measured and modeled data for 10%, 5%, and 1 % DoLP plate pairs. A same approach was used to find the plate angles used in the model. The model plate angles and the design angles for all the plate pairs are shown in Table 2.2. These plate pairs perform similarly to the 20% DoLP pair. The model and measured data usually match to with 0.001 DoLP but not 0.0002.

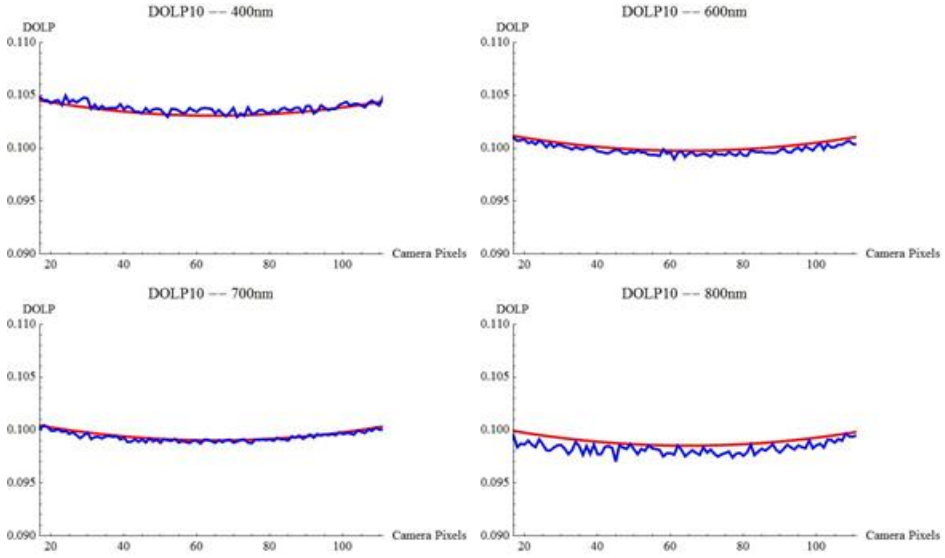

Figure 2.31. 10% DoLP plate pair measurements vs model.

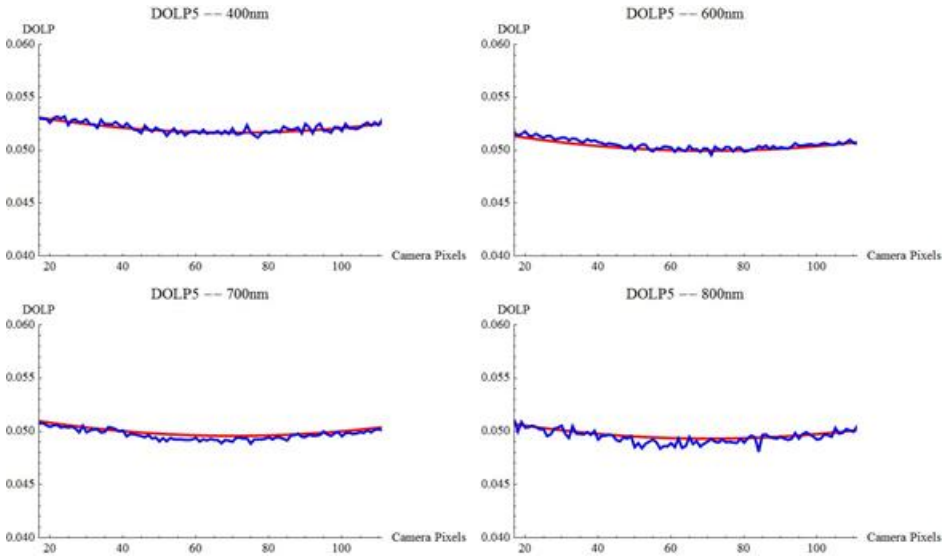

Figure 2.32. 5% DoLP plate pair measurements vs model.

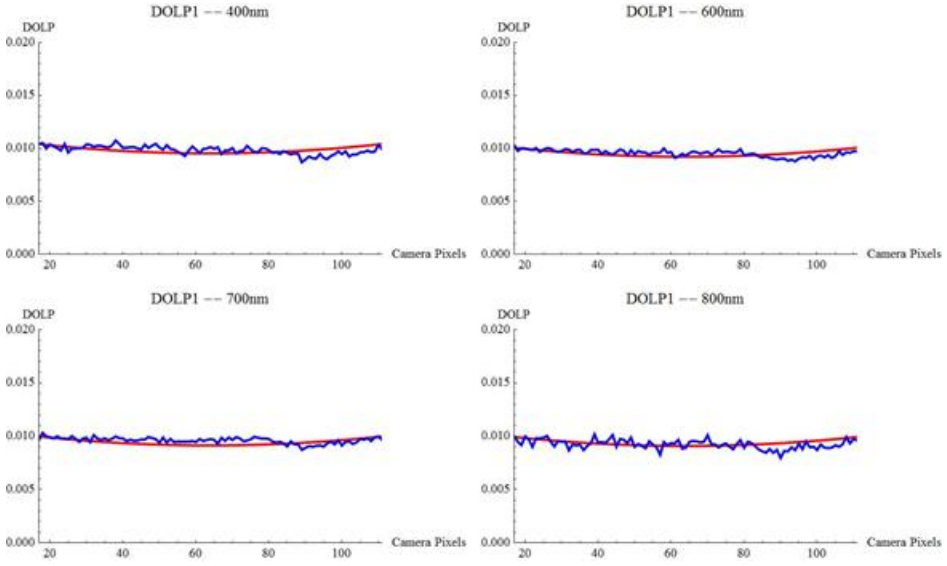

Figure 2.33. 1% DoLP plate pair measurements vs model.

The calibration of the PSG-2 used a camera instead of a single channel detector to simplify and increase the resolution of the field sampling. The source for calibration was the polarimeter's monochromator coupled into the PSG-2's integrating sphere. This resulted in low light levels that required long exposure times. Much of the discrepancy

between measured and modeled data appears to be readout noise since there is no reason to expect high frequency spatial variations in DoLP. If it is assumed that all of the high spatial frequency variations are readout noise centered on the actual DoLP, the results are very close to the 0.0002 DoLP requirement and most wavelengths and plate pairs.

Partial Polarizer	Plate angle 1	Plate angle 2	Design angle
40%	58.00	58.00	58.00
20%	44.07	42.87	43.00
10%	31.78	31.68	31.75
5%	23.40	22.60	23.00
1%	10.10	10.10	10.50

Table 2.2. Shows the measured plate angles compared to the designed plate angles.

Figure 2.34 compares the measured and model DoLP for the 40% plate pair. It shows similar performance to the other plate pairs at 400 nm and 600 nm but begins to show significant error at 700 nm and performs terribly at 800 nm with about a 3% DoLP error. This is the result of a serious design flaw in the 40% DoLP plate that was not considered until the issue was found during calibration. Figure 2.35 shows rays traced from the MSPI entrance pupil towards the PSG-2. A small patch of the inside wall of the plate holder is in the PSG-2's active field of illumination. For the 40% plate, this patch also happens to be positioned such that in can be directly illuminated by the integrating sphere. The black anodized surface absorbs most of the light at 400 nm and 600 nm but apparently is not as black at longer wavelengths.

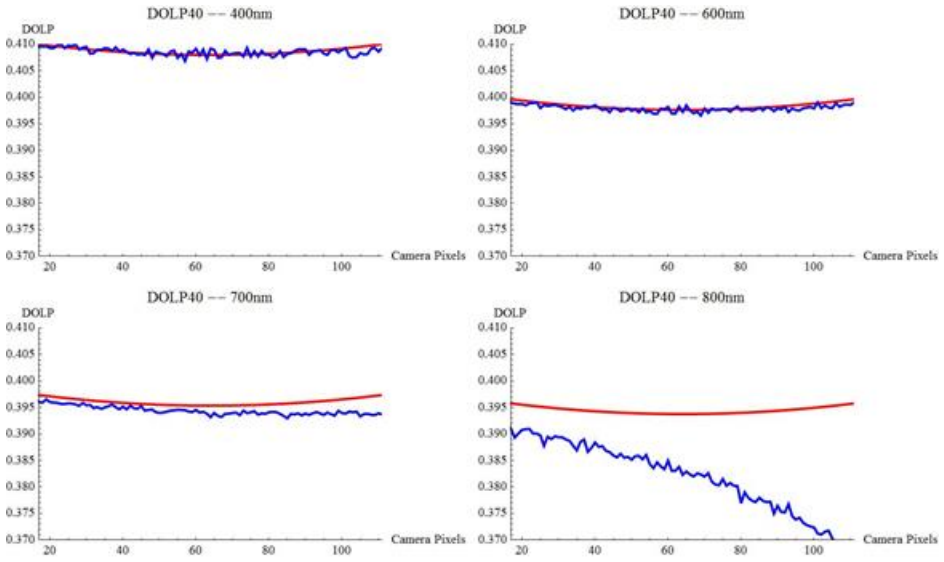

Figure 2.34. 40% DoLP plate pair vs measurement.

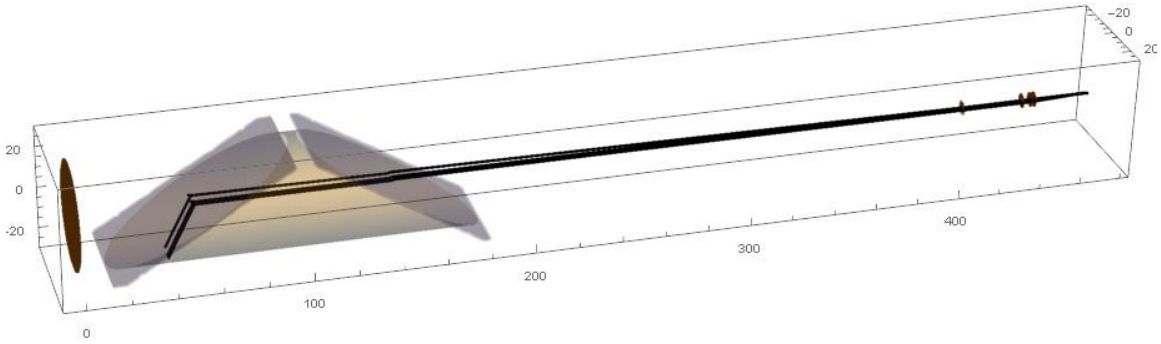

Figure 2.35. Stray light path from inside wall of plate holder MSPI entrance pupil. The patch on the plate holder wall visible to the MSPI pupil is directly illuminated by the integrating sphere for the 40% DoLP plate pair.

2.5.2 Rotational Repeatability

The ability to produce polarized and partial polarization states at any orientation provides the PSG-2 with a powerful calibration and testing tool. The accuracy of polarimetric devices cannot be assumed to constant with incident polarization orientation so the ability to analyze the accuracy over different incident orientation provides a powerful

testing tool. PSG-2 calibration cannot be performed at evey possible partial polarization orientation. Instead, DoLP maps created from calibration results at one polarization orientation will be rotated in software to compare to MSPI test data collected with different partial polarizer rotation. The DoLP maps are centered on the field defined by the alignment system, which is along the rotation axis. Rotating the DoLP maps in software should provide an accurate model for what MSPI sees as the partial polarizers physically rotate.

In order to test whether the DoLP will be accurate independent of polarization orientation we perform measurements on the 20% partial polarizer at a number of different orientations. Software is used to rotate each measurement around the pixel designated as the 0º field by the alignment system by an amount equal and opposite the set polarization orientation. If the PSG-2 is insensitive to rotation, as it is designed to be, each of the rotated plots should be approximately equal.

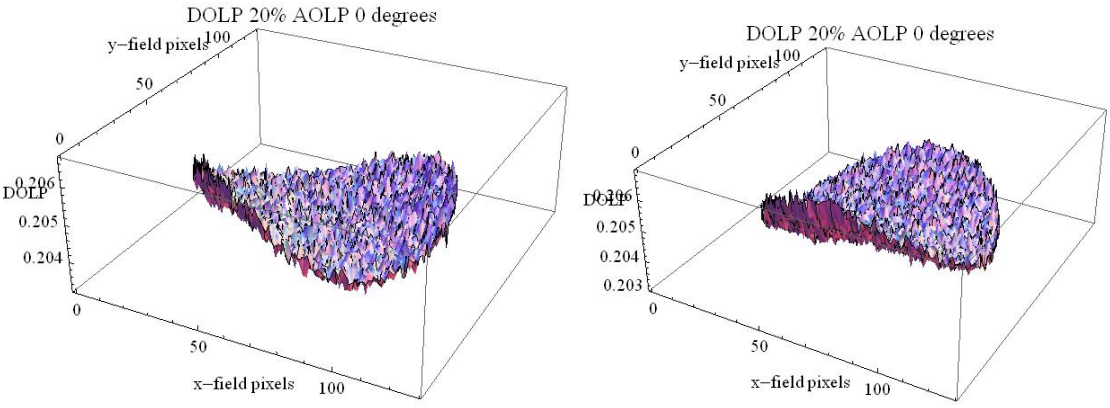

Figure 2.36. Shows 20% partial polarizer measured at 0º and 45º. The plots both show the asymmetry of the DoLP field dependence.

Figure 2.36 shows measurements taken with a 45º difference in polarization orientation. It is clear that both measurements demonstrate asymmetry in DoLP. For these measurements the alignment system was set so that the 0º field corresponded to the central pixel on the CCD. The 45º measurement was rotated by -45º around this pixel and then compared to the 0º measurement.

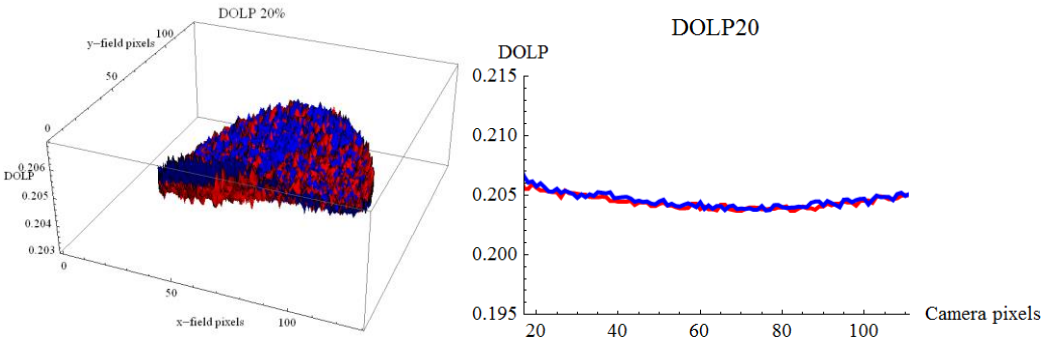

Figure 2.37. When the measurements are rotated to the same orientation in software they show good agreement.

2.6 AirMSPI Calibration

On completion of calibration the PSG-2 was delivered to JPL. The PSG-2 successfully fulfills its purpose of providing the lab-based polarization calibration and verification platform for AirMSPI. Figure 2.38 shows the results of partial polarization calibration validation testing. The DoLP uncertainty is well within the polarimeter's objective range of 0.005 [59].

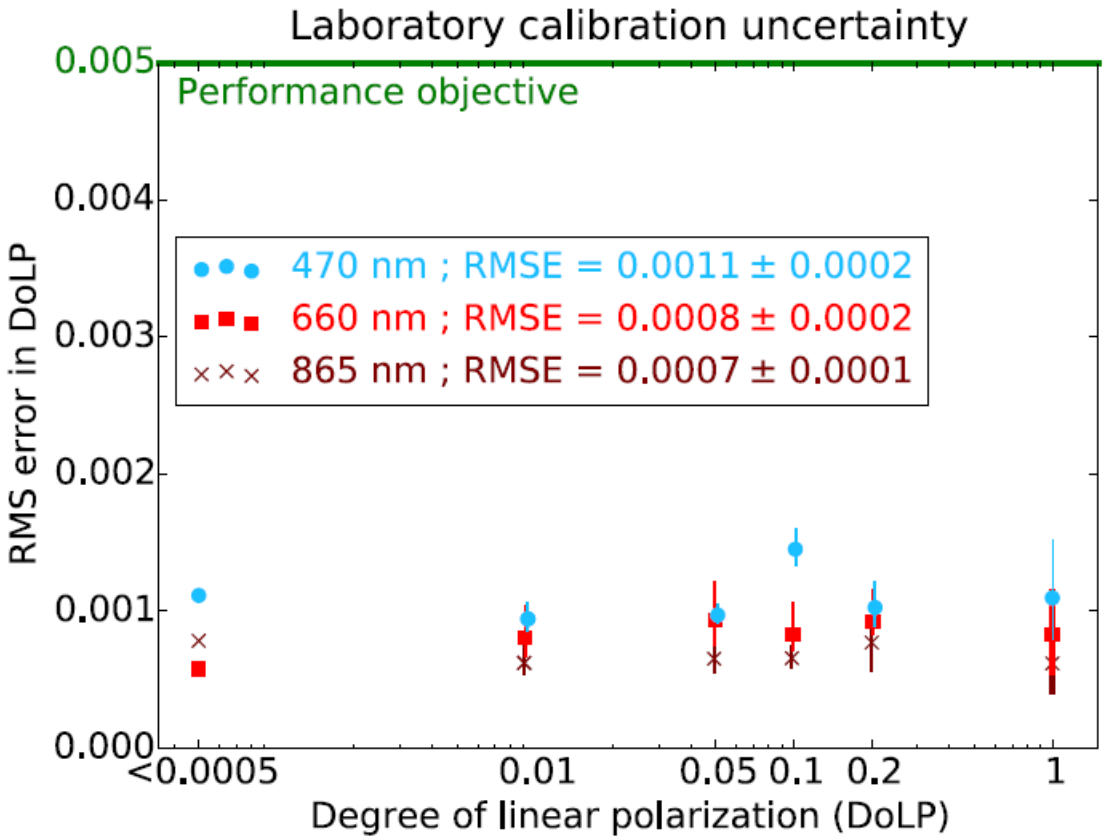

Figure 2.38. Partial polarizer test performed on AirMSPI using the PSG-2 following calibration using the PSG-2. The results are well within the 0.005 RMS DoLP objective [59].

CHAPTER 3

ANALYSIS AND IMPROVEMENT OF EXISTING DESIGN TO MEET POLARIZATION-BASED SPECIFICATIONS

3.1 Introduction

This chapter discusses modeling and optimization of a lens and coating design that was close to missing its polarization specification. Design requirements and the initial analysis identifying the potential issue was enough to identify the likely primary source of error, which was confirmed by raytracing the system using Polaris-M. Determining and understanding the source of the error allowed for a simple solution that significantly improved the error budget for the polarization-based requirement but this solution also would drive other requirements out of spec and was only presented to demonstrate that the polarization-based performance could be improved and provide a basic approach for doing so.

Optimization successfully improved the polarization-based performance without degrading other design requirements. The optimized design raised concerns about manufacturability, due to the use of thin-film layers less than 10 nm, and was modified. Monte-Carlo analysis, along with other specifically requested analysis, was performed to compare the sensitivities of the optimized and original design.

3.1.1 System Description

Details of the optical system and application are confidential so lens and coating prescriptions will not be included and the design requirements will be treated in a manner that does not divulge the application.

The optical system consists of a 12-element objective with an 18 mm entrance pupil and a 12.8 mm focal length. The objective is illuminated with a 2 mm beam of circularly polarized light originating from on axis in the front focal plane. The beam can be pointed towards any point in entrance pupil with accuracy of 3.1 μm. The system operates over the wavelength range of 500 nm to 900 nm. AR coatings applied to each air/glass interface increase transmission and reduce polarization aberrations.

3.1.2 Issue

The system has a design requirement labeled "X/Y separation" defining how accurately the relative intensity of the x and y polarization components are known for any beam aiming configuration. The X/Y separation requirement is defined as,

$$\left|\frac{I_x(r,\lambda) - I_y(r,\lambda)}{I_x(r,\lambda) + I_y(r,\lambda)} + C(r_0,\lambda)\right| \leq 4 \times 10^{-4} \tag{3.1}$$

I_x and I_y are the intensities of the x and y polarization component leaving the objective and C is a calibration term to account for polarization aberrations of the objective; both are dependent on wavelength, λ, and either actual pupil position, r, or expected pupil position, r_0. The calibration will create a table of C values by polarization ray tracing. For the following analysis it is assumed that when $r = r_0$ the X/Y separation error is 0.

Analysis of the initial design found that it was nearly out of spec at 500 nm. This analysis did not account for manufacturing errors so as built errors are likely higher than the simulated results. The 4 x 10^{-4} error budget includes small contributions from other components that are not discussed here. Based in these results, it was determined that the current design had a large risk associated with the X/Y separation accuracy.

3.2 Initial Assessment

Before performing additional modeling and optimization, analyzing and understanding the system and data will help frame the approach moving forwards. A simulation of the objective's X/Y separation at 600 nm is shown in Figure 3.1. Where the X/Y separation error is estimated by calculating local slopes over 2 mm circular sub-apertures and multiplying by the beam aiming uncertainty 3.1 μm. In total the available information amounts to the following: an optical design, description of operation, AR coating prescriptions, and simulated data demonstrating the issue. Clarifying the mode by which AR coating properties affect X/Y separation error is a good place to begin the initial assessment.

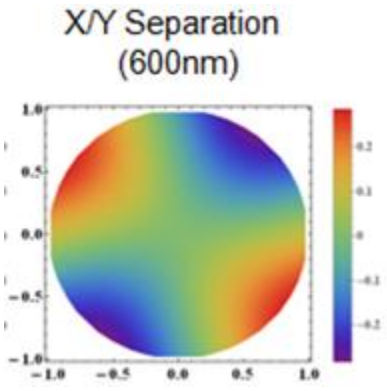

Figure 3.1. Simulated X/Y separation pupil map.

3.2.1 Possible Objective Polarization Aberrations

The objective illumination system consists of a small source located at the objective's focal plane that can be aimed to illuminate any 2 mm sub-region of an on axis collimated beam. The source size is on the order of microns so the field of view of the source is approximately 0. The objective is rotationally symmetric with spherical surfaces. To first order, the incident angle map for each surface will be centered on axis and have a magnitude increasing linearly with radius. This type of incident angle map leads to defocus type polarization aberrations for each surface. Figure 3.2 shows this type of incident angle map and resulting polarization aberration possibilities. Cascading multiple weakly polarizing surfaces with defocus type polarization aberrations will result in a pupil with approximately defocus type polarization aberrations. Each surface in the system will have retardance approximated by, $\delta_i\theta^2$, and a diattenuation approximated by, $\mathcal{D}_i\theta^2$. The orientations of polarization aberrations at each surface for a given ray will always be parallel or perpendicular to the previous surface. If each surface interaction is weakly polarizing, this means the total diattenuation or retardance can be approximated by adding the parallel components and subtracting the orthogonal components at each surface [60, 34, 61, 62]. For more complex optical systems where paraxial polarization aberration approximation do not hold the method described in [34, 63].

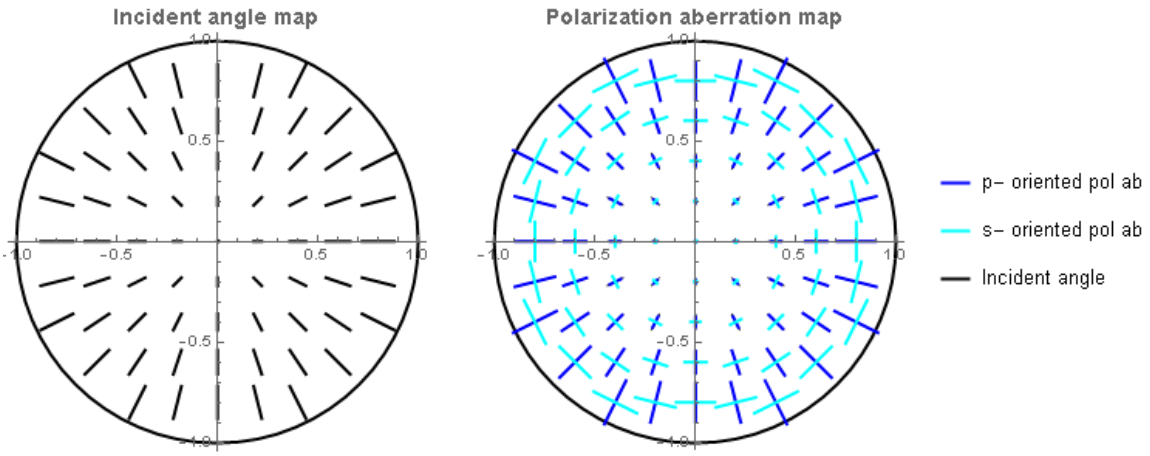

Figure 3.2. For the objective's illumination configuration, incident angle will be linear with radius and polarization aberrations will be quadratic. The geometry is such that s- and p- local coordinates will always be tangential and radial

3.2.2 Sources of X/Y Separation

After determining what type of polarization aberrations are expected, the next step is determining how they will affect the metric of interest, X/Y separation. A visual representation of X/Y separation is shown in Figure 3.3 using a Poincare sphere. X/Y separation is 0 for polarization states on the great circle containing right circular and 45° linear polarizations, and it increases or decreases linearly with position along the 0°/90° axis. This result is trivial given X/Y separation is, by definition, equal to s_1/s_0, but the visual is still useful when relating X/Y separation to polarization aberrations.

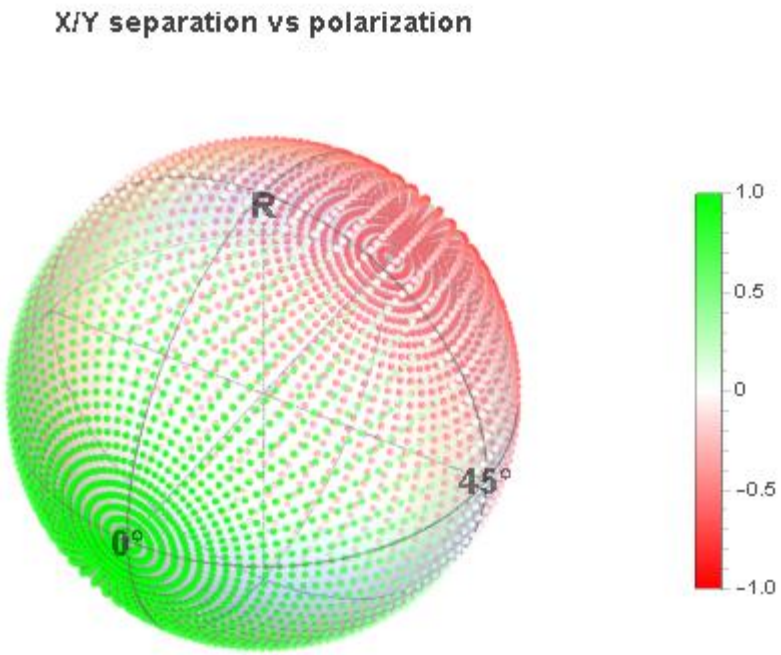

Figure 3.3. X/Y separation vs polarization plotted on Poincare sphere

A similar visual tool can be created to show the role of polarization aberrations. The polarization states resulting from circularly polarized light passing through a linear retarder or linear diattenuator at various orientation angles are plotted on a Poincare sphere, Figure 3.4. A linear retarder with an orientation of 135° or 45° will cause the polarization state to move in the direction of increasing or decreasing X/Y separation. When the orientation is 0° or 90° the polarization state changes but the value of X/Y separation does not. For a linear diattenuator orientations of 0° or 90° change X/Y separation and 45° and 135° cause no change.

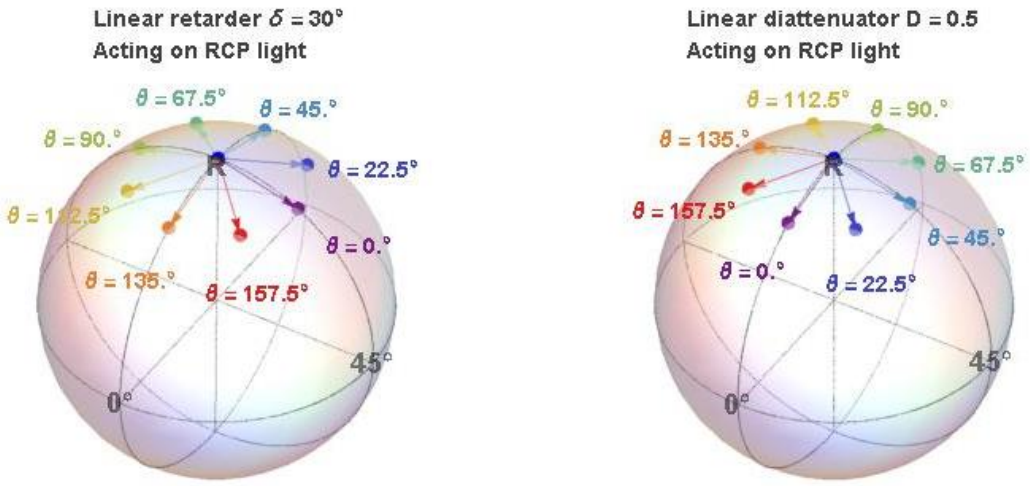

Figure 3.4. Effects of linear retarders (left) and diattenuators (right) on circularly polarized light

The provided X/Y separation map, Figure 3.1, has minima and maxima along the 45° and 135° directions. Since the objective's polarization aberrations must be either radial or tangential, the orientation of the polarization aberration causing this X/Y separation has an orientation of either 45° or 135°. Since, out of retardance and diattenuation, only retardance causes X/Y separation when oriented at 45° or 135°, it must be the primary source of X/Y separation in the current objective design.

3.2.3 Analytical Description of X/Y Separation Uncertainty

Since retardance appears to be the dominant polarization aberration, at least at 600 nm, this section will begin by examining the relationship between X/Y separation uncertainty and coating induced retardance. Figure 3.4 (left) shows how a linear retarder with an orientation of 45° or 135° will induce X/Y separation while an orientation of 0° or 90° will not. This was helpful in quickly identifying the dominant polarization aberration

but is not particularly useful in determining X/Y separation uncertainty given a pupil coordinate uncertainty of 3.1 μm. In Figure 3.4 (left) the orange line reflects the change in polarization for circularly polarized light incident on a linear retarder at 135° and clearly changing the magnitude of retardance would change the X/Y separation. This is the mechanism by which radial displacements in the pupil cause X/Y separation uncertainty. The purple line represents a linear retarder at 0°; it will have no X/Y separation regardless of retardance magnitude. However, as the retardance increases and the arrow lengthens, a change in retarder orientation will have an increasingly large effect on the X/Y separation. This provides the mechanism for tangential pupil displacement to affect X/Y separation uncertainty.

The X/Y separation uncertainty is derived below. Mueller calculus is used due to the convenient fact that, $s_1/s_0 \equiv$ X/Y separation. Equation (3.2) is just the Mueller matrix of a linear retarder with retardance δ and orientation θ and its first order approximation when δ is small. This Mueller matrix multiplied by the stokes vector for right hand circularly polarized light represents the light exiting the retarder and its component s_1 is defined as X/Y separation.

$$\mathrm{LR}(\delta,\ \theta) = \begin{pmatrix} 1 & 0 & 0 & 0 \\ 0 & \cos^2(2\,\theta) + \cos(\delta)\,\sin^2(2\,\theta) & \sin^2\left(\frac{\delta}{2}\right)\sin(4\,\theta) & -\sin(\delta)\,\sin(2\,\theta) \\ 0 & \sin^2\left(\frac{\delta}{2}\right)\sin(4\,\theta) & \cos(\delta)\,\cos^2(2\,\theta) + \sin^2(2\,\theta) & \cos(2\,\theta)\,\sin(\delta) \\ 0 & \sin(\delta)\,\sin(2\,\theta) & -\cos(2\,\theta)\,\sin(\delta) & \cos(\delta) \end{pmatrix} \quad \textbf{(3.2)}$$

$$\approx \begin{pmatrix} 1 & 0 & 0 & 0 \\ 0 & 1 & 0 & -\delta\,\sin(2\,\theta) \\ 0 & 0 & 1 & \delta\,\cos(2\,\theta) \\ 0 & \delta\,\sin(2\,\theta) & -\delta\,\cos(2\,\theta) & 1 \end{pmatrix} \text{ for small } \delta$$

$$LR(\delta,\ \theta).S_{rcp} \approx \begin{pmatrix} 1 & 0 & 0 & 0 \\ 0 & 1 & 0 & -\delta \sin(2\,\theta) \\ 0 & 0 & 1 & \delta \cos(2\,\theta) \\ 0 & \delta \sin(2\,\theta) & -\delta \cos(2\,\theta) & 1 \end{pmatrix} \cdot \begin{pmatrix} 1 \\ 0 \\ 0 \\ 1 \end{pmatrix} = \begin{pmatrix} 1 \\ -\delta \sin(2\,\theta) \\ \delta \cos(2\,\theta) \\ 1 \end{pmatrix} \tag{3.3}$$

X/Y separation is now written in terms of retardance and retardance orientation. With only defocus type polarization aberrations, it is simple to rewrite the retarder parameters as functions of pupil position. The only change needed is to substitute ($\delta_0\ r^2$) for δ, where r is the normalized pupil radius and δ_0 is the retardance for the marginal ray through the edge of the pupil. The partial derivatives of X/Y separation are computed.

$$X/Y_{sep} = S_1/S_0 \approx -\delta \sin(2\,\theta)\,|_{\delta = \delta_0\ r^2} \approx \delta_0\ (-r^2)\ \sin(2\,\theta) \tag{3.4}$$

$$\frac{\partial X/Y_{sep}}{\partial r} \approx -2\ \delta_0\ r \sin(2\,\theta) \tag{3.5}$$

$$\frac{\partial X/Y_{sep}}{\partial \theta} \approx -2\ \delta_0\ r^2 \cos(2\,\theta) \tag{3.6}$$

The units of $\frac{\partial X/Y_{sep}}{\partial \theta}$ are not consistent with $\frac{\partial X/Y_{sep}}{\partial r}$ or pupil coordinate uncertainty Δr. To correct the units a local Cartesian coordinate system is defined for every pupil

position (r, θ) as shown in Figure 3.5. Since the pupil position uncertainty is small, there is no problem using the first order approximation $\Delta\theta\, r = \Delta t$.

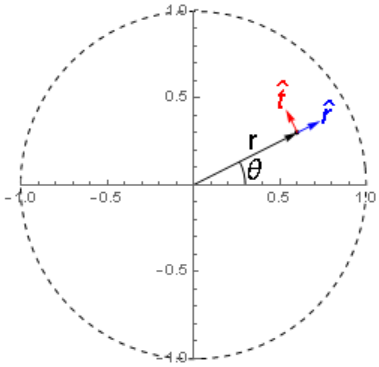

Figure 3.5. Local coordinates associated with pupil coordinate defined by (r, θ)

$$\partial\theta \approx \frac{\partial t}{r} \quad \text{for } r \gg \partial t \tag{3.7}$$

$$\frac{\partial X/Y_{sep}}{\partial t} \approx -2\,\delta_0\, r \cos(2\,\theta) \tag{3.8}$$

$$\vec{\nabla} X/Y_{sep} \approx -2\,\delta_0\, r \sin(2\,\theta)\,\hat{r} - 2\,\delta_0\, r \cos(2\,\theta)\,\hat{t} \tag{3.9}$$

$$\left\| \vec{\nabla} X/Y_{sep} \right\| \approx 2\,\delta_0\, r \tag{3.10}$$

Once the units are consistent the gradient of X/Y separation is calculated and plotted in Figure 3.6. The orientation of the X/Y separation slope changes around the pupil as the polarization aberration orientation changes. However, the magnitude of the slope is independent of θ and depends linearly on r. This slope will provide an estimate for X/Y separation uncertainty but will differ slightly from the local slopes found by least squares fitting planes to sub-regions of the X/Y separation map.

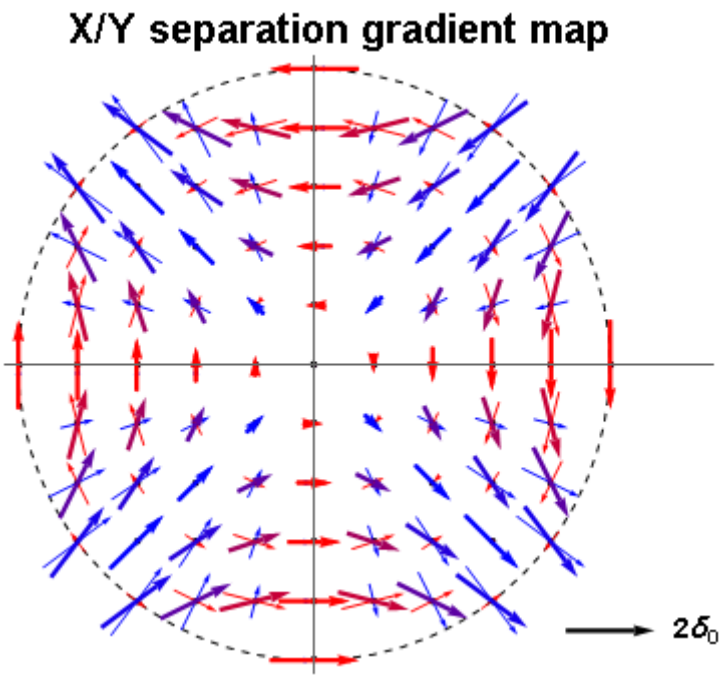

Figure 3.6. X/Y separation gradient map for system dominated by retardance. The radial and tangential components are shown in blue and red. The color of the gradient vector is weighted by the components.

Repeating the derivation starting with the Mueller matrix for a diattenuator instead of a retarder results in the diattenuation induced X/Y separation gradient map. The diattenuation induced gradient map is orthogonal to the retardance induced map. The magnitude of the gradient for a system with both diattenuation and retardance is simply the root sum squared combination of diattenuation and retardance. This suggests that a design intended to reduce the overall local slopes should aim for a balance of diattenuation and retardance rather than reducing one at the expense of the other.

$$\left\|\vec{\nabla} X/Y_{sep}\right\| \approx 2\ r\ \sqrt{\left(d_0^2 + \delta_0^2\right)} \tag{3.11}$$

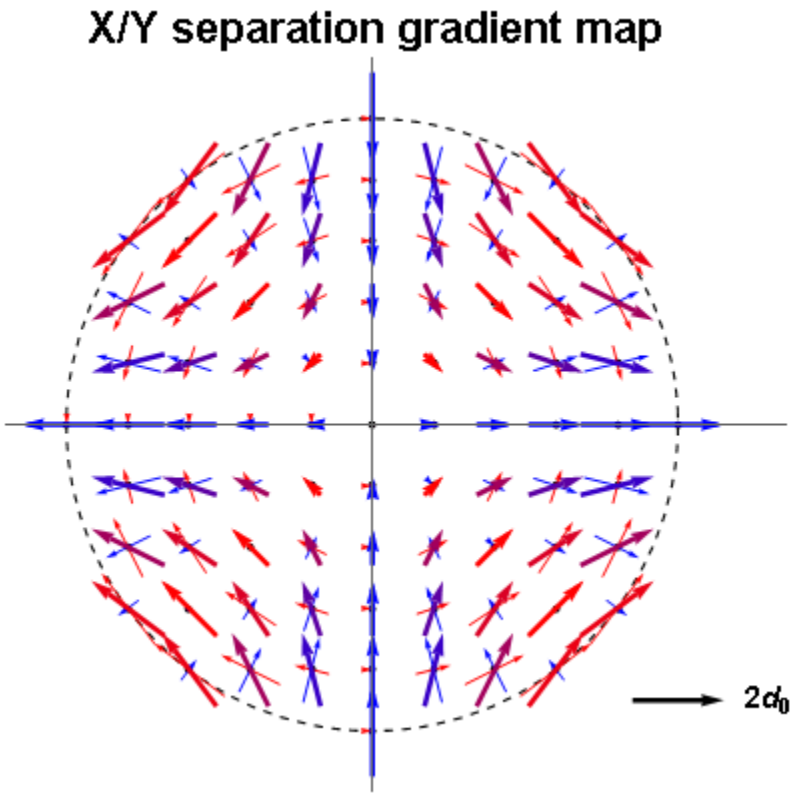

Figure 3.7 X/Y separation gradient map for system dominated by diattenuation. The radial and tangential components are shown in blue and red. The color of the gradient vector is weighted by the components.

3.2.4 Summary

By using information about the optical system and application the pupil dependence of the polarization aberrations was determined to be of the defocus type. Based on the polarization aberration type, the initial simulations, and the relationship between the metric and polarization aberrations, the dominant source of X/Y separation error at 600 nm is shown to be retardance. An approximation for determining X/Y separation uncertainty requiring only the diattenuation and retardance at the edge of the pupil was derived. This

approximation emphasized the importance of avoiding designing for one polarization aberration, retardance or diattenuation, at the expense of the other.

3.3 Reducing Polarization Aberrations with Anti-Reflection Coatings

Uncoated optical systems have relatively large polarization aberration due entirely to the diattenuation from Fresnel equations. Uncoated refractive systems also have about 4% of reflection loss per air/glass interface which is a larger problem than the polarization aberrations. Thin-film coatings can improve both transmission and polarization properties but their design tends to focus only on transmission as a metric. This approach is great for improving the diattenuation since a perfect anti-reflection coating cannot have s- and p-coefficient differences if both are equal. However, increasing the complexity of the coating can increase the retardance experienced by the transmitted wave particularly away from the center design wavelength [64]. How each of reflectance, diattenuation, and retardance will impact system performance is useful to uinderstand.

Figure 3.8 shows the diattenuation and retardance arising from transmission through an air/glass interface for various coatings. In the uncoated case, retardance is 0 for all angles and diattenuation increases quadratically with angle. When a simple ¼ wave AR coating is applied the diattenuation decreases substantially but retardance is no longer 0 but is still very small. Applying a more complex 7-layer coating reduces the diattenuation even more but adds substantial retardance.

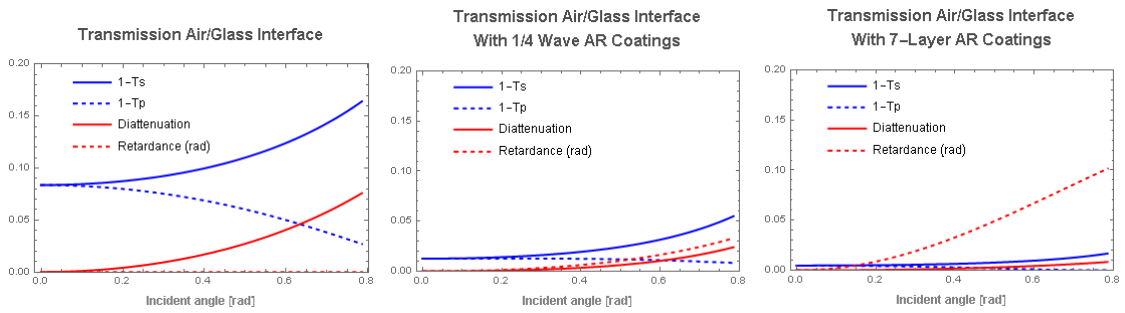

Figure 3.8. The s- and p- reflectance and the transmitted diattenuation and retardance are plotted for an air/glass interface (left), a ¼ wave AR coating on an air/glass interface (center), and a 7-layer AR coating (right).

Consider the simple optical system in Figure 3.9. Assume it's in a polarization sensitive system and it needs to minimize the cross polarized leakage between to cross linear polarizers. The properties are investigated by ray tracing for the three coating cases shown in Figure 3.8. The coating is applied to all four air/glass interfaces for each simulation. Results are shown in Figure 3.10, Figure 3.11, and Figure 3.12.

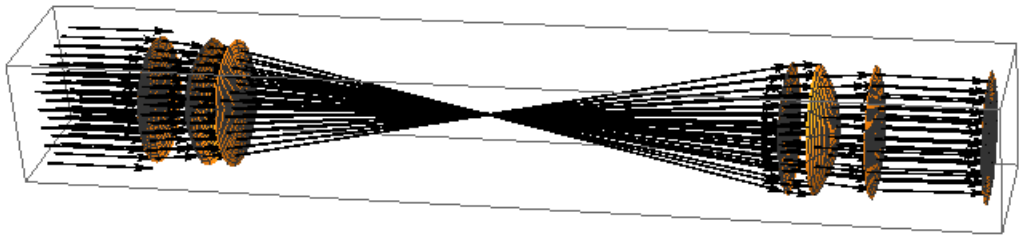

Figure 3.9. Optical system used to demo coating effects on cross polarized leakage.

For the uncoated case the leakage has the familiar Maltese cross pattern with about 3% diattenuation off axis. The lens system with ¼ wave AR coatings on 4 surfaces has reduced the leakage by two orders of magnitude and diattenuation remains the dominant polarization effect. The 7-layer system has virtually no diattenuation but the retardance increased to a peak value of about 0.1 radians and the leakage is an order of magnitude

larger than the uncoated system. In general AR coatings will improve the polarization aberrations of an optical system, but in some instances they can cause additional problems [65, 66]

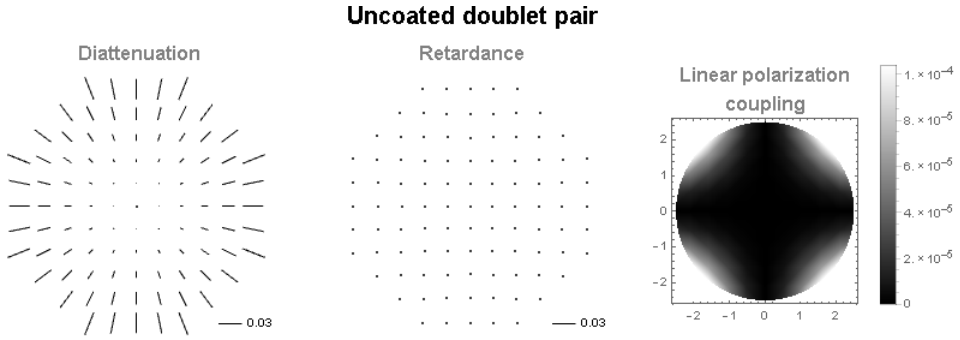

Figure 3.10. Leakage for uncoated case.

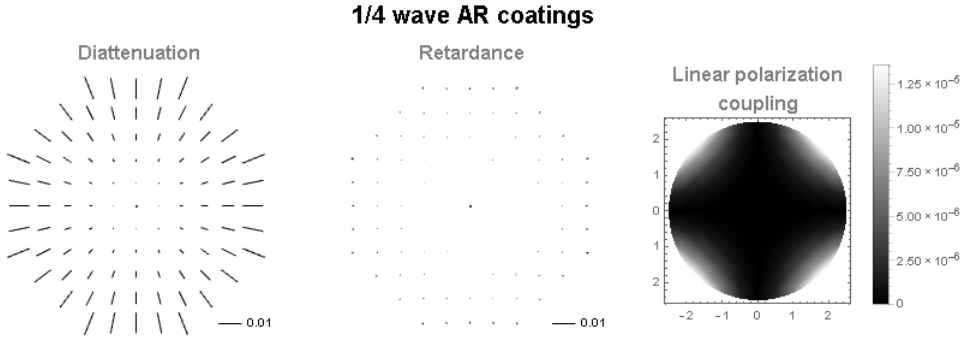

Figure 3.11. Leakage for ¼ case.

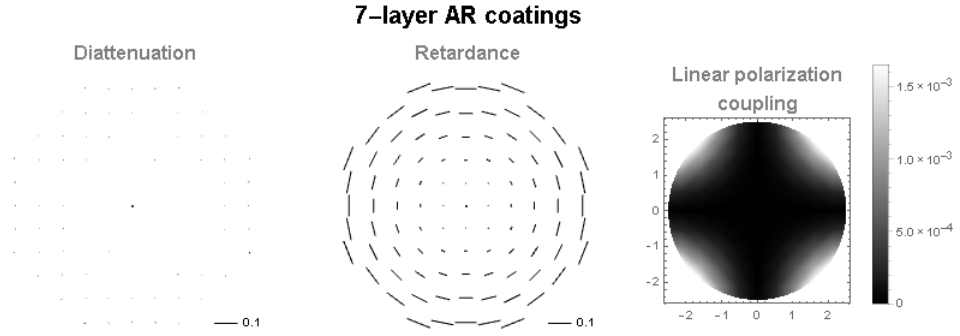

Figure 3.12. Leakage for 7-layer case.

3.4 Initial Modeling and Ray Tracing

The provided Code V files were used to create a Polaris-M model of the objective, including the AR coatings, shown in Figure 3.13. Performing polarization ray tracing in Polaris-M from 500 nm to 900 nm provided the data necessary to confirm initial conclusions and determine if they remained valid across the spectrum. Reduced results are shown in Figure 3.14.

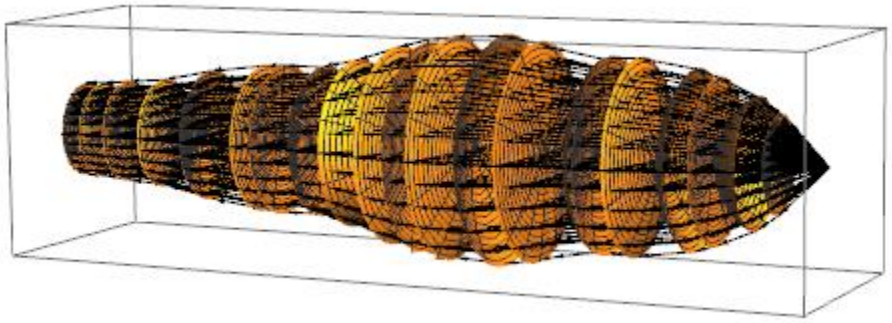

Figure 3.13. Polaris-M model of objective lens.

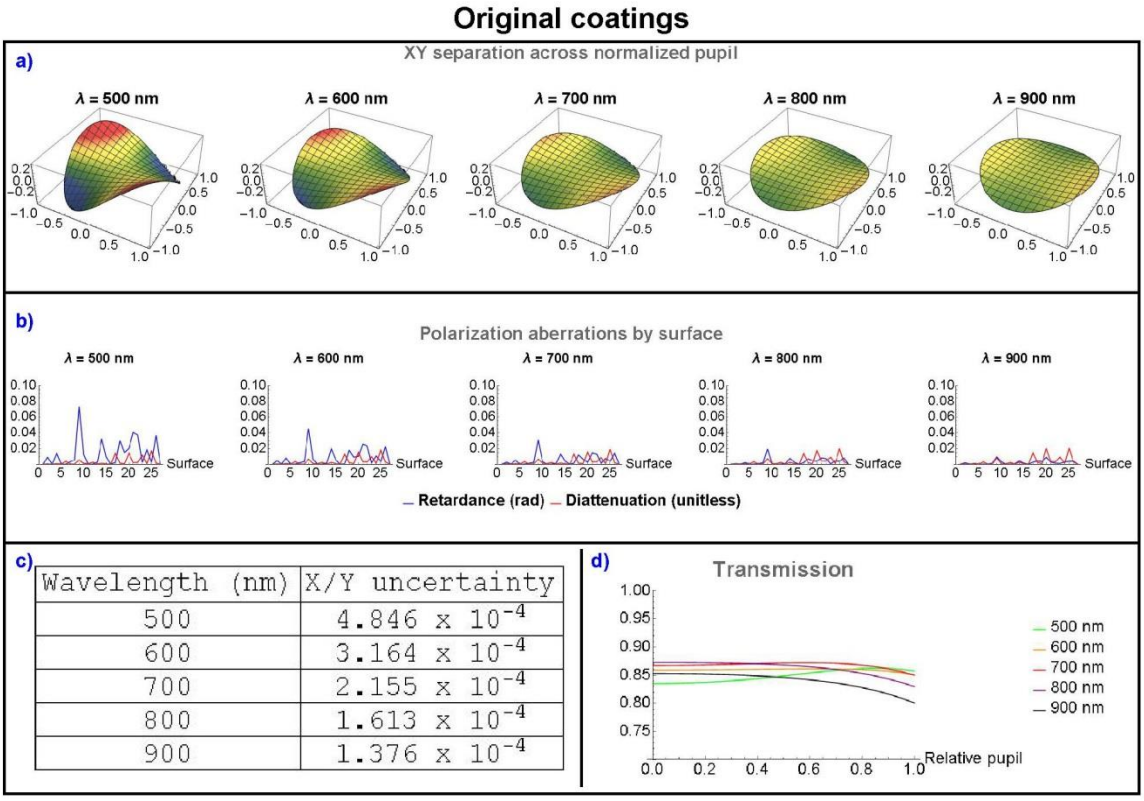

Wavelength (nm)	X/Y uncertainty
500	4.846×10^{-4}
600	3.164×10^{-4}
700	2.155×10^{-4}
800	1.613×10^{-4}
900	1.376×10^{-4}

Figure 3.14. a. X/Y separation pupil maps b. Surface by surface polarization aberrations for marginal rays c. Maximum X/Y uncertainty d. Objective transmission vs relative pupil coordinate

The X/Y separation pupil maps in Figure 3.14 a. show 45°/135° minima and maxima orientation similar to the provided pupil map for 500 nm and 600 nm. Figure 3.14 b. shows the maximum diattenuation (red) and retardance (blue) value associated with each surface of the objective. For 500 nm and 600 nm the retardance is much larger than the diattenuation as predicted. The 800 nm and 900 nm pupil maps have minima/maxima oriented more along the x/y axes and the corresponding polarization aberration plots show diattenuation is dominant. At 700 nm the orientation is somewhere between 45°/135° and x/y, and the polarization aberration plot shows similar amounts of diattenuation and

retardance. Figure 3.14 c. lists the estimated X/Y uncertainty which needs to be reduced and Figure 3.14 d. shows the objective's transmission which must be maintained.

The results expand on conclusions made from the provided data and confirm that retardance is the primary source of X/Y separation error in the system. The surface by surface polarization aberration plots add the most useful bit of information, most of the retardance comes from few surfaces. The three surfaces contributing the largest retardance are 9, 21, and 22.

3.5 Improve X/Y Separation with no Additional Design

With three surfaces contributing most of the retardance it is clear that any attempt to improve the X/Y separation should start by reducing the retardance of surfaces 9, 21, and 22. The retardance can be reduced to 0 without doing any coating design by simply removing the coatings altogether. This will cause both the diattenuation and the reflection to increase, but since only 3 surfaces will be affected maybe these effects will be manageable.

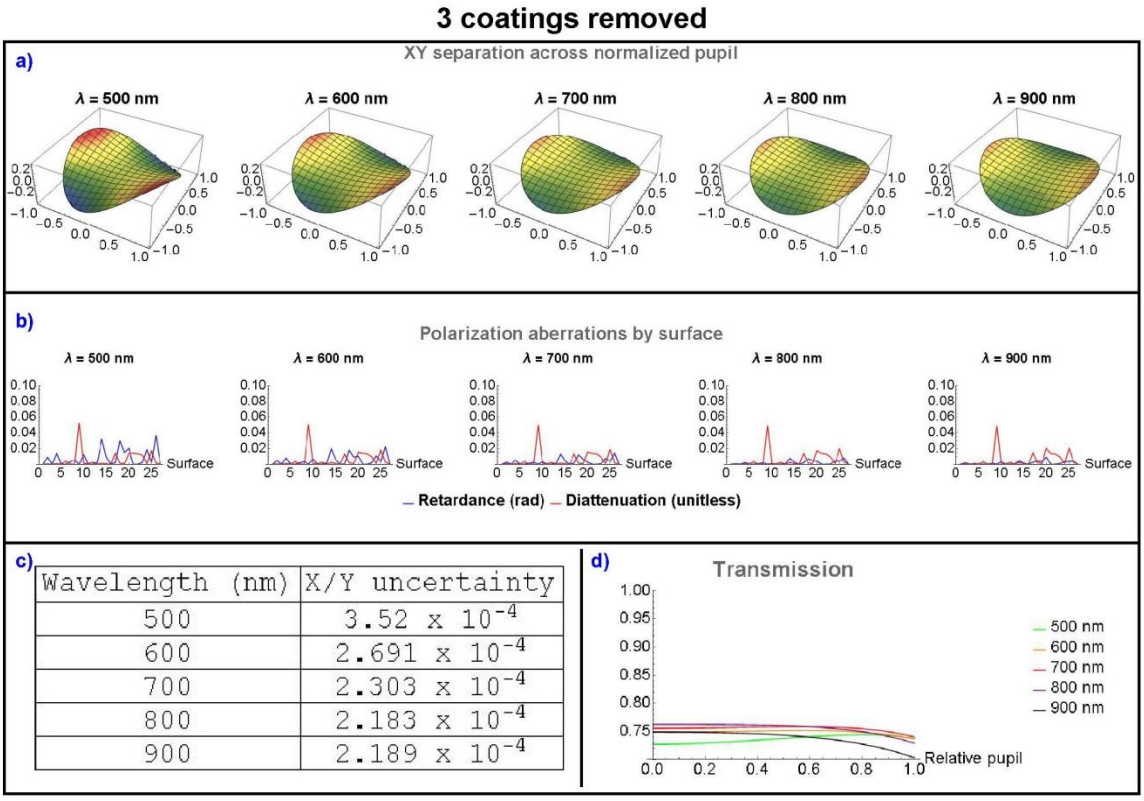

Wavelength (nm)	X/Y uncertainty
500	3.52×10^{-4}
600	2.691×10^{-4}
700	2.303×10^{-4}
800	2.183×10^{-4}
900	2.189×10^{-4}

Figure 3.15. a. X/Y separation pupil maps b. Surface by surface polarization aberrations for marginal rays c. Maximum X/Y uncertainty d. Objective transmission vs relative pupil coordinate

Figure 3.15 gives the results of repeating the previous ray trace with coatings removed from surfaces 9, 21, and 22. The X/Y uncertainty did decrease as intended, but only by about 30% even though more than 50% of the retardance was removed. The pupil maps and surface by surface polarization aberration plots reveal why. The pupil maps for 500 nm, 600 nm, and 700 nm have all rotated towards having a minima/maxima orientation along the x/y axes meaning diattenuation is starting to dominate. In the polarization aberration maps the large retardance values for surfaces 9, 21, and 22 have been replaced by large diattenuation values. The transmission was unacceptably reduced from about 86% to 75%.

This exercise has shown that reducing the objectives retardance will reduce the X/Y separation while highlighting the importance of the AR coatings. If the AR properties are not maintained, on top of reduced transmission there will be increased diattenuation which negates a portion of the X/Y separation improvement from decreased retardance.

3.6 Coating Optimization

The objectives coatings need to be modified to reduce retardance, at least for the surfaces with large retardance, without significant increase in reflection or diattenuation. For this optimization a merit function consisting of a weighted sum of absolute retardance in radians at the edge of the surface, absolute diattenuation at the edge of the surface, reflectance at the center of the surface, and reflectance at the edge of the surface. The merit function weights are shown in Table 3.1. During optimization the merit function is evaluated at more than 5 wavelengths through the spectrum, the weights are determined by interpolating the values entered in Table 3.1 over wavelength.

Optimization weights				
λ (nm)	Diat	Ret (rad)	R_{edge}	R_{Center}
500	1	5	1	3
600	1	3	1	1.5
700	1	2	1	1
800	1	1	1.5	1
900	1	1	4	1

Table 3.1. Merit function weights used in initial optimization

Thin film design approaches usually fit into two categories, methods to refine an existing coating design or methods to synthesize a new coating design [67]. When using

methods to refine an existing design the output will be highly dependent on the starting point. A starting point far from the design requirements is unlikely to converge using just refinement methods. Synthesis methods expand the design space and allows for more possible solutions to the optimization. Many synthesis methods have been proposed and implemented including genetic algorithms, needle algorithms, and combinations of various local and global search approaches [68, 69, 70, 71].

The thin-films starting points this chapter already have the desired reflectance properties so it would be advantageous if the polarization properties could be refined to acceptable values without reducing the transmission too much. The merit function is optimized using a damped least-squares algorithm, one of the most common refinement methods [72, 73]. For each coating the layer thicknesses are the optimized variables. The only constraint used in the initial optimization disallows negative values for layer thickness. Figure 3.16 shows the results of optimization using the merit function from Table 3.1 for surface 9, which originally has the largest retardance. The retardance has been substantially reduced while the other three properties have noticeably increased. The retardance in radians and the diattenuation now have similar magnitudes meaning they will contribute about the same magnitude to X/Y separation. The sum of diattenuation and retardance has become much more uniform across the spectrum instead of much larger for shorter wavelengths. Overall, the optimized coating looks like it will improve the X/Y separation. All of the coatings are optimized by repeating the procedure used for surface 9.

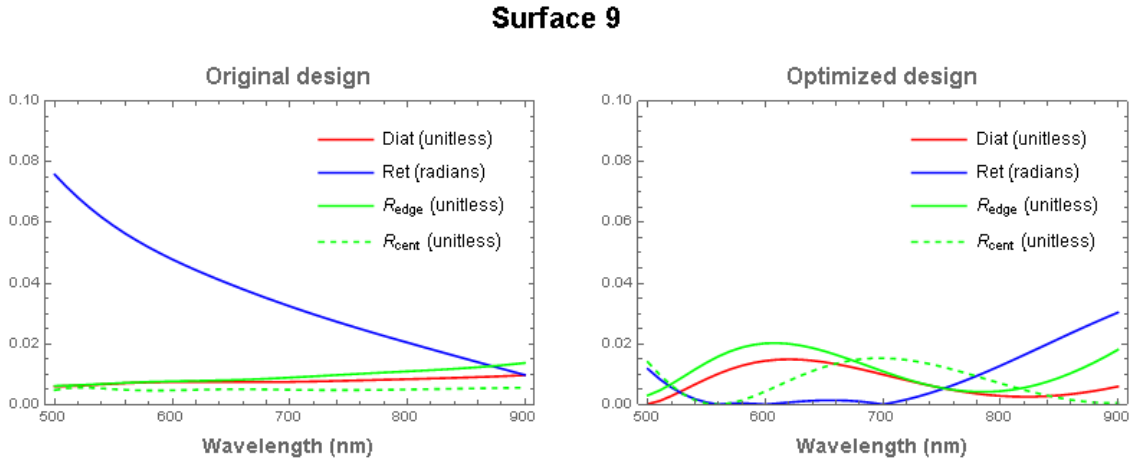

Figure 3.16. The 4 properties making up the merit function plot for surface 9 before and after optimization

Figure 3.17 shows the results of optimizing all of the coatings. The maximum X/Y separation uncertainty has been reduced by a factor of 2. The system now has very similar levels of retardance and diattenuation. The X/Y separation has been shifted in wavelength so that instead of having the best performance at one extreme of the spectrum, the system performs best at the center of the spectrum. The improvement to X/Y separation did not cost any transmission, in fact the overall transmission increased.

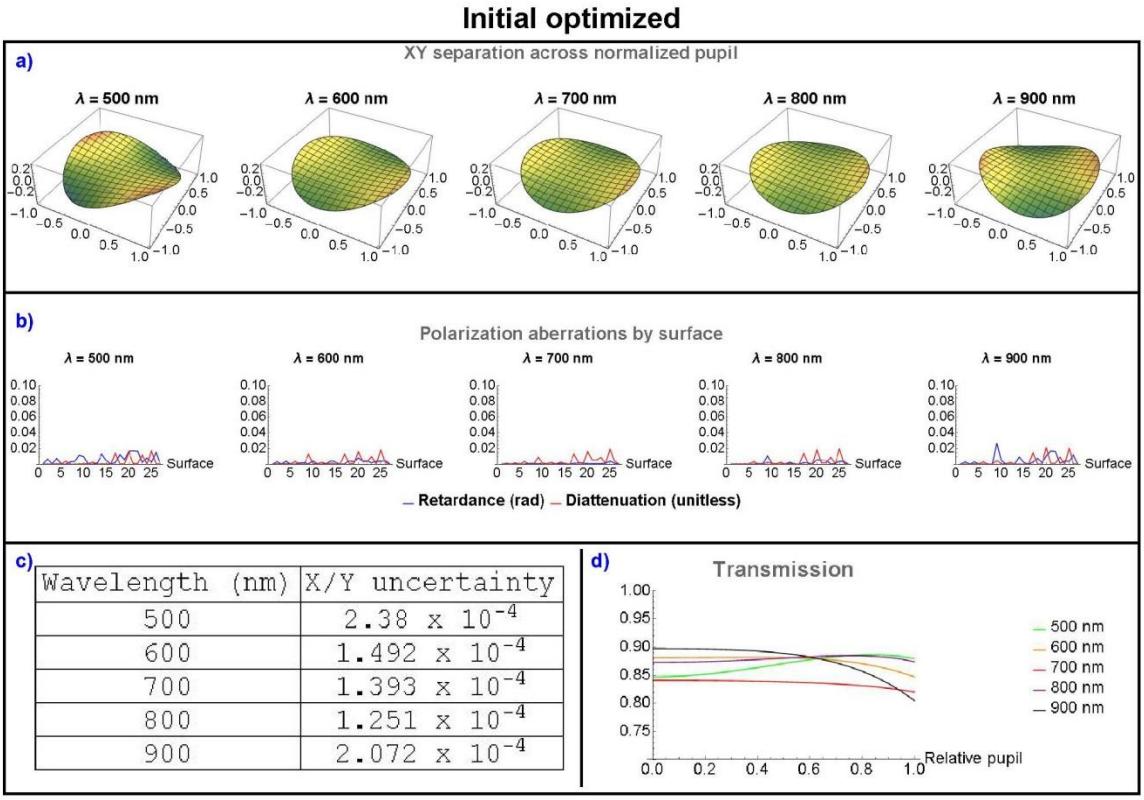

Wavelength (nm)	X/Y uncertainty
500	2.38×10^{-4}
600	1.492×10^{-4}
700	1.393×10^{-4}
800	1.251×10^{-4}
900	2.072×10^{-4}

Figure 3.17. a. X/Y separation pupil maps b. Surface by surface polarization aberrations c. Maximum X/Y uncertainty d. Objective transmission vs relative pupil coordinate

3.7 Manufacturability

After discussions regarding this design, new requirements regarding coating layer thicknesses were developed. No layers thinner than 10 nm are permitted. Try to avoid multiple layers with 10 nm < t < 20 nm in a single coating prescription. Limit the total number of layers thinner than 20 nm. Review of the optimized coating set reveals that a number of layers thicknesses have been driven to 0 nm, these are simply removed, and there are a number of problem layers remaining.

Most of the thinnest layers consist of a thin high-index layer sandwiched between low index layers. These layers are eliminated by replacing the thin high index layer by an equivalent optical thickness of low index material. This reduces the 3-layer structure to a single layer of the same optical thickness. In addition to eliminating the thinnest layers the merit function has been modified to punish layers approaching dangerous thicknesses.

The reoptimized coating set contains no layers less than 10 nm but it still has a number of pretty thin layers. Figure 3.18 shows a pair of histograms comparing the layer thickness distribution for the original coating set and the optimized set. The manufacturability risk of the original set so the comparison had been determined to be acceptable so this comparison contrast the original coatings with the final coatings. The optimized coating set has just 1 additional layer between 10 nm and 15 nm and 4 additional layers between 15 nm and 20 nm. The overall number of layers is reduced in the optimized design. While it is not preferable to add thin layers to the design, none of the thin layers fall into the unacceptable thickness range.

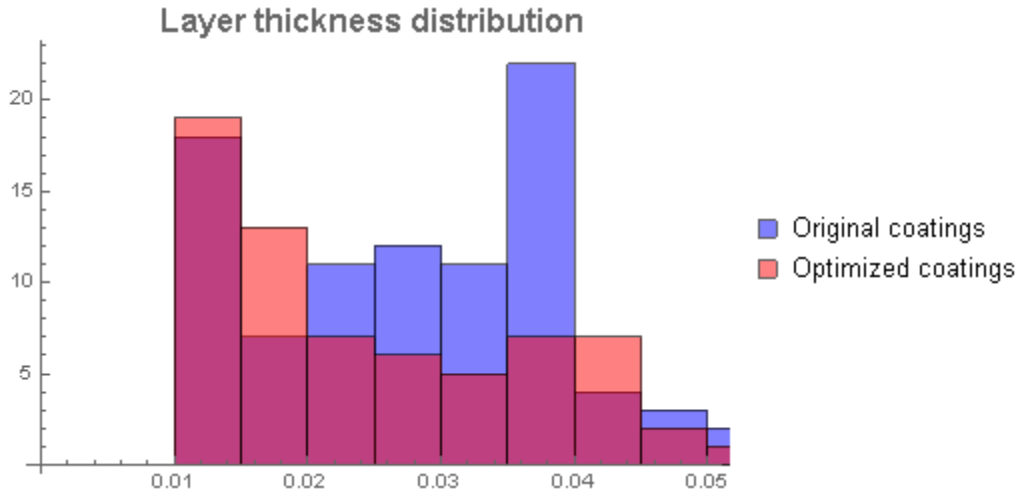

Figure 3.18. Shows the number of potential difficult layers in the original design vs the optimized design

Figure 3.19 shows the final performance of the objective after the thin layers have been removed and the coatings reoptimized. The process was accomplished with minimal impact on X/Y uncertainty or transmission. The updated system still improves X/Y separation by a factor of 2.

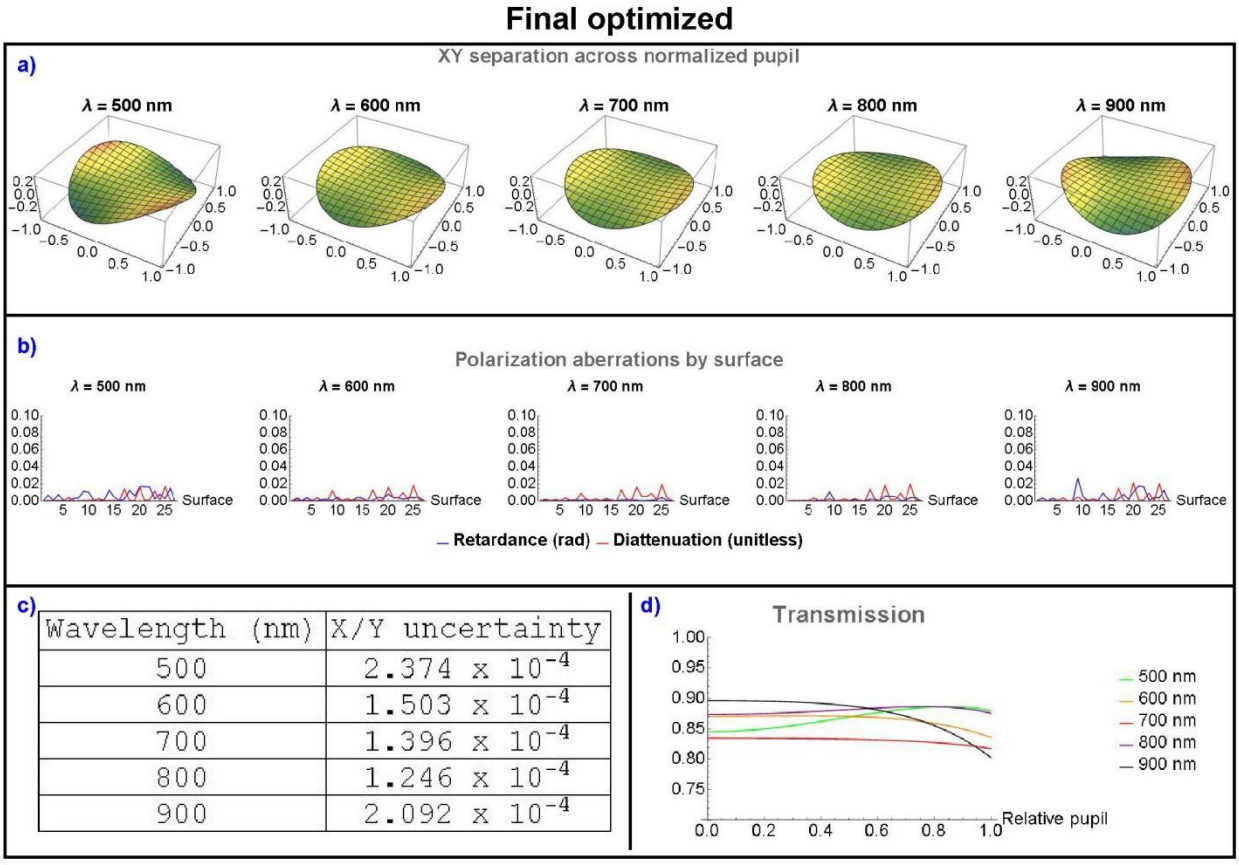

Wavelength (nm)	X/Y uncertainty
500	2.374×10^{-4}
600	1.503×10^{-4}
700	1.396×10^{-4}
800	1.246×10^{-4}
900	2.092×10^{-4}

Figure 3.19. The final performance after removal of problematic layers.

3.8 Monte-Carlo Simulation

A Monte-Carlo simulation is used to provide a more objective look at manufacturability. The simulation is created with layer thickness and layer index as normally distributed random variables with σ_t = 3% and σ_n = 2%. The four parameters associated with out optimization merit function were determined for each of 10,000 randomly generated occurrences for each the original and optimized coating set. The design values with error bars associated with a 95% confidence interval are plotted for the 4 metrics for both coating sets. The results show that the optimized coating set will have similar sensitivities to random thickness and index variations to the original coating set.

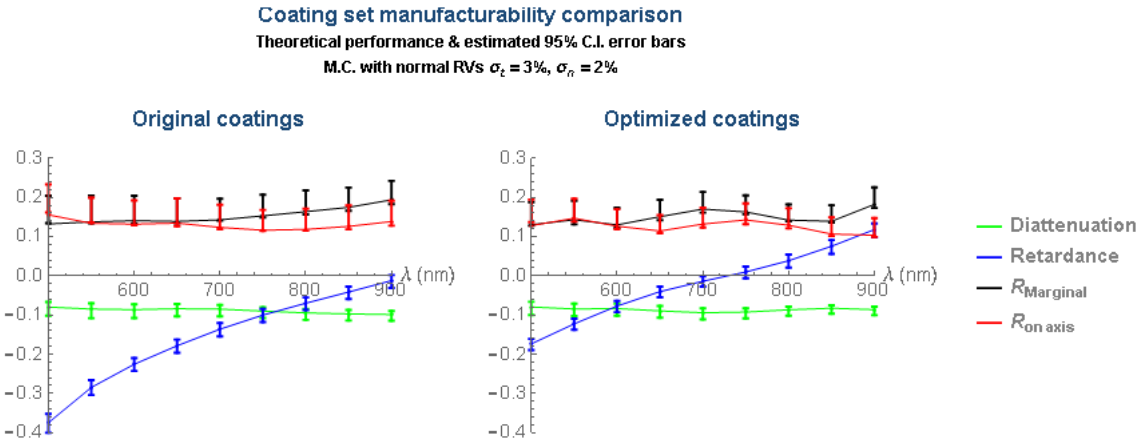

Figure 3.20. Monte-Carlo simulation for original and optimized coatings. The error bars represent the 95% confidence interval based on 10,000 randomly generated coating sets. All layer thicknesses and refractive indices were treated as normally distributed random variables with a standard deviation of 3% and 2% respectively. The reflectance values in the plot represent the total light lost to reflection through the system and are calculated as 1-$T_{Marginal/on\ axis}$.

3.9 Conclusion

The cause of the x/y separation error was identified as retardance caused by AR coatings, primarily coming from three surfaces. It was shown that simply removing the

coating from the worst surfaces could bring the instrument into polarization specifications. A realistic solution was proposed by refining all of the AR coating designs based on a new merit function that included polarization parameters. The proposed modifications had fewer total layers than the original coating set but more very thin layers. A Monte Carlo performed using tolerances provided by thin-film coating engineers found that the proposed coating set was not more sensitive to layer thickness errors than the original coating designs.

While this analysis confirms that no significant additional sensitivities to thickness or index variation have been designed into the coatings it does not properly address the additional thin layers. The lower thickness limit of 10 nm comes from the process of the coating changing from discrete islands of materials to a single continuous coating which happens around 10 nm [74].

REFERENCES

[1] I. J. Hodgkinson, "Optical anisotropy in thin films deposited obliquely: in situ observations and computer modeling," *Applied Optics*, vol. 30, p. 1303, 4 1991.

[2] S. Liedtke, C. Grüner, A. Lotnyk and B. Rauschenbach, "Glancing angle deposition of sculptured thin metal films at room temperature," *Nanotechnology*, vol. 28, p. 385604, 9 2017.

[3] A. Barranco, A. Borras, A. R. Gonzalez-Elipe and A. Palmero, "Perspectives on oblique angle deposition of thin films: From fundamentals to devices," vol. 76, pp. 59-153, 2016.

[4] D. O. Smith, M. S. Cohen and G. P. Weiss, "Oblique-Incidence Anisotropy in Evaporated Permalloy Films," *Journal of Applied Physics*, vol. 31, pp. 1755-1762, 10 1960.

[5] N. Nakhodkin, "Effect of vapour incidence angles on profile and properties of condensed films," *Thin Solid Films*, vol. 10, pp. 109-122, 4 1972.

[6] A. Dirks, "Columnar microstructure in vapor-deposited thin films," *Thin Solid Films*, vol. 47, pp. 219-233, 12 1977.

[7] L. Abelmann and C. Lodder, "Oblique evaporation and surface diffusion," *Thin Solid Films*, vol. 305, pp. 1-21, 8 1997.

[8] K. Robbie and M. J. Brett, "Sculptured thin films and glancing angle deposition: Growth mechanics and applications," vol. 15, pp. 1460-1465, 1997.

[9] R. Messier, V. C. Venugopal and P. D. Sunal, "Origin and evolution of sculptured thin films," *Journal of Vacuum Science Technology A: Vacuum Surfaces and Films*, vol. 18, pp. 1538-1545, 7 2000.

[10] A. Lakhtakia, R. Messier and D. K. Paul, "Sculptured Thin Films: Nanoengineered Morphology and Optics," *Physics Today*, vol. 59, p. 70, 2006.

[11] Y. He and Y. Zhao, "Advanced multi-component nanostructures designed by dynamic shadowing growth," vol. 3, p. 2361, 2011.

[12] J. B. Breckinridge, "Image formation in high-contrast optical systems: the role of polarization," in *Optical, Infrared, and Millimeter Space Telescopes*, 2004.

[13] J. B. Breckinridge and B. R. Oppenheimer, "Polarization Effects in Reflecting Coronagraphs for White-Light Applications in Astronomy," *The Astrophysical Journal,* vol. 600, pp. 1091-1098, 1 2004.

[14] J. R. Gee, I. J. Hodgkinson and P. W. Wilson, "Reflection anisotropy in evaporated aluminum: Consequences for telescope mirror coatings," *Journal of Vacuum Science & Technology A: Vacuum, Surfaces, and Films,* vol. 4, pp. 1875-1878, 7 1986.

[15] N. Woolf and J. R. Angel, "Astronomical Searches for Earth-Like Planets and Signs of Life," *Annual Review of Astronomy and Astrophysics,* vol. 36, pp. 507-538, 9 1998.

[16] J. E. Krist, J. T. Trauger, S. C. Unwin and W. A. Traub, *End-to-end coronagraphic modeling including a low-order wavefront sensor,* vol. 8442, M. C. Clampin, G. G. Fazio, H. A. MacEwen and J. M. Oschmann, Eds., SPIE, 2012, pp. 8442 - 8442 - 11.

[17] H. P. Stahl, *Overview and performance prediction of the baseline 4-meter telescope concept design for the habitable-zone exoplanet observatory,* vol. 10698, H. A. MacEwen, M. Lystrup, G. G. Fazio, N. Batalha, E. C. Tong and N. Siegler, Eds., SPIE, 2018, pp. 10698 - 10698 - 10.

[18] H. P. Stahl, M. Postman, G. Mosier, W. S. Smith, C. Blaurock, K. Ha and C. C. Stark, "AMTD: update of engineering specifications derived from science requirements for future UVOIR space telescopes," in *Space Telescopes and Instrumentation 2014: Optical, Infrared, and Millimeter Wave*, 2014.

[19] J. Davis, J. B. Breckinridge, R. A. Chipman and M. K. Kupinski, "HabEx polarization ray trace and aberration analysis," in *Space Telescopes and Instrumentation 2018: Optical, Infrared, and Millimeter Wave*, 2018.

[20] L. B. Wolff and D. J. Kurlander, "Ray tracing with polarization parameters," *IEEE Computer Graphics and Applications,* vol. 10, pp. 44-55, 11 1990.

[21] Y. Tu, X. Wang, S. Li and Y. Cao, "Analytical approach to the impact of polarization aberration on lithographic imaging," *Optics Letters,* vol. 37, p. 2061, 5 2012.

[22] G. Yun, K. Crabtree and R. A. Chipman, "Three-dimensional polarization ray-tracing calculus I: definition and diattenuation," *Applied Optics,* vol. 50, p. 2855, 6 2011.

[23] G. Yun, S. C. McClain and R. A. Chipman, "Three-dimensional polarization ray-

tracing calculus II: retardance," *Applied Optics,* vol. 50, p. 2866, 6 2011.

[24] R. M. A. Azzam, "Direct relation between Fresnel's interface reflection coefficients for the parallel and perpendicular polarizations," *Journal of the Optical Society of America,* vol. 69, p. 1007, 7 1979.

[25] R. M. A. Azzam and N. M. Bashara, Ellipsometry and Polarized Light (North-Holland Personal Library), North Holland, 1988.

[26] E. Garcia-Caurel, A. D. Martino, J.-P. Gaston and L. Yan, "Application of Spectroscopic Ellipsometry and Mueller Ellipsometry to Optical Characterization," *Applied Spectroscopy,* vol. 67, pp. 1-21, 1 2013.

[27] I. Ohlídal and D. Franta, "Ellipsometry of Thin Film Systems," in *Progress in Optics*, Elsevier, 2000, pp. 181-282.

[28] R. M. A. Azzam and A. G. Lopez, "Accurate calibration of the four-detector photopolarimeter with imperfect polarizing optical elements," *Journal of the Optical Society of America A,* vol. 6, p. 1513, 10 1989.

[29] R. M. A. Azzam, E. Masetti, I. M. Elminyawi and F. G. Grosz, "Construction, calibration, and testing of a four-detector photopolarimeter," *Review of Scientific Instruments,* vol. 59, pp. 84-88, 1 1988.

[30] K. Brudzewski, "Static Stokes Ellipsometer: General Analysis and Optimization," *Journal of Modern Optics,* vol. 38, pp. 889-896, 5 1991.

[31] D. H. Goldstein, "Mueller matrix dual-rotating retarder polarimeter," *Applied Optics*, vol. 31, p. 6676, 11 1992.

[32] P. K. Smith, "Characterizing dielectric tensors of anisotropic materials from a single measurement," 2013.

[33] E. Compain, S. Poirier and B. Drevillon, "General and self-consistent method for the calibration of polarization modulators, polarimeters, and Mueller-matrix ellipsometers," *Applied Optics,* vol. 38, p. 3490, 6 1999.

[34] U. C. W. S. T. (. o. A. T. U. L. G. (. I. P. C. U. Y. Russell A. (University of Arizona, Polarized Light and Optical Systems, Taylor & Francis Inc, 2018.

[35] A. Ciattoni and C. Palma, "Optical propagation in uniaxial crystals orthogonal to the optical axis: paraxial theory and beyond," *Journal of the Optical Society of America*

A, vol. 20, p. 2163, 11 2003.

[36] S. C. McClain, L. W. Hillman and R. A. Chipman, "Polarization ray tracing in anisotropic optically active media I Algorithms," *Journal of the Optical Society of America A*, vol. 10, p. 2371, 11 1993.

[37] S. C. McClain, L. W. Hillman and R. A. Chipman, "Polarization ray tracing in anisotropic optically active media II Theory and physics," *Journal of the Optical Society of America A*, vol. 10, p. 2383, 11 1993.

[38] A. Yariv and P. Yeh, Optical Waves in Crystals: Propagation and Control of Laser Radiation, Wiley-Interscience, 1983.

[39] M. Bass, C. Decusatis and J. M. Enoch, "Handbook of Optics, Third Edition Volume I: Geometrical and Physical Optics, Polarized Light, Components and Instruments(set)," MCGRAW HILL BOOK CO, 2009.

[40] W. S. T. Lam, "Anisotropic ray trace," 2015.

[41] A.-B. Mahler, "Multiangle SpectroPolarimetric Imager (MSPI)," 2010.

[42] A.-B. Mahler and R. A. Chipman, "Polarization state generator: a polarimeter calibration standard," *Applied Optics*, vol. 50, p. 1726, 4 2011.

[43] D. J. Diner, R. A. Chipman, N. A. Beaudry, B. Cairns, L. D. Foo, S. A. Macenka, T. J. Cunningham, S. Seshadri and C. U. Keller, "An integrated multiangle, multispectral, and polarimetric imaging concept for aerosol remote sensing from space," in *Enabling Sensor and Platform Technologies for Spaceborne Remote Sensing*, 2005.

[44] D. J. Diner, A. Davis, B. Hancock, G. Gutt, R. A. Chipman and B. Cairns, "Dual-photoelastic-modulator-based polarimetric imaging concept for aerosol remote sensing," *Applied Optics*, vol. 46, p. 8428, 12 2007.

[45] D. J. Diner, A. Davis, B. Hancock, S. Geier, B. Rheingans, V. Jovanovic, M. Bull, D. M. Rider, R. A. Chipman, A.-B. Mahler and S. C. McClain, "First results from a dual photoelastic-modulator-based polarimetric camera," *Applied Optics*, vol. 49, p. 2929, 5 2010.

[46] A.-B. Mahler, D. J. Diner and R. A. Chipman, "Analysis of static and time-varying polarization errors in the multiangle spectropolarimetric imager," *Applied optics*, vol. 50, pp. 2080-2087, 2011.

[47] G. N. Plass, G. W. Kattawar and S. J. Hitzfelder, "Multiple scattered radiation emerging from Rayleigh and continental haze layers 2: Ellipticity and direction of polarization," *Applied Optics,* vol. 15, p. 1003, 4 1976.

[48] Y. Kawata, "Circular polarization of sunlight reflected by planetary atmospheres," *Icarus,* vol. 33, pp. 217-232, 1 1978.

[49] D. H. Goldstein, Polarized Light, CRC Press, 2010.

[50] B. Boulbry, J. C. Ramella-Roman and T. A. Germer, "Improved method for calibrating a Stokes polarimeter," *Applied Optics,* vol. 46, p. 8533, 12 2007.

[51] D. H. Ballard, "Generalizing the Hough transform to detect arbitrary shapes," *Pattern Recognition,* vol. 13, pp. 111-122, 1 1981.

[52] R. Chan, "New parallel Hough transform for circles," *IEE Proceedings E-Computers and Digital Techniques,* vol. 138, pp. 335-344, 9 1991.

[53] F.-L. Chen and S.-W. Lin, "Subpixel Estimation of Circle Parameters Using Orthogonal Circular Detector," *Computer Vision and Image Understanding,* vol. 78, pp. 206-221, 5 2000.

[54] D. R. Myers and C. A. Gueymard, "Description and availability of the SMARTS spectral model for photovoltaic applications," in *Organic Photovoltaics V*, 2004.

[55] Labsphere, "Integrating Sphere Radiometry and Photometry," 2017.

[56] S. C. McClain, C. L. Bartlett, J. L. Pezzaniti and R. A. Chipman, "Depolarization measurements of an integrating sphere," *Applied Optics,* vol. 34, p. 152, 1 1995.

[57] D. L. Portigal, "Effectiveness of a Quartz Rod as a Light Depolarizer," *Applied Optics,* vol. 8, p. 838, 4 1969.

[58] M. F. Schubert, S. Chhajed, J. K. Kim, E. F. Schubert and J. Cho, "Polarization of light emission by 460nm GaInN⁄GaN light-emitting diodes grown on (0001) oriented sapphire substrates," *Applied Physics Letters,* vol. 91, p. 051117, 7 2007.

[59] G. Harten, D. J. Diner, B. J. S. Daugherty, B. E. Rheingans, M. A. Bull, F. C. Seidel, R. A. Chipman, B. Cairns, A. P. Wasilewski and K. D. Knobelspiesse, "Calibration and validation of Airborne Multiangle SpectroPolarimetric Imager (AirMSPI) polarization measurements," *Applied Optics,* vol. 57, p. 4499, 5 2018.

R. A. Chipman, "Polarization Analysis Of Optical Systems," *Optical Engineering*, vol. 28, p. 290, 2 1989. [60]

D. J. Reiley and R. A. Chipman, "Coating-induced wave-front aberrations: on-axis astigmatism and chromatic aberration in all-reflecting systems," *Applied Optics*, vol. 33, p. 2002, 4 1994. [61]

R. A. Chipman, "POLARIZATION ABERRATIONS (THIN FILMS).," 1987. [62]

M. Totzeck, "Orientation Zernike polynomials: a useful way to describe the polarization effects of optical imaging systems," *Journal of Micro/Nanolithography, MEMS, and MOEMS*, vol. 8, p. 031404, 7 2009. [63]

H. A. MacLeod, Thin-Film Optical Filters, Fifth Edition, Taylor & Francis Ltd, 2018. [64]

A.-B. Mahler, P. K. Smith and R. A. Chipman, "Low polarization optical system design," in *Polarization Science and Remote Sensing III*, 2007. [65]

J. Wolfe and R. A. Chipman, "Reducing symmetric polarization aberrations in a lens by annealing," *Optics Express*, vol. 12, p. 3443, 2004. [66]

L. Li, C. Liu and Q.-H. Wang, "Three-step method for optimization of optical thin film," *Optik*, vol. 124, pp. 1796-1799, 7 2013. [67]

L. Li, Q.-H. Wang, D.-H. Li and H.-R. Peng, "Jump method for optical thin film design," *Optics Express*, vol. 17, p. 16920, 9 2009. [68]

J. A. Dobrowolski, "Completely Automatic Synthesis of Optical Thin Film Systems," *Applied Optics*, vol. 4, p. 937, 8 1965. [69]

J.-M. Yang and C.-Y. Kao, "An evolutionary algorithm for the synthesis of multilayer coatings at oblique light incidence," *Journal of Lightwave Technology*, vol. 19, pp. 559-570, 4 2001. [70]

A. V. Tikhonravov, M. K. Trubetskov and G. W. DeBell, "Optical coating design approaches based on the needle optimization technique.," *Applied optics*, vol. 46, no. 5, pp. 704-710, 2 2007. [71]

A. L. Bloom, "Refining and optimization in multilayers," *Applied Optics*, vol. 20, p. 66, 1 1981. [72]

J. A. Dobrowolski and R. A. Kemp, "Refinement of optical multilayer systems with [73]

different optimization procedures," *Applied Optics,* vol. 29, p. 2876, 7 1990.

[74] M. W. McCall, Q. Wu and I. J. Hodgkinson, Birefringent Thin Films and Polarizing Elements, ICP, 2014.

[75] E. Waluschka, "Polarization Ray Trace," *Optical Engineering,* vol. 28, p. 286, 2 1989.

[76] W. Urbańczyk, "Optical Transfer Function for Imaging Systems Which Change the State of Light Polarization," *Optica Acta: International Journal of Optics,* vol. 33, pp. 53-62, 1 1986.

[77] W. Urbanczyk, "OPTICAL IMAGING SYSTEMS CHANGING THE STATE OF LIGHT POLARIZATION: IMAGE FORMATION FOR COHERENT DIFFUSE OBJECTS.," *Optik (Jena),* vol. 68, pp. 247-254, 10 1984.

[78] J. P. McGuire and R. A. Chipman, "Diffraction image formation in optical systems with polarization aberrations. II - Amplitude response matrices for rotationally symmetric systems," *Journal of the Optical Society of America A,* vol. 8, pp. 833-840, 6 1991.

[79] J. P. McGuire and R. A. Chipman, "Diffraction image formation in optical systems with polarization aberrations. I - Formulation and example," *Journal of the Optical Society of America A,* vol. 7, pp. 1614-1626, 9 1990.

[80] M. Mansuripur, "Effects of high-numerical-aperture focusing on the state of polarization in optical and magneto-optical data storage systems," *Applied Optics,* vol. 30, pp. 3154-3162, 8 1991.

[81] R. Dorn, S. Quabis and G. Leuchs, "Sharper Focus for a Radially Polarized Light Beam," *Physical Review Letters,* vol. 91, p. 233901, 12 2003.

[82] T. J. Bruegge, "Analysis of polarization effects in optical systems," in *Polarization Considerations for Optical Systems II*, 1990.

[83] H. Kikuta, H. Toyota and W. Yu, "Optical Elements with Subwavelength Structured Surfaces," *Optical Review,* vol. 10, pp. 63-73, 3 2003.

[84] H.-T. Huang, W. Kong and F. L. Terry, "Normal-incidence spectroscopic ellipsometry for critical dimension monitoring," *Applied Physics Letters,* vol. 78, pp. 3983-3985, 6 2001.

[85] D. S. Sabatke, A. M. Locke, M. R. Descour, W. C. Sweatt, J. P. Garcia, E. L. Dereniak, S. A. Kemme and G. S. Phipps, "titleFigures of merit for complete Stokes polarimeter optimization/title," in *Polarization Analysis, Measurement, and Remote Sensing III*, 2000.

[86] O. P. Hasekamp and J. Landgraf, "Retrieval of aerosol properties over land surfaces: capabilities of multiple-viewing-angle intensity and polarization measurements," *Applied Optics*, vol. 46, p. 3332, 5 2007.

[87] J. F. Haan, P. B. Bosma and J. W. Hovenier, "The adding method for multiple scattering calculations of polarized light," *Astronomy and Astrophysics*, vol. 183, pp. 371-391, 1987.

[88] D. A. Haner and R. T. Menzies, "Integrating sphere depolarization at 10 m for a non-Lambertian wall surface: application to lidar calibration," *Applied Optics*, vol. 32, p. 6804, 11 1993.

[89] M. K. Trubetskov and A. V. Tikhonravov, "Robust Synthesis of Multilayer Coatings," in *Optical Interference Coatings*, 2010.

[90] A. Premoli and M. L. Rastello, "Minimax refining of wideband antireflection coatings for wide angular incidence," *Applied Optics*, vol. 33, p. 2018, 4 1994.